



UNIVERSITA' DEGLI STUDI DI MILANO

Dipartimento di Scienze Biomediche per la Salute

PhD course in

Integrative Biomedical Research (R23)

XXXIII Cycle

**Investigation on pharmacological and age-induced
modulations of cardiac peacemaking
and electrophysiological characterization
of a compound mutation in the cardiac sodium channel**

Dr. David Molla

Matr. R12111

Tutor: Prof. Mirko Baruscotti

Coordinator: Prof. Chiarella Sforza

Academic Year 2019-2020

INDEX

PREFECE	- 4 -
Identification of the bradycardic molecule contained in the traditional Chinese medicine drug Tongmai Yangxin:	- 4 -
Age-related changes in cardiac autonomic modulation and heart rate variability in mice:.....	- 5 -
Electrophysiological characterization of a SCN5A compound mutation (K1578N-G1866fs) discovered in a young patient affected by sinus node dysfunction, atrial flutters and drug-induced long QT syndrome:.....	- 6 -
GENERAL INTRODUCTION	- 9 -
The heart	- 9 -
Anatomy.....	- 9 -
Functions	- 11 -
Cardiac muscle and electrical activity	- 11 -
Autonomic innervation	- 13 -
Electrocardiogram	- 14 -
Heart rate variability	- 16 -
The action potential	- 16 -
Fast response action potential	- 16 -
Slow response action potential	- 18 -
The pacemaker ‘Funny’ current	- 19 -
HCN channels	- 20 -
Structure and function.....	- 20 -
Pharmacology	- 23 -
Voltage-gated Na ⁺ channel Nav1.5.....	- 25 -
TRADITIONAL CHINESE MEDICINE	- 28 -
INTRODUCTION.....	- 28 -
Traditional Chinese medicine	- 28 -
Tongmai Yangxin	- 30 -
Background.....	- 31 -
AIMS	- 36 -
MATERIALS AND METHODS.....	- 37 -
Animals	- 37 -
Cells isolation	- 37 -
Patch-clamp solutions	- 39 -
Protocols and data analysis	- 40 -
RESULTS	- 43 -

TMYX fractions (F1-4) analysis	- 43 -
F1 sub-fractions (F1.1-1.4) analysis	- 48 -
Preliminary investigations on uridine	- 50 -
DISCUSSION	- 52 -
PACEMAKER MODULATION IN AGING	- 55 -
INTRODUCTION.....	- 55 -
AIMS	- 57 -
MATERIALS AND METHODS.....	- 58 -
Animals	- 58 -
Transmitter implantation	- 58 -
Pharmacological ANS modulation	- 58 -
Data recording and analysis	- 59 -
Incidence of cardiac arrhythmias	- 60 -
RESULTS	- 61 -
Circadian HR and HRV rhythms	- 61 -
Age-related differences in ANS modulation of the heart rate.....	- 62 -
HRV responses to pharmacological autonomic blockades.....	- 64 -
Vulnerability to cardiac arrhythmias	- 67 -
DISCUSSION.....	- 69 -
Age-related changes in cardiac ANS modulation in mice	- 69 -
Utility of HRV indexes in detecting age-related changes in murine cardiac ANS modulation ..	- 70 -
Age-related changes in the vulnerability to cardiac arrhythmias	- 71 -
SODIUM CHANNEL MUTATIONS	- 73 -
INTRODUCTION.....	- 73 -
AIMS	- 76 -
MATERIALS AND METHODS.....	- 77 -
Cell culture	- 77 -
Plasmids generation and transfection	- 77 -
Patch clamp solutions	- 79 -
Protocols and data analysis	- 79 -
RESULTS	- 81 -
DISCUSSION.....	- 86 -
REFERENCES	- 88 -

PREFECE

During my Ph.D. internship at the 'PaceLab', I have been involved in several scientific projects that, although involving different experimental models and with different aims, share the common background of cardiac pacemaker modulation and ion channels activity. In this section are briefly described the three main research lines in which I took part; a more complete discussion of the data will be presented later in this thesis. Notably, by the time I am writing this proposition, two of these studies have been submitted to scientific journals.

- **Identification of the bradycardic molecule contained in the traditional Chinese medicine drug Tongmai Yangxin:**

The identification of new bradycardic agents able to specifically bind HCN channels, rises great interest in the scientific community since a decreased cardiac pacemaker current would lead to an general heart rate lowering without side-effects. To date, despite a long and intensive investigation, only one pure bradycardic agent (Ivabradine)¹⁻³ is used in the clinical setting. Ivabradine is considered virtually free of negative side-effects even though, in some rare cases, it can elicit minor optical limitations.

A few years ago, our research group started a collaboration with a traditional Chinese medicine (TCM) drug producer (Le Ren Tang Pharmaceutical Factory, Tianjin, China) with the aim of unravelling the molecular mechanism of one of their products: Tongmai Yangxin (TMYX). This drug is currently used in China for the treatment of several cardiac diseases like coronary artery disease, palpitation, heart failure and angina⁴ and, like other TCM compounds, it is a mixture of botanical and animal products. Remarkably, recent investigations highlighted its ability to reduce cardiac metabolic disorders, oxidative stress and inflammation on stable angina patients⁴⁻⁶.

Our previous studies explored the bradycardic action of this drug; in particular, its effects were evaluated on freshly isolated rabbit SAN myocytes. TMYX displayed a dose dependent and fully reversible rate slowing of the spontaneous action potential (AP) activity, specifically acting on the pacemaker current by shifting the activation curve of HCN channels towards more negative potentials; furthermore, its efficacy appeared to be strictly correlated to the intracellular cAMP concentration. Detailed analysis demonstrate that this drug acts as a functional cAMP surmountable competitive antagonist,

competing for the CNBD of f-channels according to a mode of action never observed before for the regulation of this current. Still, the nature of the bio-active molecule is unknown.

With the aim of identify this principle, TMYX was divided into 4 fractions (F1-4) by our Chinese colleagues at the Pharmaceutical Informatics Institute of Zhejiang University (Hangzhou, China) according to the solubility of its components, and the ability of each preparation to modulate spontaneous rate and the I_f current was evaluated by patch-clamp experiments in rabbit SAN myocytes. Data clearly demonstrate that only the most hydrophilic fraction (F1) displayed features similar to the total drug, decreasing the AP rate up to ~20% specifically acting on the pacemaker current.

To further narrow down the number of molecules to examine, F1 was subsequently divided into 4 sub-fractions (F1.1-1.4) and, as for the previous preparations, their effects were examined on rabbit SAN myocytes. The results pointed out the presence of the target molecule both in F1.1 and F1.2 since they were able to reduce the spontaneous AP firing by ~25 and ~20%, respectively, with a specific action on I_f current.

Eventually, HPLC data revealed the presence of uridine in both these sub-fraction, suggesting that this molecule (or one of its derivates) could be involved in the bradycardic process. Therefore, a preliminary experiment was carried out to analyze its possible cardiac rate regulation properties on rabbit SAN myocytes. Surprisingly, the perfusion of uridine (1 μ M) generated a small increase in the AP rate (+3.45%) but a decrease in the pacemaker current at -65mV. Additional experiment are requested in order to shed more light on the properties of this molecule, however, given that uridine, and in particular its cyclic nuclidic form (cUMP), have been reported to interact with some isoforms of the HCN channels family⁷⁻⁹, it appears to be a good starting point for the identification of the active principle of TMYX.

- **Age-related changes in cardiac autonomic modulation and heart rate variability in mice:**

The incidence of mortality caused by age-associated cardiovascular diseases is increasing dramatically and it will represent a serious clinical issue in the next decades^{10,11}.

In humans, the natural process of aging is associated with progressive changes in cardiac autonomic nervous system (ANS) regulation that may predispose to higher cardiac risks.

Animal models of aging are needed to gain insights into the relation between the aging of the ANS and cardiac pathophysiology. Specifically, the aim of this study is to verify the translational relevance of mouse models for further in-depth evaluation of the link between cardiac ANS regulation and increased arrhythmic risk with advancing age.

Therefore, heart rate and time- and frequency-domain indexes of HRV were calculated from ECG recordings in two groups of conscious C57BL6/J male mice of different ages (4- and 19-months-old) during daily undisturbed conditions following peripheral β -adrenergic (atenolol), muscarinic (methylscopolamine), and β -adrenergic + muscarinic blockades and β -adrenergic (isoprenaline) stimulation. Eventually, vulnerability to arrhythmias was evaluated during daily, undisturbed conditions and following β -adrenergic stimulation.

HRV analysis and heart rate responses to autonomic blockades revealed that 19-month-old mice had a lower vagal modulation of cardiac function compared with 4-month-old mice. This age-related autonomic effect did not however affect basal heart rate, since it compensated for the lower intrinsic heart rate observed in 19-month-old compared with 4-month-old mice. Both time- and frequency-domain indexes of HRV were reduced following muscarinic, but not β -adrenergic, blockade, suggesting that HRV is largely modulated by vagal tone in mice. Finally, 19-month-old mice showed a larger vulnerability to both spontaneous and isoprenaline-induced arrhythmias.

These results reveal the presence of a reduced cardiac vagal modulation and HRV associated with an increased vulnerability to cardiac arrhythmias in older mice, which is consistent with the human condition. Given their short life span, mice could be further exploited as an aged model for studying the trajectory of vagal decline with advancing age using HRV measures, and the mechanisms underlying its association with proarrhythmic remodeling of the senescent heart.

- **Electrophysiological characterization of a SCN5A compound mutation (K1578N-G1866fs) discovered in a young patient affected by sinus node dysfunction, atrial flutters and drug-induced long QT syndrome:**

Given its high relevance in the generation of the cardiac AP event, alterations in the genetic sequence encoding for Na_v1.5 channel (SCN5A) are often related to severe dysfunction in the heart function¹².

In this situation, a compound mutation (K1578N/G1866fs) has been reported in a child affected by severe bradycardia, atrial flutter and drug-induced QT prolongation. Notably, the parents, who present a heterozygous mutation each, did not suffer of any cardiac problem and their ECG signals were unremarkable. Following clinical examinations, the diagnosis was sinus node dysfunction and the patient was implanted with a pacemaker¹³. With this study we intended to characterize the electrical properties of the Na^+ current carried by the mutated $Na_V1.5$ channels in order to better understand the impact of these alteration and explore whether the patient will benefit from a specific pharmacological treatment.

According to the literature^{14,15}, *SCN5A* gene can undergo a series of alternative splicing events, among which the inclusion of different exon 6 sequences that identify the neonatal and the adult $Na_V1.5$ isoform. Consequently, the electrical difference between these two isoforms was assessed by patch-clamp experiments on HEK-293 cells transfected with a vector containing their genetic sequence. The results displayed no differences in the current density compared to the adult isoform (HP: -120 mV) while a positive shift of both activation and inactivation curves were detected (5.1 mV and 8.8 mV, respectively). The impacts of the mutations on the Na^+ current were then evaluated on the same model both in the patient (compound mutation K1578N/G1866fs in the neonatal isoform) and in the parents (heterozygous expression in the adult isoform) conditions. For what concerns the parents, the data collected are reasonably in agreement with the clinical investigation indicating no pathologic conditions. On the other hand, the transfection of both the mutations in the neonatal *SCN5A* isoform caused a dramatic reduction in the current density associated to a rightward shift of the activation curve (6.5 mV), compared to the corresponding WT isoform.

In addition, since the time at which the neonatal to adult isoform switch occurs has still not been clearly identify, the compound mutation was also inserted in the WT adult vector. However, no changes were detected in the current density while a leftward shift of the activation curve (7.5 mV), which can be ascribed to the isoform change, suggested that the alterations have a similar effect on the activation kinetics regarding of the isoform in which are expressed.

Eventually, no changes in the recovery from inactivation process were found between all the conditions investigated.

All in all, these data show an important loss-of-function of Nav1.5 channels in the patient's condition, suggesting that the two mutations (K1578N–G1866fs), when expressed together, generate a far worst phenotype than their single heterozygous expression. Furthermore, even when incorporated in the adult SCN5A isoform, the effects caused by the alterations did not change suggesting that the neonatal to adult isoform switch will probably grant no benefits for the patient.

GENERAL INTRODUCTION

The heart

Anatomy

The heart is a muscular, hollow, unequal organ that lies in the anterior mediastinum, behind the body of sternum and the second to sixth costal cartilages, in front of the thoracic vertebrae T5-T8 and above the diaphragm. A double-membraned connective sac called the pericardium surrounds and attaches it to the mediastinum; it limits the cardiac acute dilation and offers protection against infections. This organ is pyramidal in shape with the basis facing upward to the right and the apex downward to the left; its axis is therefore oblique so that a third of it lies to the right of the median plane and two-thirds of it to the left.

A normal heart has the size of a closed fist and weighs between 188 and 575 grams¹⁶.

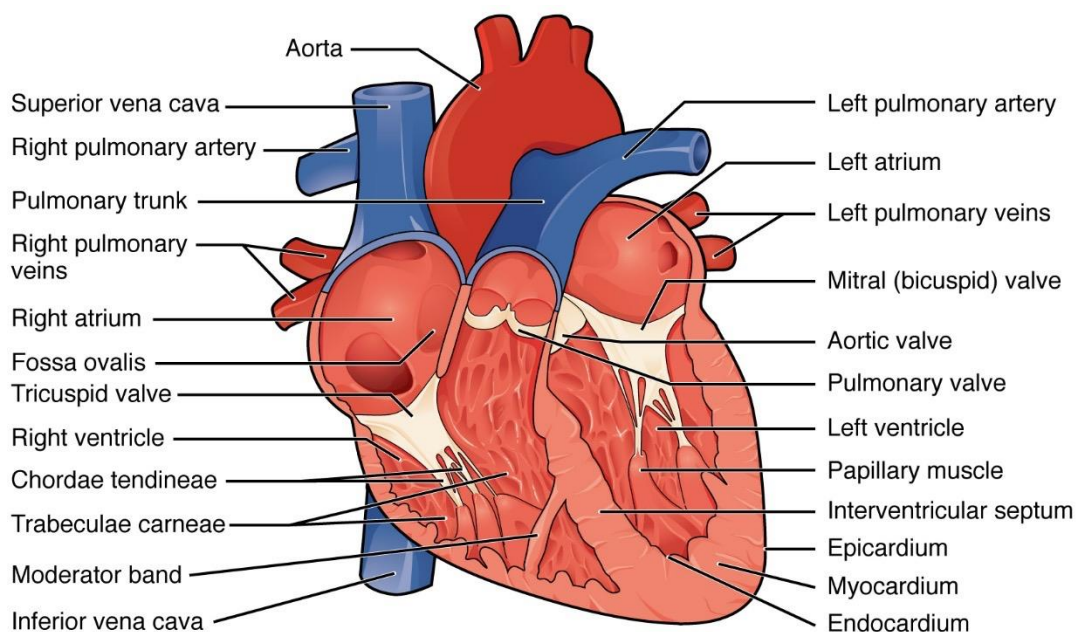


Figure 1. Anatomy of the human heart.

Internal anterior view of the human heart that shows the four chambers, the major vessels and their early branches (in blue the ones in which flows deoxygenated blood while in red the ones in which flows the oxygenated one), as well as the valves and other minor structures.

It consists of four chambers (**figure 1**): the upper two are called atria and are separated by the interatrial septum, while the lower two are called ventricles and are separated by the interventricular septum. Atria and ventricles are isolated from each other by means of the atrioventricular septum. The only way for the blood to flow in the chambers is through the atrioventricular valves, thin flaps of tissue controlled by the papillary muscles via the chordae tendineae. The tricuspid valve allows a monodirectional blood flow from the right atrium to the right ventricle while the bicuspid (or mitral) valve allows the same type of blood flow from the left atrium to the left ventricle.

Although the heart wall is mostly composed by cardiac muscle fibers, it can be divided into three layers: endocardium, myocardium and epicardium (**figure 2**).

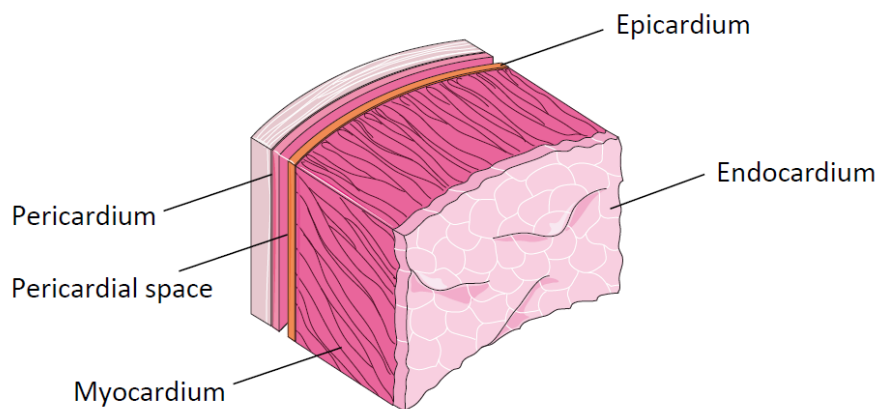


Figure 2. Structure of the heart wall.

Schematic representation of the composition of the heart wall which shows the three cardiac layers (endocardium, myocardium and epicardium) as well as the pericardium.

The endocardium is the innermost layer that lines the atria, the ventricles and covers the cardiac valves distributing nutrients to the myocytes through a dense network of capillary vessels; it is made up of loose connective tissue and endothelium.

The myocardium is the intermediate level and the main functional constituent of the wall. It is a striated cardiac muscle layer whose thickness varies between atria and ventricles providing a greater contraction ability to the latter ones.

The epicardium is the outmost level and represents the visceral layer of the pericardium. It is composed by mesothelial cells below which lies a small amount of adipose and fibroelastic connective tissue that cushions the organ.

Functions

Blood is the fundamental vehicle by which oxygen and nutrients are distributed through the organism, thus the main function of the heart is to provide a continuous blood flow to the whole body.

Generally, the heart right side contains deoxygenated blood whereas its left side contain the oxygenated one; the mixing of fluids is prevented by the interatrial and the interventricular septi. Furthermore, the atrioventricular valves, located between atria and ventricles, and the semilunar valves, placed at the entrance of arteries, prevent any form of retrograde flow.

In the right atrium, deoxygenated blood coming from the whole body is collected from two large veins: the superior and the inferior venae cavae. The blood is then conveyed to the right ventricle through the tricuspid valve and finally to the pulmonary trunk which branches and generates the pulmonary circulation. In this circuit blood exchanges carbon dioxide for oxygen in the lungs, thanks to the process of respiration. Subsequently, the newly oxygenated blood reaches the left atrium via the pulmonary veins, enters the left ventricle through the mitral valve and is finally distributed to all tissues via the aorta and the systemic circulation.

Cardiac muscle and electrical activity

According to their function, myocardial cells can be divided in two categories: working and conduction myocytes.

Working cardiomyocytes represent the majority of the myocardium; their task is to contract to ensure an efficient blood distribution to the entire organism. Striated muscle fibers are connected to each other with peculiar structures called intercalated discs, fundamental for the transmission of the electrical signal between cells.

The conduction system of the heart is made up of specialized myocytes capable of generating and conducting an electric signal throughout the organ. Once generated, the impulse follows a specific path which allows the heart to contract in a coordinated way. The electrical event, also called depolarization wave, is indeed the trigger for the muscular contraction of working cells. The cardiac conduction system includes several specific regions, such as the sinoatrial node (SAN), the atrioventricular node (AVN), the bundle of His, the two bundle branches and the Purkinje fibers network (**figure 3**).

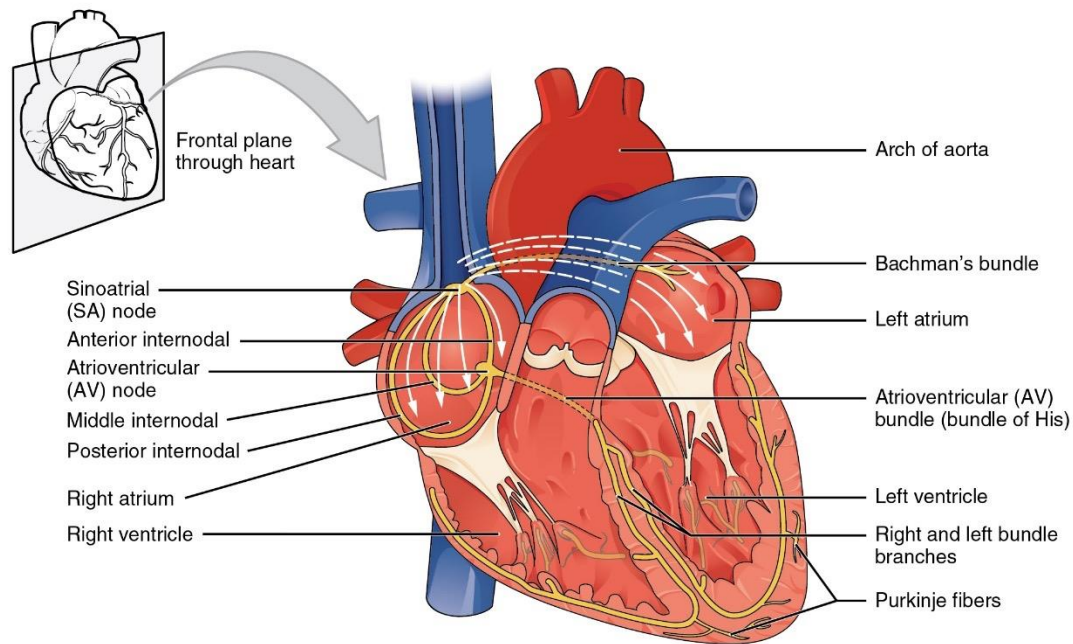


Figure 3. Anatomy of the conduction system of the human heart.

Internal anterior view of the human heart that illustrates the location of the main elements of the cardiac conduction system.

Cardiac rhythm is established in the SAN, a highly specialized cluster of myocytes located in the area where the superior vena cava joins the right atrium. The impulse then spreads through the atria via the internodal pathways and reaches the AVN. It takes approximately 50 ms to travel between these two locations and an additional pause of 100 ms occurs at the AVN. This delay allows an efficient atrial filling so that the correct amount of blood can be pumped into the ventricles. Subsequently, the pulse proceeds through the interventricular septum via the bundle of His before it divides into the two bundle branches. This passage takes approximately 25 ms. The branches then reach the apex and then, the base of the ventricles. Finally, the Purkinje fibers emerge from the last tract of the branches and spread into a dense network, delivering the pulse in the myocardial layer. Purkinje cells have a fast inherent conduction rate and the electrical pulse reaches all of the ventricular muscle in about 75 ms. The total time required from the generation of the impulse until the depolarization of the last parts of the ventricles is approximately 225 ms¹⁷.

Although the primary, or natural, pacemaker of the heart is the SAN, other cardiac regions possess pacemaker potentiality (**figure 4**), a feature that is fundamental under non-physiological conditions, such as hypoxia or SAN block; when the natural pacemaker is not able to fulfill its function, it can be substituted by another beating region. The ability of the SAN to dominate

over other autorhythmic areas is a phenomenon called '*overdrive suppression*'; this mechanism ensures that the region with higher intrinsic rate dominates over the lower ones.

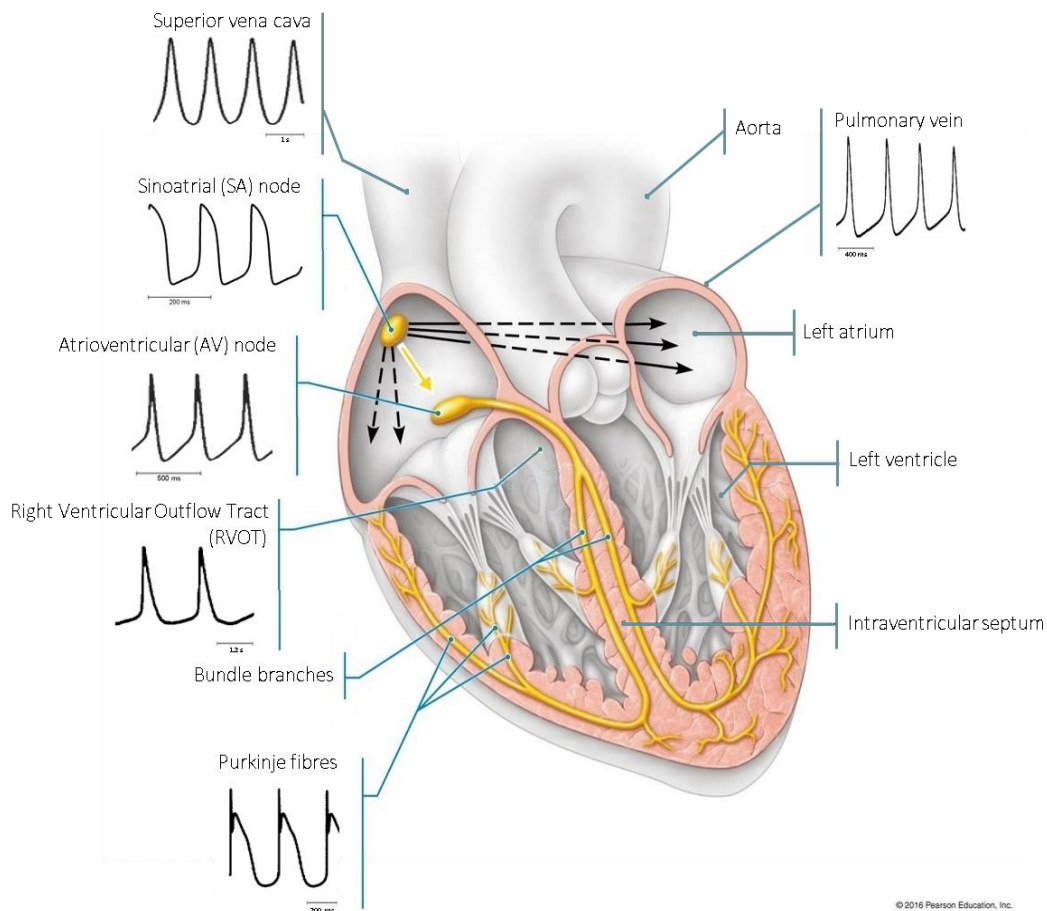


Figure 4. Pacemaker potential of different areas of the heart.

Representation of the cardiac conduction system and typical action potential traces recorded from the superior vena cava (dog, 37°C¹⁸), the SAN (rabbit, 35°C; D. Molla, unpublished data), the AVN (rabbit, 35–37°C¹⁹), the RVOT (rabbit, 37°C; S.J.R.J. Logantha, unpublished data), Purkinje fibers (rabbit, free running; 37 °C; S.J.R.J. Logantha, unpublished data) and pulmonary veins (rabbit, 37°C²⁰). All records were acquired in tissue preparations with the exception of SAN, AVN and superior vena cava recordings, which were obtained from isolated myocytes (modified from Dobrazynski et al., 2013).

Autonomic innervation

The intrinsic autorhythmicity of SAN cells keeps the heart beating at a regular pace; however, cardiac function is modulated by and responds to outside influences as well. Specifically, this organ is abundantly innervated by the autonomic nervous system (ANS), both by the sympathetic and the parasympathetic branches (**figure 5**).

Sympathetic fibers originate from the spinal cord (T1–T4 region), contact the paravertebral ganglia and travel to the SAN, atria and ventricles. The effects of a sympathetic activation are essentially an increase in chronotropy (beating rate), inotropy (power of muscular contraction) and dromotropy (speed of conduction of the electrical impulse)²¹. Parasympathetic fibers, on the other hand, originate from the brainstem and travel directly to the SAN and AVN via the vagal nerve (X cranial nerve)²². The effects of a parasympathetic activation are substantially opposite to those of the sympathetic system: a decrease in chronotropy and dromotropy²¹.

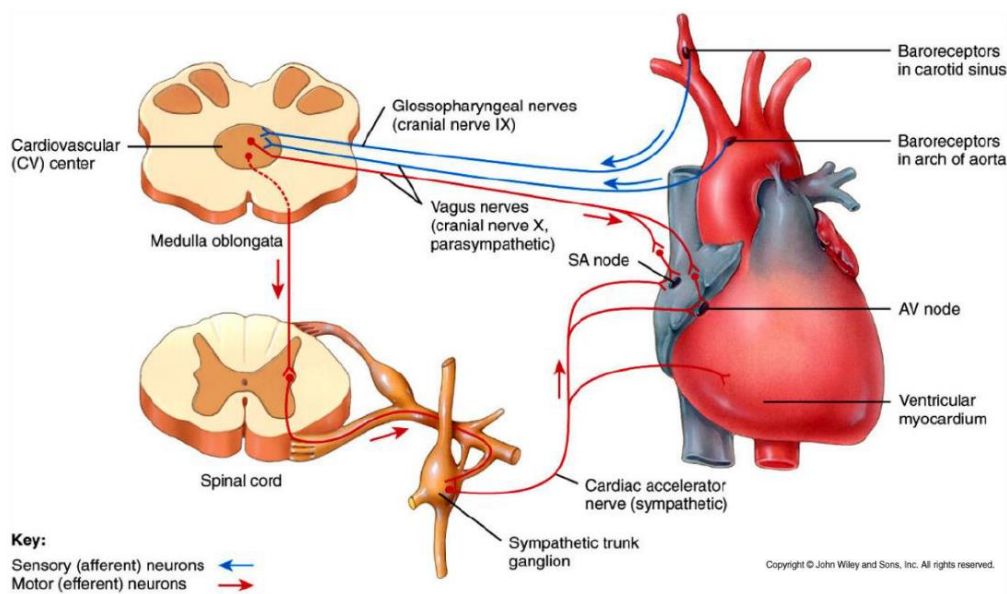


Figure 5. *Illustration of the cardiac ANS innervation.*

Both the branches of the ANS innervate the heart regulating chronotropy, inotropy and dromotropy. At the same time, information about blood pressure are sensed from the baroreceptors and delivered to the brainstem through the IX cranial nerve.

Electrocardiogram

Electrocardiography is the process of recording the electrical activity of the heart over a period of time using a series of electrodes placed on the skin of a patient. The graph of voltage versus time produced by this noninvasive medical procedure is referred to as an electrocardiogram (ECG) and offers a graphical representation of the voltage fluctuations that occur at every beating cycle (**figure 6, bottom**). Normal EGC traces have a characteristic shape defined by positive and negative waves which are altered under pathological conditions²³ (**figure 6, top**).

P wave represents the atrial depolarization from the SAN to the AVN and from the right to the left atrium. It lasts between 60 and 120 ms.

QRS complex is a set of three consecutive waves and reflects the ventricular depolarization:

- Q wave represents the depolarization of the intraventricular septum;
- R wave represents the depolarization of the apex of the ventricles;
- S wave represents the depolarization of the base of the ventricles.

The whole complex lasts between 60 and 90 ms. Simultaneously to this phase, atrial repolarization takes place but is masked by the ventricular depolarization.

T wave reflects ventricular repolarization but is not always visible since it is rather weak.

Another wave, called U wave, can be occasionally recorded and it is attributable to the repolarization of deep papillary muscles.

Heart rate can be inferred from ECG traces by evaluating the time that elapses from two consecutive R peaks.

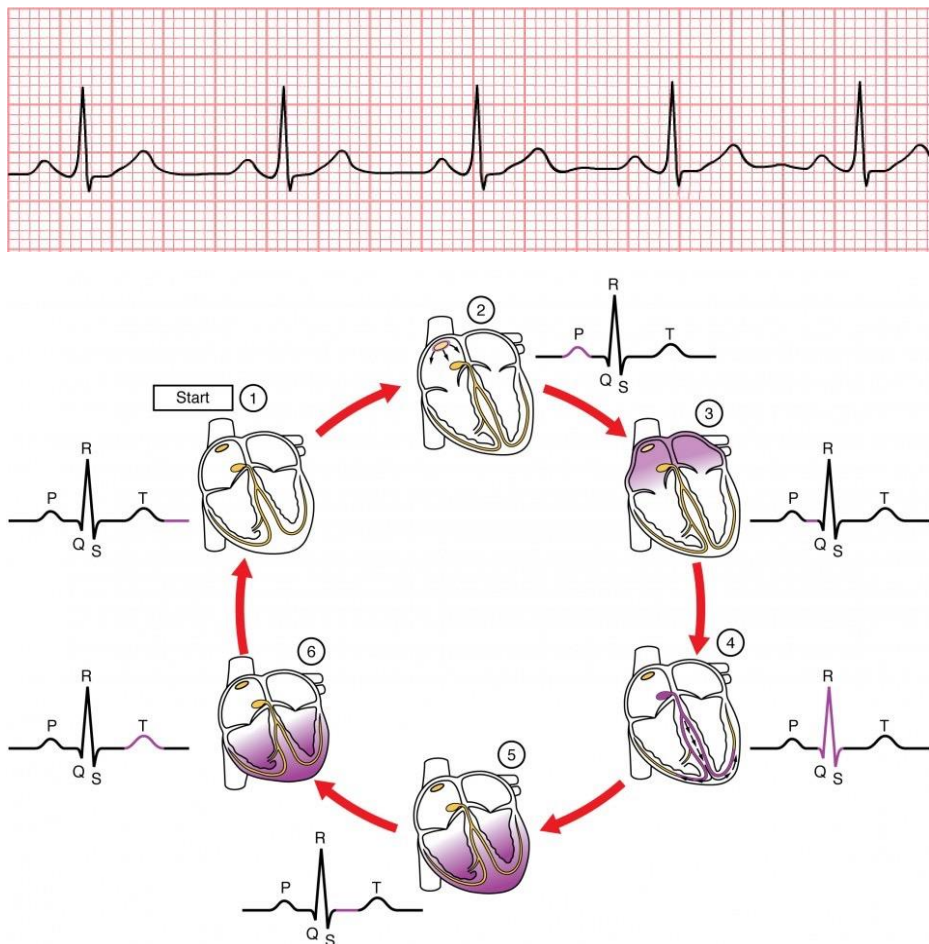


Figure 6. *The ECG trace reflects the cardiac electrical activity.*

TOP: Sample ECG trace of a healthy heart. BOTTOM: Representation of the cardiac electrical cycle and associate waves detected in the ECG.

Heart rate variability

Physiologically, basal heart rate (BHR, R-R intervals) is characterized by a beat-to-beat variability over a wide range which are described and quantified by the analysis of heart rate variability (HRV). A high variability is considered as a sign of a good adaptability, whereas lower variability is often a marker of abnormal balance and insufficient flexibility of the ANS²⁴ and is correlated with morbidity and mortality in many conditions and disease. Therefore, HRV analysis provides in a non-invasive way information about cardiac autonomic modulation²⁵ and overall compromised health²⁶. Despite in normal conditions the two branches of the ANS are in dynamic balance, autonomic imbalance, in which one branch predominates over the other, is associated with a lack of dynamic flexibility and health²⁷.

HRV is analyzed either by simple statistical methods (time-domain analysis) or by using computer algorithms (frequency-domain analysis) to detect slow (low-frequency modulations – parasympathetic activity) and fast (high-frequency modulations – sympathetic activity) changes occurring from beat to beat.

The action potential

The action potential (AP) is a rapid and reversible reversal of the electrical potential difference across the plasma membrane typical of excitable cells. It represents the basis for information processing, propagation and transmission.

APs occur in various types of animal cells²⁸, such as neurons (cell-to-cell communication), muscle cells (contraction) and endocrine cells (hormone release), as well as in some plant cells²⁹.

In the heart, the two main cell types, working myocytes and conducting cells, besides histological and morphological characteristics, display noticeable physiological differences, especially regarding their APs. This is due to the different tasks these cells must accomplish: while atrial and ventricular working cells must contract in order to maintain the pulsatile activity of the heart, conducting cells are responsible for the generation and the propagation of the electrical pulse.

Fast response action potential

This type of AP, peculiar of atrial and ventricular myocytes, is characterized by a very rapid depolarization (phase 0) and can be divided into 5 phases (**figure 7, Right**):

- Phase 0: it is a fast depolarization phase, due to the quick inflow of a depolarizing Na^+ current from the voltage-gated Na^+ channels. The trigger for this channels activation is the depolarization wave spread by the conduction system;
- Phase 1: it is a partial repolarization phase, caused by two main events: the activation of a K^+ transient outward current (I_{to}) and the voltage-dependent inactivation of Na^+ channels;
- Phase 2: also known as the plateau phase, it is typical of ventricular cells. Here, the inward L-type Ca^{2+} current (I_{CaL}) counteracts the transient outward K^+ current, keeping the membrane potential between 0 and -10 mV;
- Phase 3: as the I_{CaL} inactivates, a series of inward K^+ currents (I_{Kur} , a very rapid current peculiar of atrial myocytes, I_{Kr} , a fast current and I_{Ks} , a slow current) repolarize the cell to the resting potential;
- Phase 4: the membrane potential is maintained at the resting voltage of about -85 mV, primarily by an inward K^+ current named I_{K1} . The resting state is preserved until another electrical stimulus brings the voltage up to the threshold for the activation of voltage-gated Na^+ channels.

The main difference between atrial and ventricular APs lies in the duration of the plateau phase since this is indeed shorter or even absent in atrial myocytes. The discrepancy arises from the different amount of contraction power these cells must generate, which is definitely greater in the ventricles.

The Ca^{2+} inflow during the plateau phase is an extremely relevant phenomenon since it triggers the process of calcium-induced calcium release (CICR) which is, in turn, fundamental for the physical contraction of the sarcomeres. Briefly, after Ca^{2+} cations are carried inside the plasma membrane, they bind to the ryanodine receptors (RYRs) located in the sarcoplasmic reticulum (SR) leading to a massive release of other Ca^{2+} cations. As they reach their specific binding spots on troponin C, tropomyosin is removed from the contraction machinery allowing the formation of a strong bond between actin and myosin: the sarcomere contraction can now take place.

At the end of the process, SERCA (Sarcoplasmic Endoplasmic Reticulum Calcium-ATPase) pumps located on the membrane of the SR employ ATP in order to carry Ca^{2+} cations from the cytosol back to their location; in addition, calcium is also pumped outside the cell by Ca^{2+} -pumps located in the cell membrane³⁰.

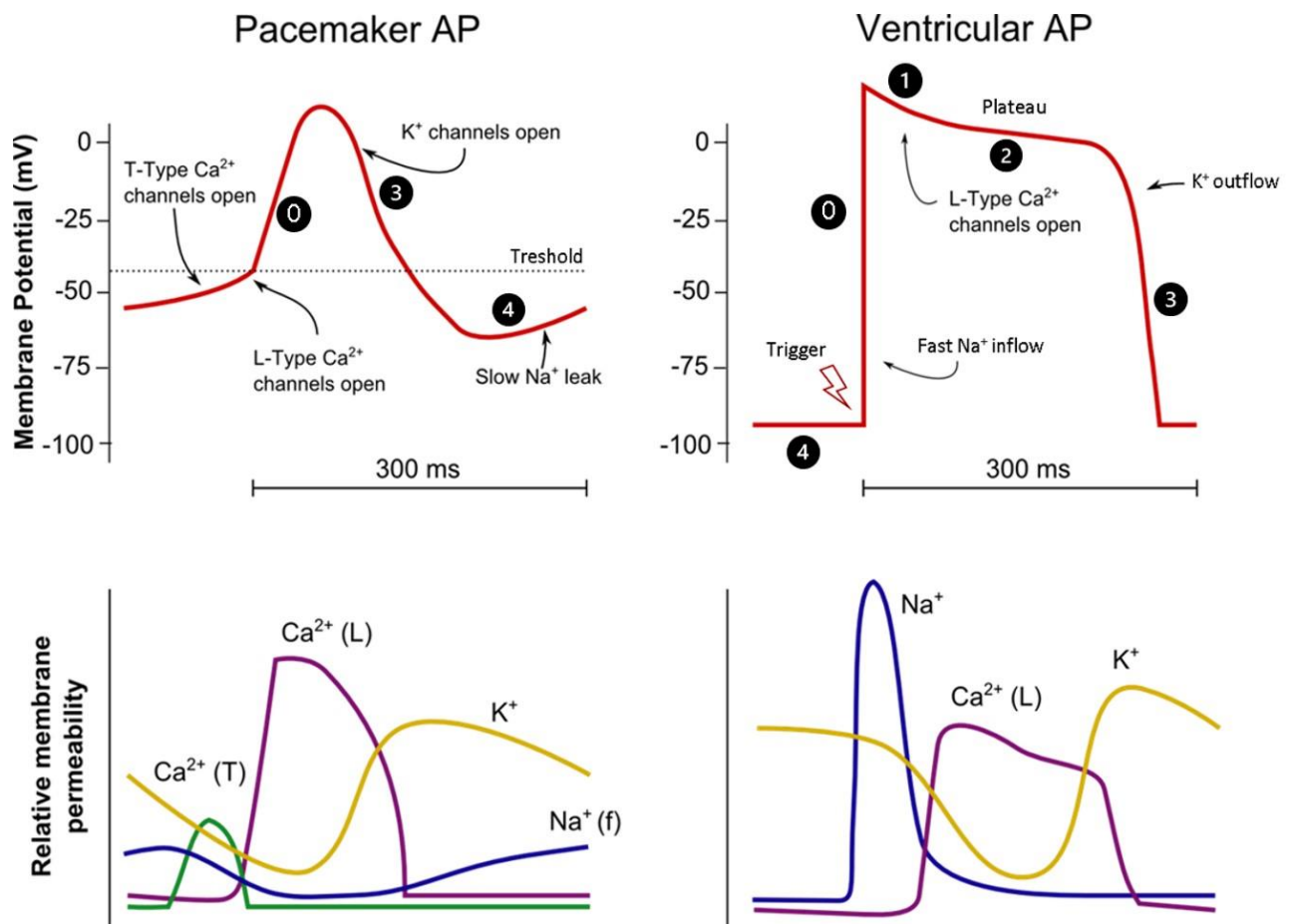


Figure 7. Comparison between slow and fast response AP shape and representation of the main currents involved.

According to their function, conducting cells and working myocytes are characterized by a different pattern of ion channels expression which results in a different AP shape (TOP). In the BOTTOM panel, the main currents involved in the processes are displayed.

Slow response action potential

This process is typical of pacemaker and conducting cells and, as for the previous phenomenon, it can be divided into distinct phases (**Figure 7, Left**):

- **Phase 0**: it is the main depolarization phase, led by the I_{CaL} current. It is slower compared to the phase 0 of fast response action potentials;
- **Phase 3**: the voltage is hyperpolarized by a combination of outward K^+ currents, such as I_{Kr} and I_{Ks} . Furthermore, L-type Ca^{2+} channels inactivate and switch to their closed-state. The K^+ currents involved in this phase cease their activity at the beginning of the following one (phase 4);

- Phase 4: when the repolarization phase (phase 3) comes to an end, the membrane potential reaches the maximal diastolic potential (MDP), defined as the most negative value reached during the entire cycle (about -60 mV). In this range of voltage, HCN channels begin to open, conducting a mixed Na^+ and K^+ inward current, the so-called '*funny*' or pacemaker current (I_f)³¹ which leads the slow diastolic depolarization phase. Following its activation, the membrane potential starts to rise, activating the T-type Ca^{2+} channels and finally the L-type Ca^{2+} channels, initiating a new cycle.

Since pacemaker cells are able to generate spontaneous and rhythmic beats, their AP lacks of a stable resting phase (phase 4). Moreover, unlike working myocytes whose task is to contract, these cells generate and transmit the electrical impulse throughout the heart so their AP lacks the plateau phase (phase 1-2), too.

The pacemaker 'Funny' current

First described in the late 70s in SAN myocytes³² and Purkinje fibers^{33,34}, the cardiac pacemaker '*funny*' (I_f) current has been extensively characterized for its role as the main generator and regulator of the early diastolic depolarization phase. Moreover, it is also involved in some of the basic neuronal function of the brain, such as dendritic integration³⁵, working and motor memory^{36,37} and synaptic transmission³⁸.

This current is named after its peculiar features: it is an inward-directed, voltage-dependent current, triggered by cell hyperpolarization at potential more negative than -40/-50 mV (in SAN cells). It is carried both by Na^+ and K^+ cations and reverses between -10 and -20 mV³¹. Furthermore, its activation and deactivation kinetics are sigmoidal functions of time³¹.

It has been observed that, during electrophysiological experiments in whole-cell configuration, the amplitude of this current undergoes a time-dependent reduction³¹. The cause of this phenomenon, called run-down, has not already been fully clarified, however, since it does not occur during perforated-patch studies, some authors suggested that it may be due to the loss (or excessive dilution) of intracellular components which regulate the channels in normal conditions^{39,40}. The physiological activity of the pacemaker current is strictly related to the intracellular concentration of the second messenger cyclic AMP (cAMP), a nucleotide involved in several cellular

processes which is highly controlled in synthesis (adenylyl cyclase) and degradation (phosphodiesterase)⁴¹. Direct binding of this molecule to f-channels increases their opening probability by shifting the activation curve towards more positive voltages, whereas low concentrations of the same gives rise to an opposite action⁴². This mechanism is the way through the ANS modulates heart rate in order to respond efficiently to rapid physiological demands. SAN cells express on their membrane both $\beta 1/\beta 2$ -adrenergic and M2-muscarinic receptors, respectively mediators of the sympathetic and parasympathetic nervous system activity. Since they share a specific transduction pathway, these receptors are pooled together with f-channels in membrane microdomains called *caveolae* in order to keep them in close proximity^{43,44}. Adrenergic agonists are able to increase the I_f current by stimulating an increase in cAMP production which results in a positive shift of the f-channels activation curve, thus increasing the slope of the diastolic depolarization phase and accelerating heart rate. Muscarinic agonists have opposite effects, causing a decreased slope of this phase and decelerating heart rate (**figure 8**).

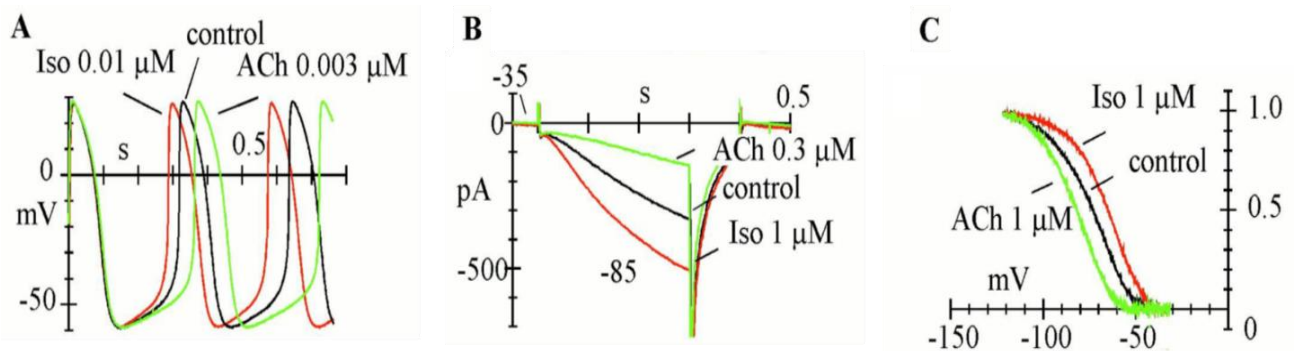


Figure 8. *Effects of autonomic modulations on APs and I_f current.*

Autonomic modulators, Isoprenaline (Iso) and Acetylcholine (ACh), are able to increase/reduce SAN cells firing rate (A). This effect is the direct consequence of the I_f current modulation (B) obtained through the shift of the activation curve of f-channels (C) (modified from Accili et al., 2002).

HCN channels

Structure and function

The hyperpolarization-activated, cyclic nucleotide-gated (HCN) channels represent a small family of cation channels expressed in the heart and in the central nervous system, cloned for the first time the end of the 90s⁴⁵. They are the molecular components of the I_f current, also described as I_h when associated to the neuronal environment.

Their structure resembles both voltage-dependent K^+ channels⁴⁶ and cyclic nucleotide-gated (CNG) channels⁴⁷ (**figure 9**). Specifically, HCN channels display a tetrameric structure⁴⁵ in which every monomer is composed by 6 transmembrane domains (S1-S6). Among these, S4 represents the voltage sensor since it incorporates a series of basic, positively charged amino acids.

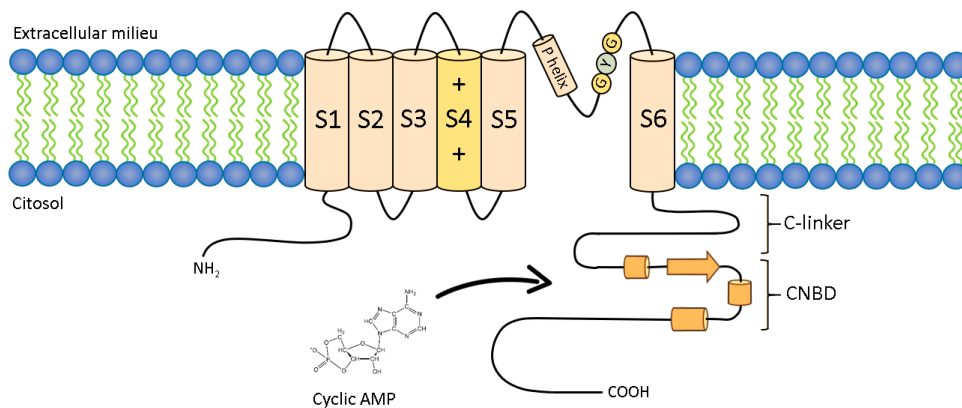


Figure 9. HCN channels structure.

Schematic representation an HCN monomer where the six transmembrane domains (S1-S6), the P-helix (fundamental for the generation of the pore), the GYG triplet (involved in ion selectivity process), the C-linker and the CNBD (mediator of cyclic nucleotides binding) are displayed.

The link between the S5 and S6 domain, called P-loop (or pore-loop), settles the pore in the tetrameric state⁴⁷; moreover, in this region is located the GYG triplet that represents the ionic selectivity filter of the channel⁴⁸. The N- and the C-terminus of the protein are both positioned in the cytosol and, notably, the C-terminus can be divided in two main regions: the C-linker and the cyclic nucleotide binding domain (CNBD). The first one connects the S6 domain to the CNBD and it's organized in 6 α -helices⁴⁸; the second one allows the channel to interact with cyclic nucleotides, especially with cAMP. This molecule binds the channel with a stronger bond when it is in open state^{45,49} causing structural changes in the whole protein with the result of increasing the open probability.

Four isoforms of HCN channels, encoded by four different genes, have been described to date (HCN1, HCN2, HCN3 and HCN4)⁴⁷. Nevertheless, all of them display a series of common features: they all switch to the open state during hyperpolarization, are permeable to both Na^+ and K^+ (with a Na^+/K^+ permeability ratio of about 0.2) and are able to directly bind cyclic nucleotides (even though HCN1 and HCN3 seem to be only mildly modulated). Moreover, all isoforms display structural similarity in the core region (80% identical); however, their N- and C-terminus

are substantially diverse⁵⁰, leading to relevant differences in their activation and deactivation kinetics, in the gating mechanism⁵¹ and in the sensibility to cyclic nucleotides^{45,52}. None of them display an inactivation-state⁵³ (**figure 10**).

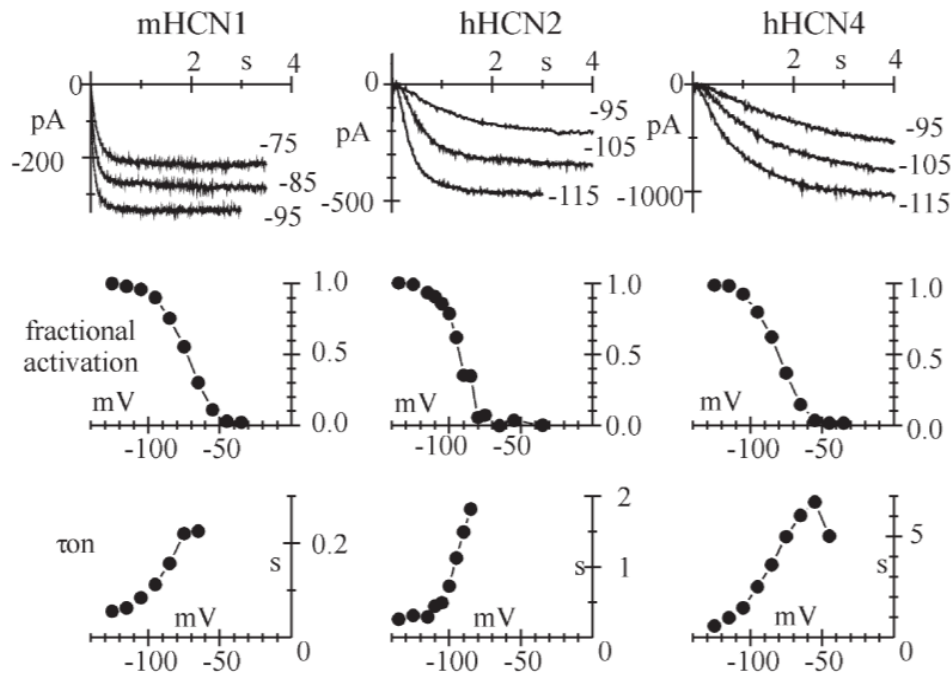


Figure 10. *Electrophysiological properties of HCN1-2-4 channels.*

I_f sample traces and current analysis of different HCN channels isoforms (mouse HCN1 – human HCN2 – human HCN4) expressed in HEK-293 cells. TOP: current traces recorded at the voltages indicated from a holding potential of -35mV. MID-DLE: mean activation curves; $V_{1/2}$ (mV): -73; -92; -81; respectively. BOTTOM: mean time constants of current activation (from Accili et al., 2002).

HCN1 is the less responsive isoform to cAMP, with a shift of 2/6 mV, compared to HCN2 and HCN4 (shift: 10/25 mV)⁵⁰. Regarding their location, while in the heart HCN4 and HCN2 are the main isoforms expressed, in the brain there is a higher presence of HCN1 and HCN2 (cortex, hippocampus and thalamus)⁴⁷.

HCN3 is the less investigated isoform: it shows a kinetics of activation which is faster than HCN4 but slower than HCN2 and a $V_{1/2}$ similar to HCN1. It displays only a minimal modulation by cAMP⁵⁴.

Pharmacology

Given the relevance that this ion channel family has in the generation of peacemaking, a lot of interest has been devoted to the research of pharmacological compounds able to modulate their action.

Caesium (Cs^+) has been the first molecule discovered to be able to block the channel, displaying a voltage-dependent action^{31,55}. However, since this substance is not specific for HCN channel, it could cause a series of side effects in the entire organism.

In recent years the quest for the so called “pure bradycardic” agents, i.e. drugs able to reduce heart rate without undesired side-effects, has gain more and more relevance. In spite of this, Ca^{2+} -antagonist and β -blockers are still the most common used drugs for the therapeutic reduction of heart rate although their mechanism of action leads to a reduced force of cardiac contraction that eventually leads to hypotension^{56,57}.

The first bradycardic drug discovered was Alinidine (ST-567, **figure 11**) which is able to prolong the diastolic depolarization of SAN cells through a negative shift of the activation curve of f-channel combined with a reduced conductance. However, since alinidine showed interaction with both K^+ and Ca^{2+} channels, it was soon abandoned in clinics^{58,59}.

Further studies performed on Verapamil (a Ca^{2+} -antagonist drug) led to the production of other compounds, such as Falipamil (AQ-A29), Zatebradine (UL-FS 49) and Cilobradine (DK-AH-269). Among these, Zetabradine (**figure 11**) displays a dose-dependent effect and a molecular mechanism that requires the channel to be in open-state. However, it also causes important central side-effects, since it binds also on the HCN channels located in the brain⁶⁰.

Another molecule that displayed an I_f -modulating effect is ZD7288 (**figure 11**) which causes a negative shift of the activation curve (0.3 μM : -16.2 mV) and reduces HCN channel conductance (0.3 μM : -52%) inducing an overall firing rate reduction (0.3 μM : -61% in SAN cells). Still, it displays minor interaction with K^+ and Ca^{2+} channels in the heart and in several regions of the central nervous system^{61,62}.

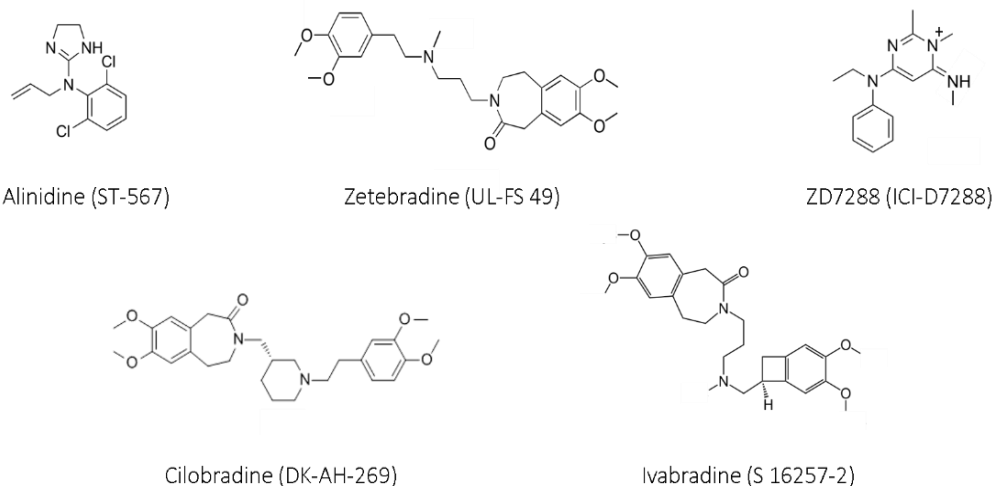


Figure 11. Molecular structure of some of the main HCN modulators.

Chemical structure of a selection of drugs able to interact with HCN channels. Among these only Ivabradine is still used in clinics.

Finally, the most selective molecule for HCN channels, able to reduce heart rate acting on the I_f current, is Ivabradine (S 16257-2, **figure 11**). At a concentration of 3 μM , in isolated rabbit SAN cells, it reduces the rate of spontaneous firing by 24%. Its bradycardic action is associated with a decreased slope of the early diastolic depolarization phase and a slight increase of the action potential duration (+9%)¹. Further experiments confirmed that Ivabradine strongly reduced the I_f current (-60% at steady-state, **figure 12, bottom**), without affecting T- and L-type Ca^{2+} and K^+ channels². Similarly to Zatebradine, also Ivabradine may cause visual symptoms (phosphenes) which, however, are well tolerated.

Detailed investigations on the blocking mechanism of native sinoatrial and HCN channels (**figure 12, top**) demonstrated that Ivabradine can access its blocking site only when the channels are in the open state (state-dependency), and that the process is favored by depolarization; yet, a functional block is strictly dependent on the presence of an outward flow of current through the channel (current-dependency). Since f-channels open in hyperpolarization but the block is favored by depolarization, the binding of the drug to the blocking site develops quickly and strongly when channels cycle through open/closed states at high rates (use-dependency).

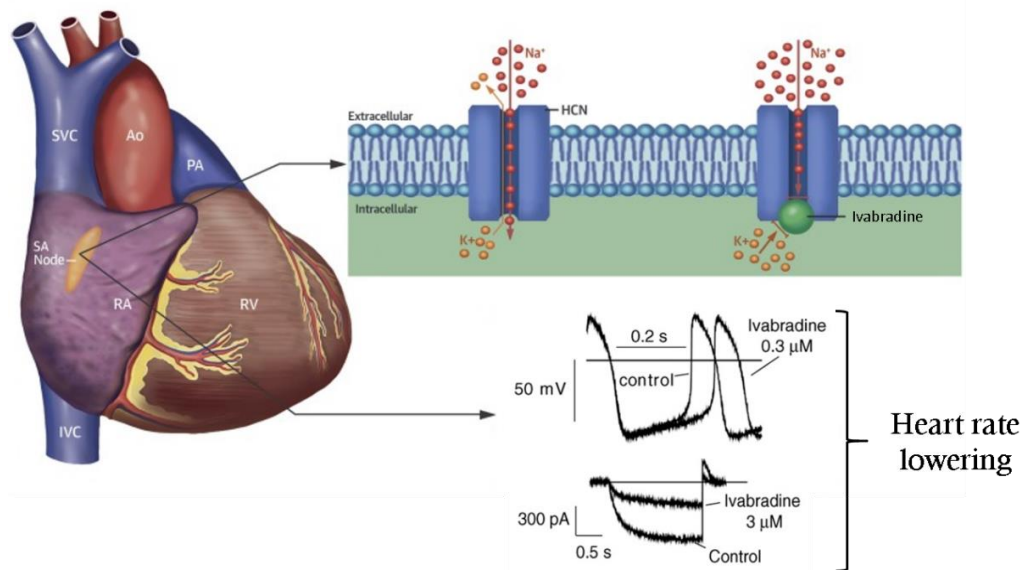


Figure 12. Mechanism of action and electrophysiological effects of Ivabradine.

TOP: representation of the Ivabradine block on HCN channels; BOTTOM: effects of Ivabradine perfusion on rabbit spontaneous APs ($0.3 \mu\text{M}$: $-16.2 \pm 1.5\%$) and on the I_f current ($3 \mu\text{M}$: $\sim -60\%$) the eventually lead to the reduction of the overall heart rate (modified from Koruth et al., 2017; data from Bucchi et al., 2007).

Clinical studies have demonstrated that Ivabradine can be a useful pharmacological tool for angina symptoms prevention and the underlying ischemia^{3,63}. Finally, the SHIFT study demonstrated that this drug is associated with a reduced risk of cardiovascular death or hospital admission for worsening heart failure⁶⁴.

Voltage-gated Na^+ channel $\text{Na}_V1.5$

Voltage-gated Na^+ channels play a key role in membrane excitation both in cardiomyocytes and neurons. These molecules are involved in a plethora of phenomena, however their structure is very similar.

$\text{Na}_V1.5$ is the cardiac most expressed isoform and is encoded by the *SCN5A* gene, located on chromosome 3p21. Its transcript is abundant in working myocardium but almost absent in conduction system. The protein consists of 2015-2016 amino acids and its molecular weight is about 220 kDa.

Every channel is composed by an α -subunit (**figure 13**) organized in 4 homologous structural domains (I-IV), each formed by 6 transmembrane α -helix segments (S1-S6). Segment S4 serves

as the voltage sensor (it contains a variable motif of positively charged amino acid) while the linker between S5 and S6 is fundamental for the generation of the pore and contains the selectivity filter. The 3 linkers that connect the domains, as well as the C- and the N-terminus are cytoplasmic.

In order to function properly, every α -subunit is associated with β -subunits which modulate its function. Those small molecules are encoded by 4 different genes (SCN1B-4B) and consist of an extracellular N-terminal region that presents an immunoglobulin-like domain, a single trans-membrane segment, and an intracellular C-terminal domain (**figure 13**). β subunits play an important role in the modulation of the channel function regulating the voltage-dependence of activation and inactivation kinetics and the expression levels, increasing the trafficking towards the membrane¹⁵.

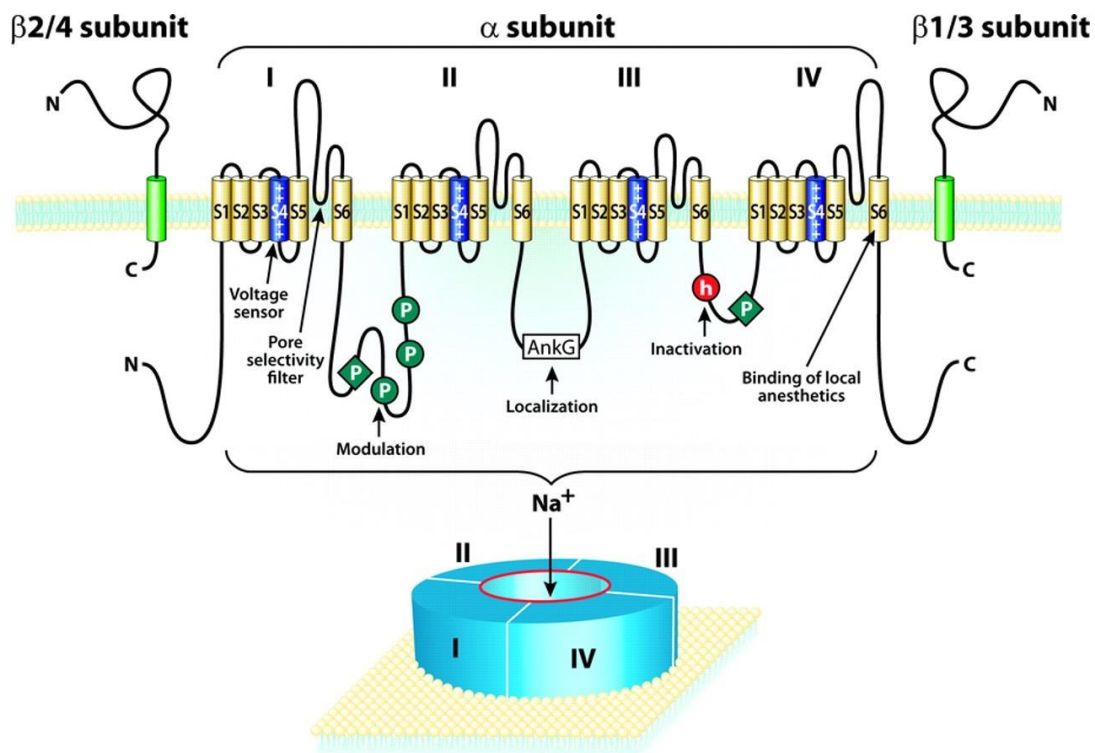


Figure 13. Voltage-gated Na⁺ channels structure.

Schematic representation of the primary structure of a voltage-gated Na⁺ channel; here are presented the α - and β -subunits, phosphorylation (P, green) and localization (AnkG) sites and the 'hinged lid' motif (h, red), fundamental for the process of fast inactivation (from Benarroch, 2006).

Na⁺ channels selectivity is based both on ion dimensions and on electrical properties: while the first is determined intrinsically by the channel itself, the latter is due to the interaction between amino acids residues (coordination sites) in the pore region. Only if the ion is properly stabilized

can pass through the coordination sites and enter the cells, if not it is repelled away. About 20 amino acids located inside the P-loop that connects the segments S5 and S6 are involved in the process. This mode of ion flow is called multi-ion-single-file pore; the flow is only allowed to a Na^+ cation associated with two water molecules⁶⁵.

Not only ion passage is strictly controlled, but the current flow depends on the voltage in two ways. Briefly, the channel conformation can switch between 3 states: open, closed and inactivated. As mentioned before, at a resting potential of about -85mV the channel is in closed state; only when the voltage rises over the activation threshold (-60/-70mV) a conformational change occurs in S4 segments causing the opening of the channel (open state) so that the current is allowed to flow inwardly depolarizing the cell potential. However, the voltage increase also triggers another gate of the channel (mediated by segment S6) which prevents the current flow (inactivated state). Only once the voltage has returned to resting values the channel can switch back to the closed state and subsequently re-open (recovery from inactivation).

Finally, during the biosynthetic trafficking of the channel, several post-translational modifications may occur, among which: phosphorylations, arginine methylations, N-term acetylations and glycosylations. Furthermore, several slicing variants have been reported⁶⁶.

TRADITIONAL CHINESE MEDICINE

INTRODUCTION

Traditional Chinese medicine

Traditional Chinese medicine (TCM, or *Zhōngyī*) is one of the oldest organized healing systems in human history and is based on a holistic view of both the disease state and the associated therapy. It was established in ancient China more than 2000 years ago but it is still used as a medical practice. It includes Chinese herbal medicine (*zhōngyào xué*), acupuncture (*zhēnjiǔ*), Chinese massage (*tui na*), mind/body exercises (*Tai Chi, Qigong*, etc.), and dietary therapy (*shíliáo*). In the TCM approach any disease state represents the loss of the perfect balance in the body. According to this view, the equilibrium represents a harmonic state between opposite but complementary elements of the same phenomenon; an idea that is applied both on nature and the organism. These concepts are well explained by the theory of *Yin-Yang*, one of the two fundamentals principles of TCM.

The other pillar is *Wuxing* (or *wǔ zhǒng liúxíng zhī qì*), known in western countries as ‘*the theory of the five elements*’. It is a fivefold conceptual scheme used to explain a wide range of phenomena, from cosmic cycles to interactions between organs. The five elements, or phases (fire - *huǒ*, earth - *tǔ*, metal - *jīn*, water - *shuǐ*, wood - *mù*), are mutually regulated and are associated to specific human organs, influencing the environment and the physiological and pathological interactions between them⁶⁷ (**figure 14**). For these reason, the perfect synthesis of TCM pharmacology is based on complex drugs composed by a mixture of different elements/herbs whose aim is to target the causes of the disease, modulate other aspects of the body wellness and contrast toxicity^{68,69}.

Although this philosophical view is far from having a scientific base (and according to the western science it should and must be rejected) it is undoubtedly true that the pharmacology associated with TMC has a long history and in several cases the results are experimentally verified.

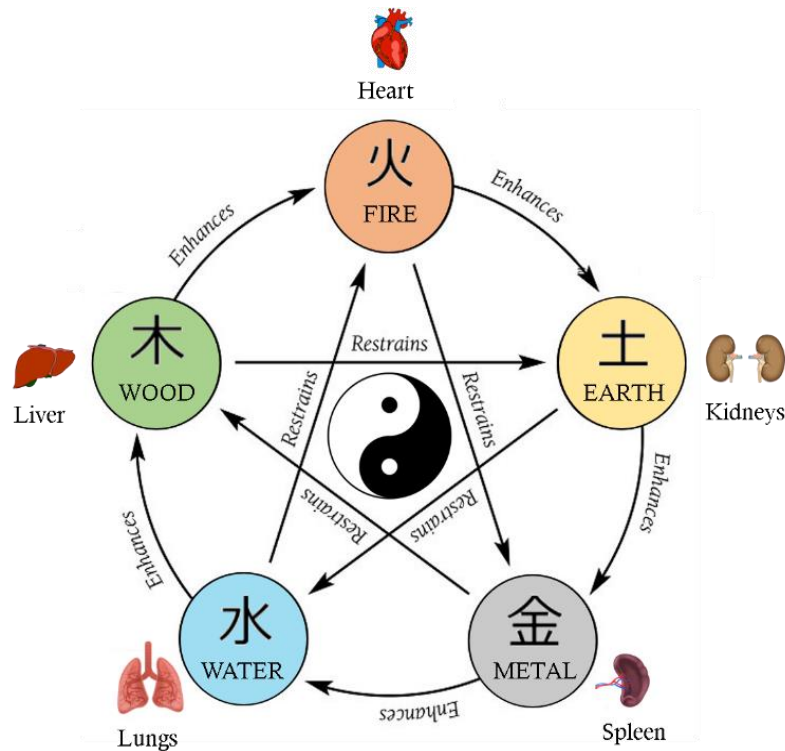


Figure 14. Diagram of the interaction between the five elements in *Wuxing*.

In *Wuxing* the five phases are linked together by the Creation/Generation cycle (outer) and by the Control/Destruction cycle (inner). Here are also displayed the main organ associated with each element. In the middle is reported the Taijitu (*tàijítú*), sum of the *Yin-Yang* philosophy.

Western medicine is founded on a different perspective since it focusses on the identification of the specific molecular mechanisms associated with the disease and defines this level as its therapeutic target. These apparently distant interpretations are now converging thanks to the bridge provided by modern biochemical and molecular analyses, which can be applied to TCM drugs; indeed, the discovery of novel active principles can ideally be exploited also by western medicine^{67,70-72}.

In the last years, several TCM compounds have acquired importance in Western countries for their therapeutic potential. Berberine, for instance, is an alkaloid found in many medicinal plants of the *Berberis* and *Coptis* genera (**figure 15A**) which displayed important cardiovascular effects since it induces the vasodilatation of smooth muscles^{73,74} and has been reported to exert both positive inotropic and negative chronotropic actions, blocking I_{to} and I_{K1} currents^{75,76}.

Another TCM cardiac regulator is Wenxin Keli, a mixed herb extract reported to prevent the induction of persistent atrial fibrillation in isolated canine right atria preparations⁷¹. It generates

a complex intracellular cascade resulting in the modulation of multiple ion channels with different potencies, mainly acting on peak and late Na^+ current, with some effect on I_{t0} and I_{CaL} , too⁷⁷.

Notably, the most famous contribution of TMC to modern medicine is Artemisinin (*Quinghao*)⁷⁸, an antimalarial molecule extracted from *A. annua*, a small herbaceous plant (**figure 15B**). Despite its mode of action is still not fully understood, the absence of toxic side-effects and its proven specific potency, led this compound to be recognized as one of the most effective and recommended treatment regimens for uncomplicated malaria^{79,80}. In 2015, the Chinese pharmacologist that was able to isolate Artemisinin, Tu Youyou, was awarded with the Nobel prize in physiology or medicine.

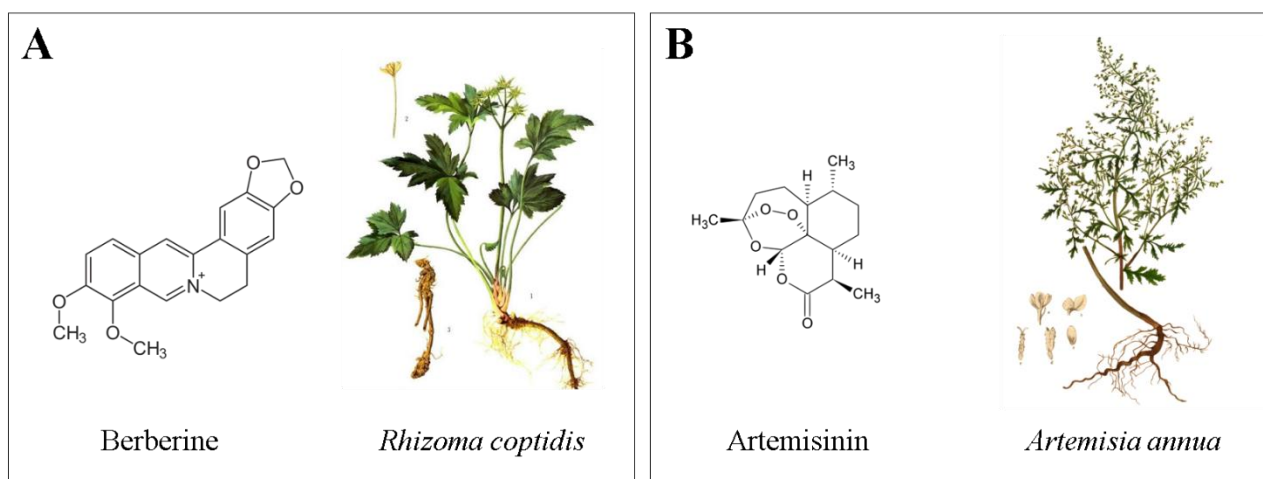


Figure 15. *Berberine and Artemisinin are two example of bioactive molecules isolated from TCM herbs.*

(A) Molecular structure of Berberine and the herb from which it was first isolated, *R. coptidis*. (B) Structure of the antimalarial drug Artemisinin and representation of the *A. annua* herb.

Tongmai Yangxin

Tongmai Yangxin (TMYX) is a TCM drug currently used in China to treat several cardiovascular pathologies (coronary artery diseases, palpitation, heart failure and angina) listed in the Chinese Pharmacopeia 2015⁴ (**figure 16**). According to TCM it functions as a *qi* replenisher, able to nourish *Yin*.

It is a mixture of 11 different compounds both of botanical (*Fructus Jujubae*, *Radix Codonopsis*, *Radix Rehmanniae*, *Rhizoma Glycyrrhizae*, *Ramulus Cinnamomi*, *Raxid Polygoni Multiflori Praeparata*, *Caulis Spatholobi*, *Radix Ophiopogonis*, *Fructus Schisandrae Chinensis*) and animal (*Colla Corii Asini*,

Plastrum Testudinis) nature, originally developed from a well-known herb pair called “*GuiZhi-GanCao*”, documented in “*Shang-Han-Lun*” by Zhongjing Zhang in the Eastern Han Dynasty.



Figure 16. *Tongmai Yangxin pills.*

TMYX is currently used in TCM to treat a wide range of disorders and is usually sold in film-coated concentrated water pills (1g per 10 pellets).

Recently, biochemical analysis revealed that TMYX contains at least 80 bioactive molecular components among which flavonoids, coumarins, iridoid glycosides, saponins and lignans⁸¹, while metabolomics analysis, carried out in a registered clinical trial on stable angina patients has highlighted a reduced serum presence of markers related to cardiac metabolic disorders, oxidative stress, and inflammation^{4,6}.

In addition to this cardio-protective role, TMYX is also used as an antiarrhythmic agent⁴; however, the mechanisms underlying this action have never been investigated.

Background

A few years ago, our laboratory, in collaboration with Le Ren Tang Pharmaceutical Factory (Tianjin, China), started an investigation on TMYX with the objective of unravel the molecular mechanism at the base of its cardiac rate regulation properties.

When perfused on rabbit SAN myocytes, TMYX induced a dose-dependent and fully reversible rate slowing of the spontaneous AP activity (**figure 17A**). The analysis of the effect of different doses led to the generation of a dose-response curve of rate (**figure 17B**), obtained by fitting the experimental points with the Hill equation ($y=y_{max}/(1+(k/x)^h)$ where y_{max} is the maximal effect, x is the drug concentration, k is the drug concentration eliciting half-maximal block and h is the Hill factor).

As reported in **figure 17C**, the reduction in the AP rate is mainly due to a decreased slope of the early diastolic depolarization (EED) phase while the take-off potential (TOP) and the maximum

diastolic potential (MDP) were not altered. A slight increase has been detected in the action potential duration (APD).

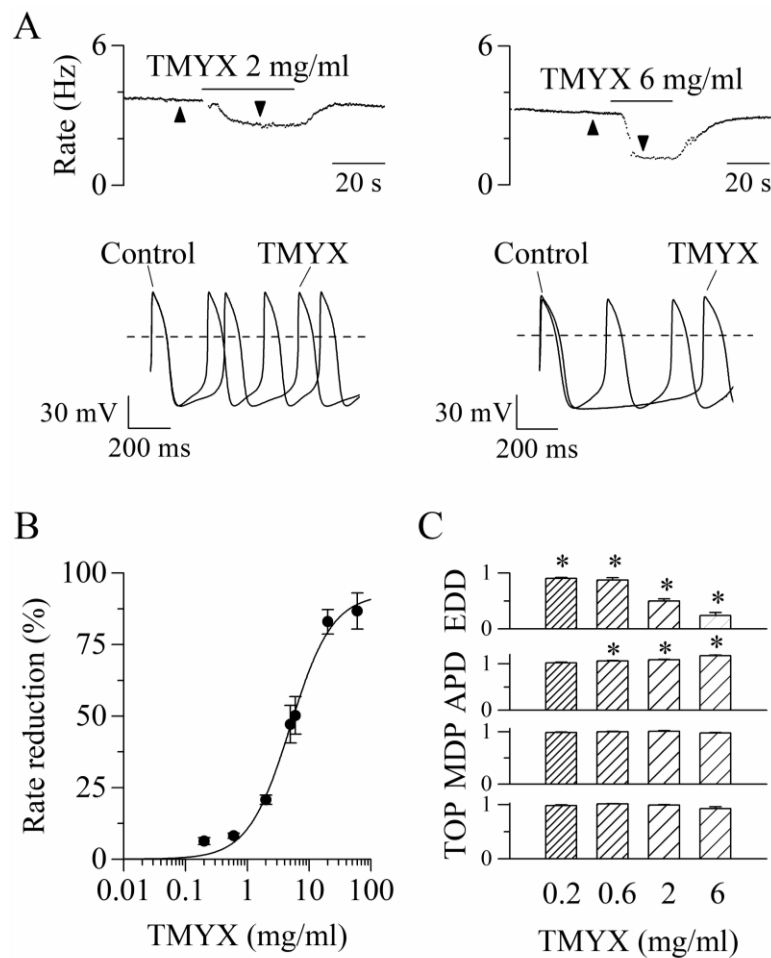


Figure 17. TMYX slows the spontaneous AP rate of rabbit SAN myocytes by reducing the slope of the EDD phase.

(A) Representative time-courses (TOP) and sample AP traces (BOTTOM) in control conditions and in the presence of TMYX (2 and 6 mg/ml). The arrows in the time-course panels, here and in following figures, indicate the time of recording of the sample traces. (B) Dose-response curve of rate reduction induced by TMYX (0.2, 0.6, 2, 5, 6, 20, 60 mg/ml; $n=68$). The Hill fitting (full line) yielded the following values: $y_{max} = 92.7\%$, $k = 4.9$ mg/ml, and $h = 1.3$. (C) Effects of TMYX on the main AP parameters (EDD, APD, MDP, and TOP; $n=7-12$) normalized to the corresponding control values. $p < 0.05$ vs control, Student's Pair t-Test (from Piantoni et al., 2020 - submitted).

Since I_f current is one of the key players in the generation of this process, an extensive analysis was carried out and, surprisingly, TMYX displayed a double opposite effect on the current density (figure 18A): a decrease at -65 mV (due to a leftward shift of the activation curve, figure 18B) and an increase at -125 mV (caused by an increase in channels maximal conductance, figure 18C). However, the mean steady-state curve (figure 18D) demonstrates that at physiological

potentials (< -80 mV) the contribution of the leftward shift of the activation curve prevails over the conductance increase, and the overall effect of the drug is a reduced current density.

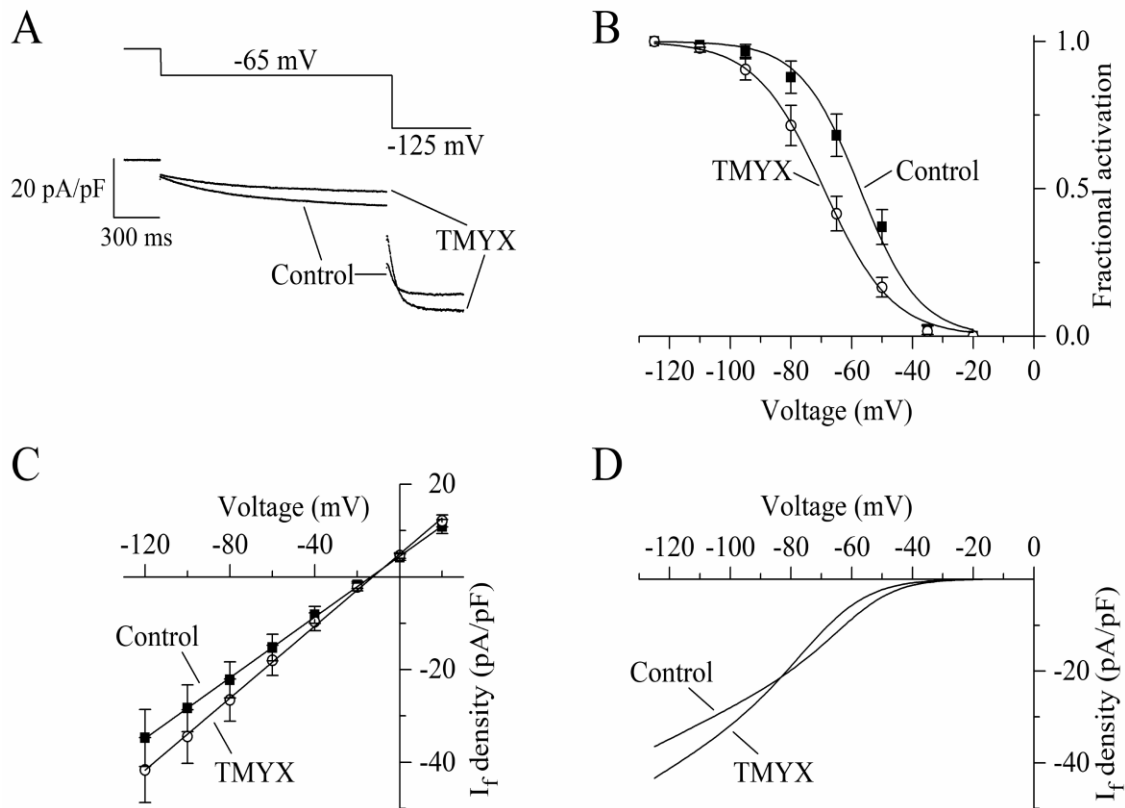


Figure 18. Dual action of TMYX on I_f current.

(A) Representative traces (BOTTOM) elicited by a double-step protocol (TOP) before and during TMYX (6 mg/ml) perfusion in whole-cell configuration. (B) Voltage-dependent activation curves recorded in control conditions and during TMYX perfusion ($n=7$). Boltzmann fitting of data-points (full lines) yielded the following half-activation values ($V_{1/2}$) and inverse-slope factors (s): -57.3 mV and 9.8 mV (Control) and -69.2 mV and 11.3 mV (TMYX); the shift of the curves is statistically significant (F-Test; $p<0.05$). (C) Mean fully-activated current/voltage (I/V) relations measured before and during drug perfusion ($n=5$ cells). Linear fitting yielded reversal potentials of -13.6 mV and -12.7 mV in control and in the presence of TMYX, respectively. The slopes (0.328 and 0.389 (pA/pF)/mV, respectively) of the I/V fitting lines are significantly different (linear regression analysis test; $p<0.05$). (D) Steady-state I/V fitting curves obtained by multiplying the activation curves (Boltzmann fitting in panel B) and fully activated I/V relation (linear fitting in panel C) in control condition and in the presence of the drug (from Piantoni et al., 2020 - submitted).

Since a negative shift of the I_f current activation curve is the final effect of the ACh pathway too, a series of experiment were carried out in order to observe if these two molecules display a common mechanism of action. Still, TMYX appear not to bind the muscarinic receptor since the ACh inhibitor Atropine did not modify the action of TMYX. However, detailed investigations demonstrate a progressive loss of modulatory efficacy of TMYX as the intracellular cAMP content increases (table 1).

cAMP (μM)	Basal	10	100
TMYX- induced I_f current reduction, mean \pm SEM (%)	49.1 \pm 3.0	37.9 \pm 5.1	2.3 \pm 3.3

Table 1. A progressive loss of the modulatory efficacy of TMYX (6 mg/ml) correlates with the intracellular cAMP content increases. I_f current traces were elicited through hyperpolarizing steps at -65mV with 3 different cAMP concentrations dissolved in the patch pipette: basal (0), 10 and 100 μM ; n=6, all conditions are significantly different, $p < 0.05$.

In order to further study this phenomenon, TMYX action was observed in inside-out configuration (**figure 19**). The results revealed that the drug is not able to bind f-channels in the absence of cAMP, indeed, its presence is fundamental for TMYX efficacy since the drug acts as a surmountable competitive antagonist of the second messenger binding to the CNBD of the channels.

In conclusion, TMYX slows spontaneous rate of SAN cells and, if appropriate doses are used, the underlying mechanism is a selective depression of the diastolic depolarization operated through an antagonistic action on cAMP-induced f-channel activation. In addition, targeting the cAMP binding domain is an interesting perspective for selective modulation of HCN channels since it will reduce the possibility of unspecific interference with other channels⁸². Although TMYX is composed by several molecules, the mechanism described is compatible with the action of a single molecule.

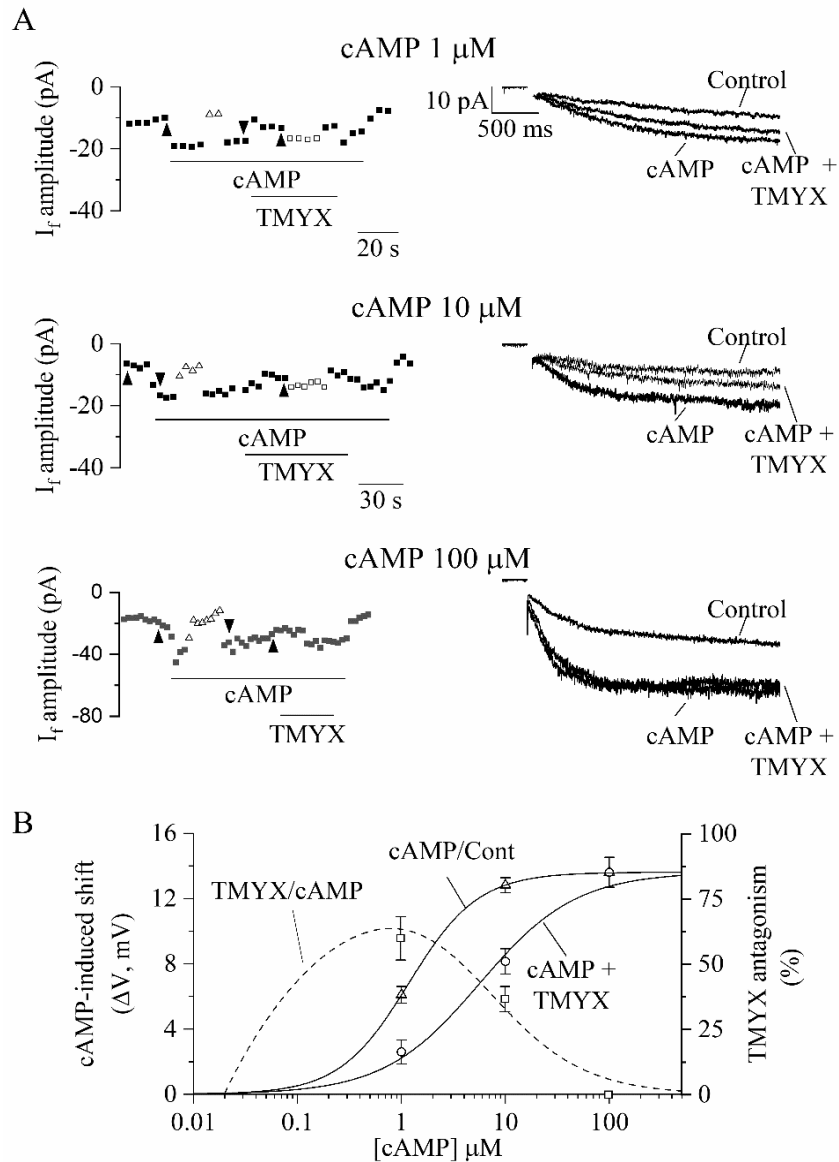


Figure 19. TMYX modulates the I_f current by antagonizing the cAMP-induced voltage-dependent I_f modulation.

(A) Sample time courses (LEFT) and current traces (RIGHT) of I_f current amplitudes recorded in inside-out macro-patches during repetitive hyperpolarizing steps to -105 mV; cAMP (1, 10, 100 μM , $n=4-6$) was perfused alone (cAMP) or in combination with a fixed dose of TMYX (6 mg/ml, cAMP+TMYX). Filled triangles and empty squares represent current amplitudes observed after manual corrections of the applied voltage (ΔV) to compensate for (and evaluate) both the effect of cAMP and the ability of TMYX to reduce cAMP modulation.

(B) (Right Y-axis): cAMP-induced shifts of the I_f activation curve obtained in the presence of cAMP alone (filled triangles) and of cAMP+TMYX (6 mg/ml, empty squares). The continuous lines represent dose-response Hill fittings of experimental data-points (13.6 mV was the maximal shift experimentally measured and therefore was taken as y_{max} for both conditions). (Left Y-axis): TMYX-induced fractional inhibition of cAMP modulation of the I_f current calculated as derived from experimental measures ($\Delta V_{TMYX/cAMP}/\Delta V_{cAMP}$, empty circles) and extrapolated from Hill Fittings ($\text{Hill}_{cAMP}-\text{Hill}_{cAMP+TMYX}/\text{Hill}_{cAMP}$, dashed line) (from Piantoni et al., 2020 - submitted).

AIMS

Pharmacological reduction of heart rate is often a fundamental treatment for cardiomyopathies, however, administration of β -blockers and Ca^{2+} -antagonists is usually the clinical approach to these diseases. Unfortunately, these drugs cause undesired and frequently intolerable side-effects, hence the quest for specific molecules able to regulate cardiac rhythmicity is considered a priority in the biomedical field. To date, the only drug used in clinics that acts on SAN rate is Ivabradine.

In recent years, several compounds used in Traditional Chinese Medicine (TCM) have acquired significance also in Western countries for their proven therapeutic properties. As described in the '*Background*' section, previous studies performed in the laboratory where I spent my Ph.D. internship have unravelled the molecular mechanism by which Tongmai Yangxin (TMYX), a TCM drug, accomplishes its bradycardic action. Still, in order to be used as a therapeutic agent also in Western medicine, the bioactive molecule responsible for this action must be isolated and characterized.

The aim of this scientific project is therefore to identify this molecule/s and, in future, to further analyse its effects both *in-vitro* (on SAN myocytes/HCN channel isoforms) and *in-vivo* (on the murine/human model). In order to accomplish this aim we started a collaboration with the group of prof. Yi Wang of the Zhejiang University (Hangzhou, China).

MATERIALS AND METHODS

Animals

All procedures performed were in accordance with the Italian DL. 26/2014 and the European directive 2010/63/UE, regarding the protection of animals used for experimental and other scientific purposes.

Experiments were performed on freshly isolated SAN myocytes from young (5 weeks old) female albino rabbits (NZW, from Charles River Europe) of about 0.8-1.2 Kg weight. All efforts were made to reduce the sample size and minimize animal suffering.

Cells isolation

Animals were anesthetized with an intramuscular injection of Xilagesic (Carlier – Xylazine 2%, 0.15 ml/kg), euthanized with an intravenous injection of sodium thiopental (MSD Animal Health, 60 mg/kg) and exsanguinated immediately after. The heart, quickly removed, was placed in prewarmed (37°C) Tyrode solution (all solutions are described in **table 2**) containing 1000 units of heparin to prevent blood clots formation, and finally, after surgical isolation, the SAN tissue was cut into 5-6 stripes. In the first phase of the cell isolation protocol, the tissue is washed three times with a Ca^{2+} -free, low- Mg^{2+} solution (solution 2 in **table 2**) and kept in an enzymatic solution (solution 3 in **table 2**) containing collagenase, protease and elastase at 37°C for 20/25 minutes, in order to degrade intercellular matrix and loosen cell-to-cell adhesions to facilitate the following mechanical dissociation procedure. The next step consisted in rinsing the stripes 3 times in a high- K^+ , low- Na^+ , Ca^{2+} -free and Mg^{2+} -free solution (solution 4 in **table 2**). Lastly, the tissue undergoes mechanical shacking for about 10 minutes at 37°C in the same solution^{83,84}.

Before starting the patch-clamp experiments, isolated cells were gradually readapted to proper extracellular Ca^{2+} and Na^+ concentration by adding increasing volumes of the following solutions: Tyrode and albumin 1 mg/ml; NaCl 10 mM, $CaCl_2$ 1,8 mM⁸³.

SAN myocytes were stored for the day at 4°C. During the experiments, cells were plated in a 35-mm plastic Petri dish and perfused with Tyrode solution at a stable temperature of $35\pm 0.5^\circ C$.

Solutions					
	1	2	3	4	Pipette
	Tyrode	Ca^{2+} -free, low- Mg^{2+}	Enzyme	Dispersion	Intracellular solution
PH	7.4	6.9	6.9	7.4	7.2
NaCl	140	140	140	—	10
KCl	5.4	5.4	5.4	20	—
KOH	—	—	—	80	—
CaCl ₂	1.8	—	0.2	—	2
MgCl ₂	1	0.5	0.5	—	2
KH ₂ PO ₄	—	1.2	1.2	10	—
HEPES-NaOH	5	5	5	—	10
HEPES-KOH	—	—	—	10	—
EGTA-KOH	—	—	—	0.1	5
D-Glucose	5.5	5.5	5.5	—	—
Collagenase (U/ml)	—	—	224	—	—
Elastase (U/ml)	—	—	1.42	—	—
Protease (U/ml)	—	—	0.45	—	—
Glutamic acid	—	—	—	70	—
β -Hydroxybutyric acid	—	—	—	10	—
Taurine	—	50	50	10	—
Albumin (mg/ml)	—	—	1	1	—
GTP	—	—	—	—	0.1
ATP	—	—	—	—	2
Phosphocreatine	—	—	—	—	5
Aspartic acid (K^+ salt)	—	—	—	—	130

Table 2. Solutions used for cell dispersion, perfusion and pipette filling (concentrations in mM, unless other indications). All salts and powders were purchase from Sigma-Aldrich, Merck KGaA (Collagenase from Worthington Biochemical).

Patch-clamp solutions

Spontaneous APs were recorded from single cells or small uniformly beating aggregates perfused with a normal Tyrode solution. A similar solution was employed to record the I_f current in whole-cell condition with the addition of $BaCl_2$ (1 mM) and $MnCl_2$ (2 mM) to the extracellular Tyrode in order to block contaminating K^+ and Ca^{2+} currents. The resistance of patch pipettes used in whole-cell experiments measured 3–5 M Ω ; smaller pipettes (7–9 M Ω) were used during APs recordings.

TMYX was provided by Le Ren Tang Pharmaceutical Factory (Tianjin, China) as a dry powder. A stock solution was prepared daily by dissolving the appropriate amount of substance in water (~80°C for 15 minutes); this solution was then filtered (pore size: 0.45 μ m) to remove undissolved components. This stock solution was used to prepare the test solutions at the desired concentrations.

Fraction 1-4 (F1-4) were obtained by the group of prof. Y. Wang from the Pharmaceutical Informatics Institute of Zhejiang University (Hangzhou, China) through column chromatography with gradient elution (**figure 20**). Briefly, 10g of TMYX extract (obtain from 50g of TMYX pills) were dissolved in 20ml of methanol and the supernatant was loaded onto an ODS column (YMC Co.). Subsequently, the column was eluted with 1.5L of purified water and increasing concentrations of methanol (20-60-100%). The resulting solutions were collected and concentrated under reduced pressure with a rotary evaporator to about 20 ml. For what concerned patch-clamp experiments, since F1 is a hydro-soluble compound (mostly composed by sugars), it was dissolved in water and diluted in the Tyrode solution. Fractions 3 and 4 were instead first dissolved in DMSO then diluted in Tyrode solution (the final dilution of DMSO was 1:1000 in order to avoid toxic effects on cells).

The preparation of sub-fractions (F1-1 to F1-4) was carried out by preparative liquid chromatography (Agilent 1200 series HPLC system) coupled with an ELSD detector (**figure 20**). Chromatographic separation was performed on a Prevail Carbohydrate ES column (5 μ m, 10 \times 250 mm) at a temperature of 35 °C. Gradient elution was conducted with water and acetonitrile (0 min, 20%; 10 min, 20%; 30 min, 30%; 60 min, 50% and 65 min, 50%). The flow rate was 0.8 ml/min and injection volume was 100 μ l. The time period for taking these resulting solutions is as follows: F1-1: 0-10 min; F1-2: 10-18 min; F1-3: 18-40 min; F1-4: 40-54 min. The total injection volume was about 6 ml. Finally, the fractions were concentrated under reduced pressure with a rotary evaporator to 2 ml and finally freeze-dried to prepare lyophilized powders. Since these

sub-fraction were obtain from F1, they were simply dissolved in the Tyrode solution at the desired concentration.

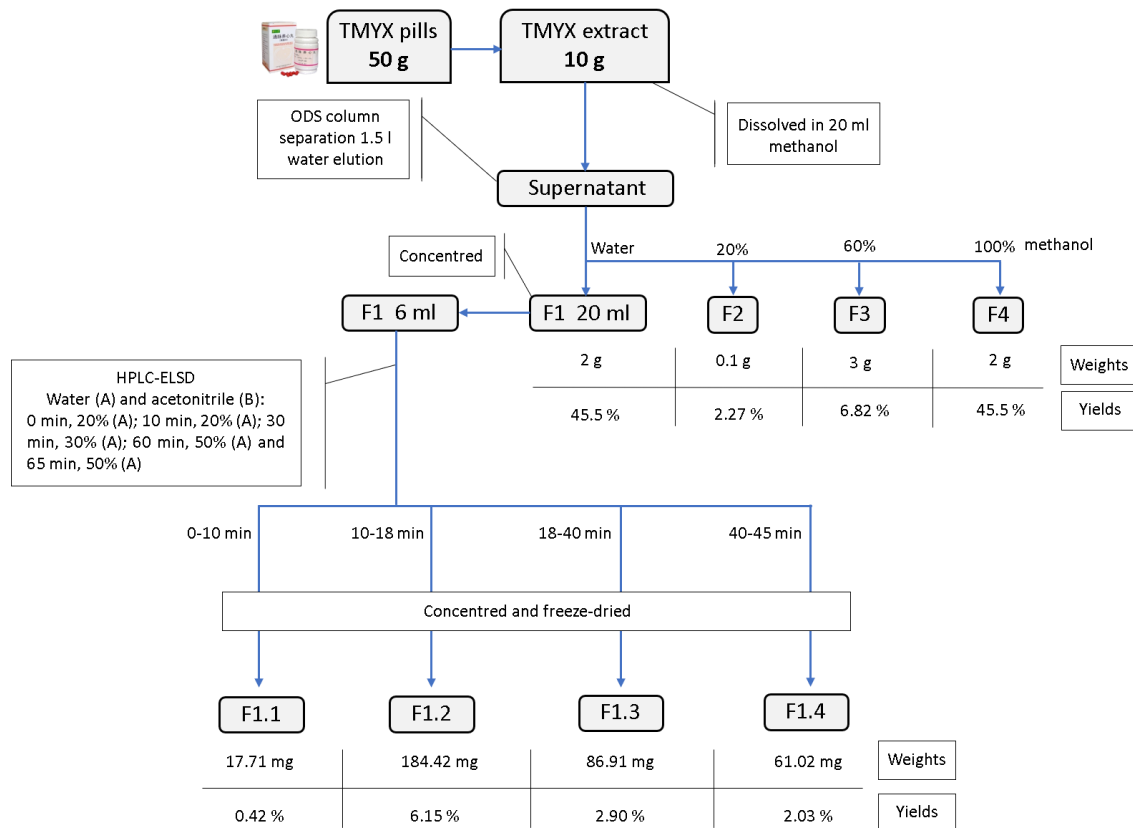


Figure 20. Flow chart of the isolation process of TMYX fractions (F1-4) and F1 sub-fractions (F1.1-1.4). Schematic representation of the flow chart used to isolate the 4 TMYX fractions (F1-4) and the 4 sub-fraction of F1 (F1.1-F1.4). The entire processes were performed by the team of professor Y. Wang at the Zhejiang University (Hangzhou, China).

Protocols and data analysis

All data were acquired through pClamp 10.7 software and subsequently analyzed using Clampfit, OriginPro 2016 and GraphPad Prism 7 software.

The protocols used in the experiments were designed on pClamp 10.7 software.

APs were recorded in current-clamp configuration as continuous traces for several hundreds of seconds at a sampling rate of 1-2 kHz. Raw traces records were digitally smoothed through a 10-point adjacent averaging smoothing procedure and the time derivative was calculated according to a second polynomial, 8-point smoothing differentiating routine.

For each AP cycle the following parameters were analyzed (**figure 21**):

- 1) Rate (Hz), calculated as the reciprocal of the cycle length from peak-to-peak dV/dt traces.
- 2) Maximum Diastolic Potential (MDP, mV), defined as the most negative voltage reached during AP repolarization.
- 3) Take-Off Potential (TOP, mV), defined as the voltage measured at the time when the voltage derivative (dV/dt) overtakes a given threshold, set to 0.5 mV/s (dashed red line in the bottom panel of **figure 21**); this value normally represents the level at which, regardless of rate, the voltage derivative dV/dt changes abruptly during the transition from phase 4 to phase 0 of the AP. The TOP value can also be described as the voltage at which the Ca^{2+} current responsible for AP depolarization takes off.
- 4) Slope of Early Diastolic Depolarization (EDD, mV/ms), for each cycle the diastolic depolarization is defined as the slope of the AP in the interval immediately following the MDP. Only the first half of the process is considered as EDD.
- 5) Action Potential Duration (APD, ms), defined as the time between a TOP and the following MDP, represents the time employed for a complete AP event.
- 6) Overshoot (OS, mV) defined as the most positive voltage reached during the AP depolarization.

All the parameters were analyzed using a customized software previously described in literature^{85,86}.

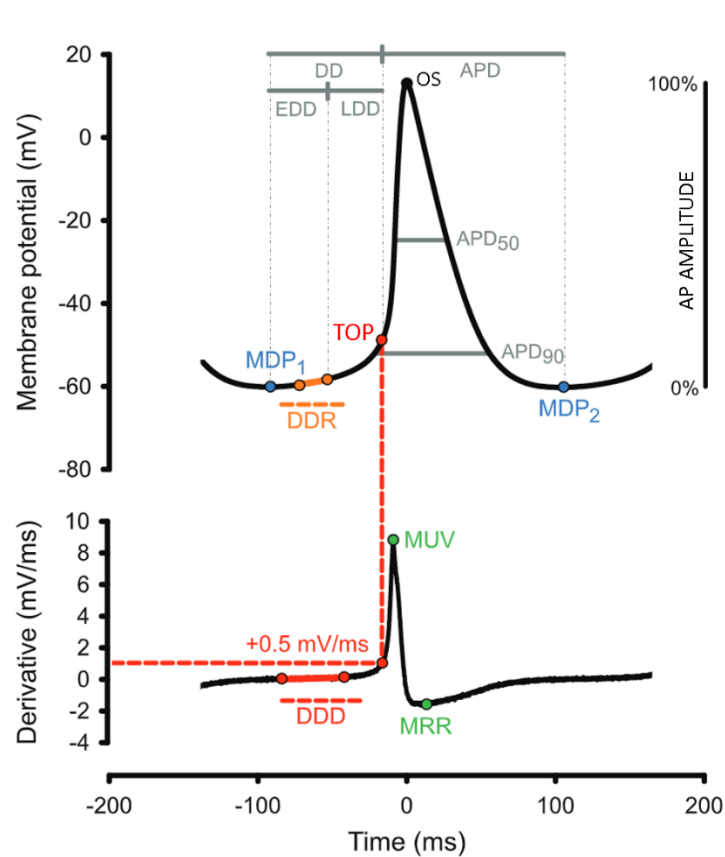


Figure 21. AP trace and corresponding time derivative dV/dt .

Representative AP trace (TOP) and the corresponding first time derivative dV/dt (BOTTOM). Here are indicated the maximum diastolic potential (MDP, blue), the take-off potential (TOP, red), the overshoot (OS, black), the early diastolic depolarization (EDD, grey line) and the action potential duration (APD, grey line). Additional parameters: DD=diastolic duration; LDD=late diastolic depolarization; DDR=diastolic depolarization rate; DDD=diastolic depolarization derivate; MUV=maximum upstroke velocity; MRR=maximum repolarization rate. (modified from Rickert & Proenza, 2017)

I_f current was recorded from single SAN myocytes (filter: 1 kHz) through a double step protocol which consisted of a 1.5s pulse to -65 mV (close to the $V_{1/2}$ of the activation curve) followed by a 0.5s voltage pulse to -125 mV, from a holding potential of -35 mV.

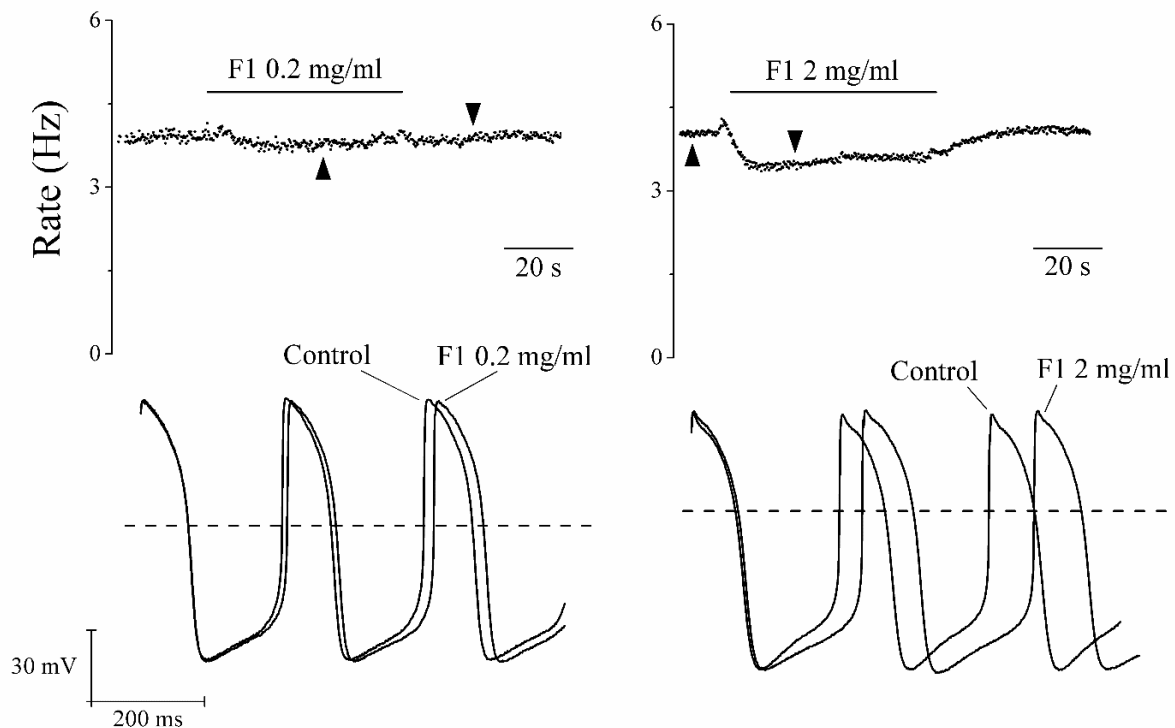
All data are presented as mean \pm SEM values. Computational and statistical analysis were carried out with OriginPro2016 and GraphPad Prism 7. Statistical tests and significance are indicated in the text.

RESULTS

TMYX fractions (F1-4) analysis

Since the clearest effect of TMYX on SAN myocytes is a reduction of the spontaneous firing rate, we set to identify which of the 4 fractions (F1-4) contains the molecule responsible for its bradycardic effect; to this aim each fraction was perfused individually on freshly isolated rabbit SAN myocytes. A series of patch-clamp experiments were then carried out to observe possible fraction-induced alterations in cell electrical properties that could resemble those of TMYX.

F1 was tested at two concentration (0.2 and 2 mg/ml); in both cases it was able to induce a reduction (vs control, Student's paired t-test, $p < 0.05$) of the spontaneous firing rate of pacemaker SAN cells, albeit with a minor potency than the total drug (**figure 22**).



F1 (mg/ml)	TMYX (mg/ml)	F1 REDUCTION (%)	TMYX REDUCTION (%)
0.2	0.44	-2.4	-4
2	4.4	-18.3	-40

Figure 22. Effects of F1 (0.2 and 2 mg/ml) perfusion on spontaneous rate of SAN myocytes.

Representative time-courses (TOP) and sample AP traces (BOTTOM) recorded in control condition and in presence of F1 (0.2 and 2 mg/ml). The table indicates F1 relative concentration in the total drug and compares the percentage rate reduction between the preparations.

The effect was fast and fully reversible since, after a brief wash-out period, the AP rate returned to the control state. This action resembled that of TMYX (albeit with a reduced potency, **figure 22, table**), thus an accurate analysis of the main AP parameters was carried out (**figure 23**). The results show that the rate reduction induced by F1 is associated with a decreased slope of the EDD phase (%: -4.66 ± 1.65 and -25.38 ± 3.02 ; F1 0.2 and 2 mg/ml, respectively) and a slight increase in APD but only at the higher concentration (%: 2.80 ± 1.13 , F1 2 mg/ml). MDP, TOP and OS were not influenced.

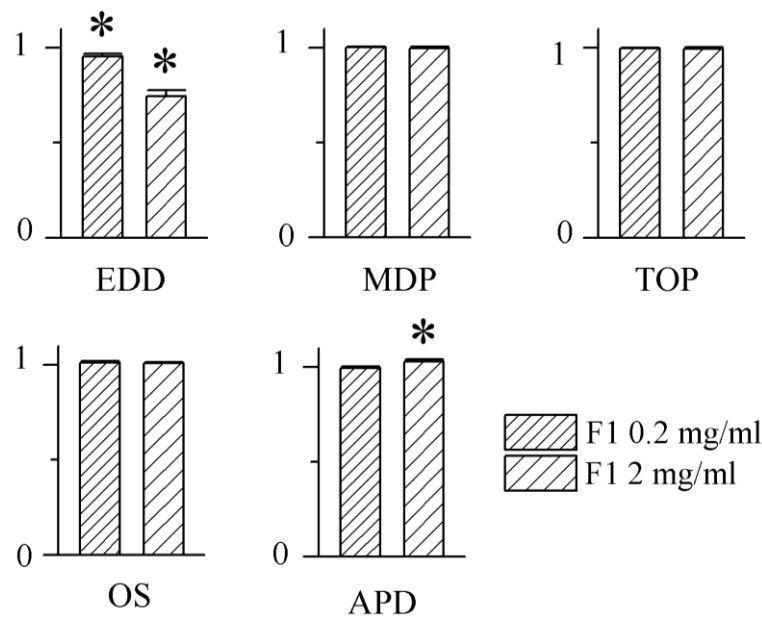


Figure 23. Effects of F1 (0.2 and 2 mg/ml) on the main AP parameters.

The bar graphs display the effects of two doses of F1 (0.2 and 2 mg/ml; n=11 and n=20, respectively) on the main AP parameters (EDD, MDP, TOP, OS and APD) normalized on the respective control values; $p < 0.05$ vs control, Student's paired t-test.

Finally, since the data indicated a specific action of F1 on the EDD slope, the possible involvement of the pacemaker current, the main regulator of this phase, was assessed: F1 (2 mg/ml) was perfused on single SAN myocytes and the I_f current was elicited through a double-step protocol (**figure 24 top**). As for TMYX, this compound was able to reduce the steady-state I_f current at -65mV while increasing it at -125mV (**figure 24 bottom**).

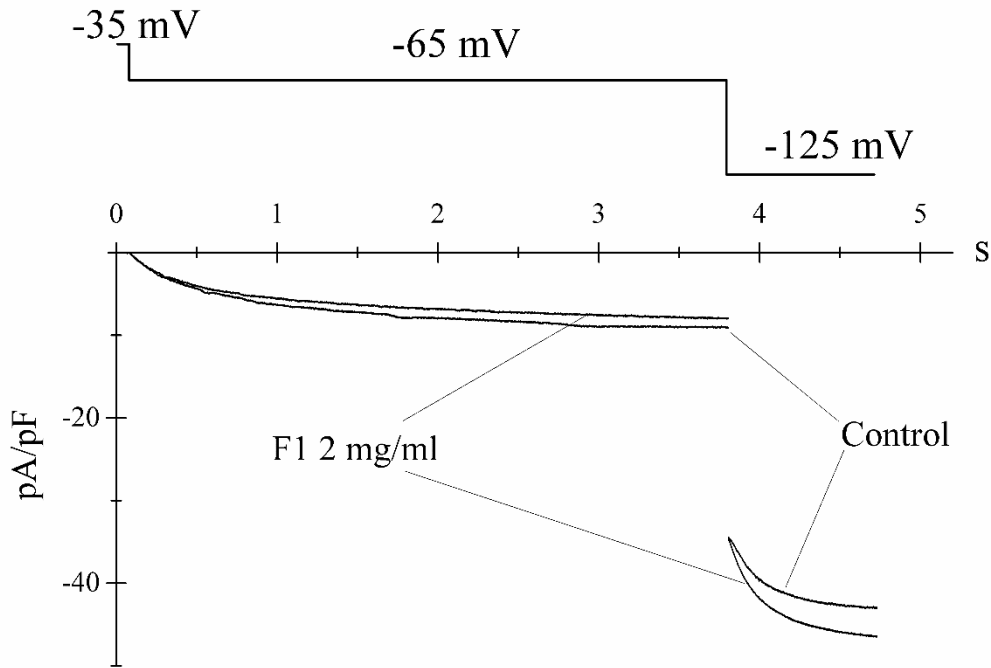
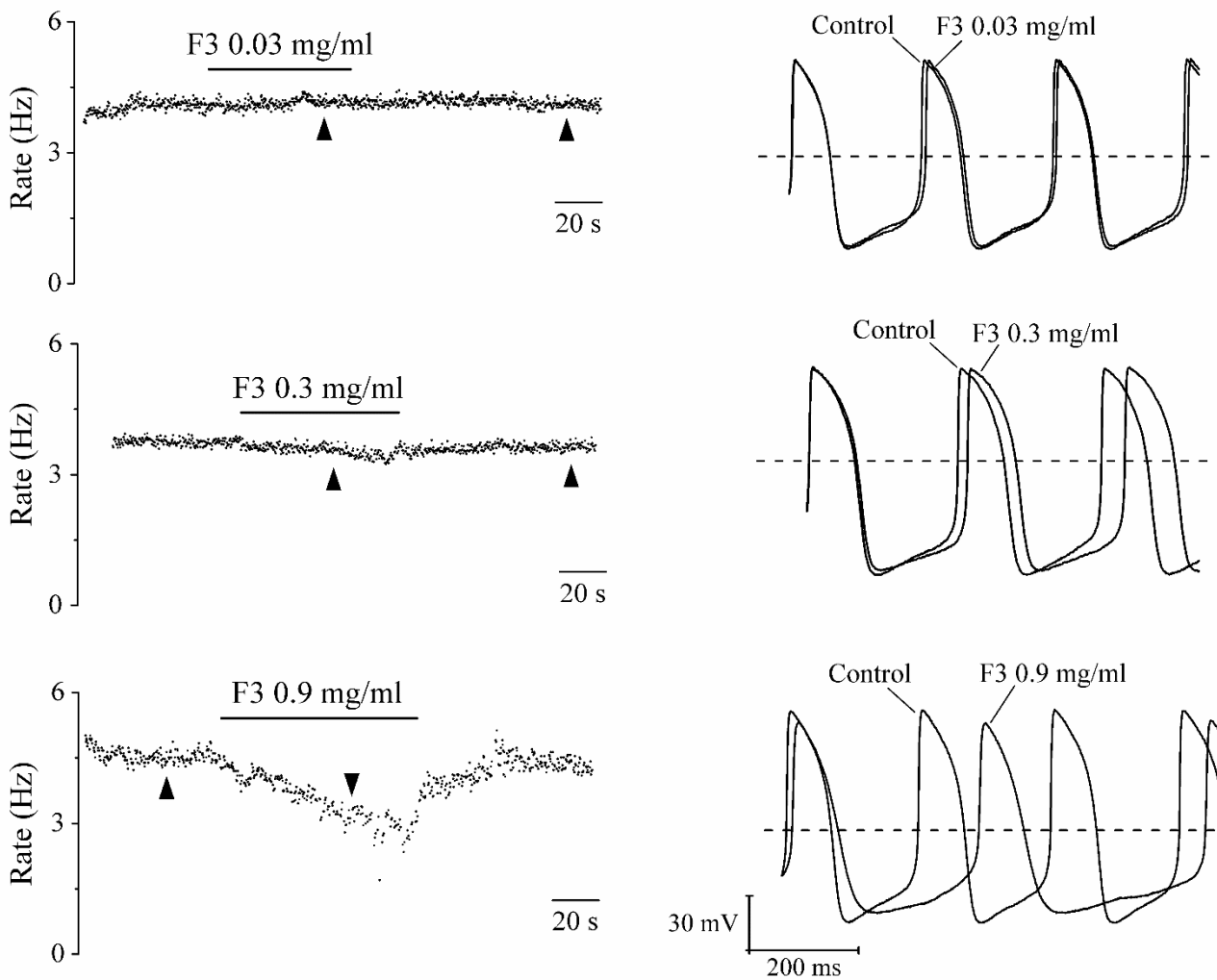


Figure 24. *F1 (2mg/ml) perfusion causes a double opposite effect on I_f current density at different voltages.* I_f current sample traces (BOTTOM) before and during perfusion of F1(2mg/ml). F1 is able to reduce the pacemaker I_f current at -65mV and increase it at -125mV, the same peculiar double opposite effect of the total drug. The two-step protocol used to record this current is displayed in the TOP part of the figure.

Unfortunately, due to the very low amount of F2 provided by the Chinese colleagues, an analysis of its effects on spontaneous rate and on the I_f current was impossible. Furthermore, given the promising result obtained for F1 and its sub-fractions, the analysis of this preparation appears not to be relevant for the aim of this work.

F3 underwent the same series of analysis carried out for F1 and was tested at three concentration (0.03, 0.3 and 0.9 mg/ml). When perfused on spontaneous beating SAN cells (**figure 25**), F3 induced a dose-dependent slowing of the AP rate (vs control, Student's paired t-test, $p < 0.05$) at all doses investigated. Its action was fully reversible, however, at 0.9 mg/ml, it clearly caused an alteration of the AP shape. As for F1, its potency was lower compared to that of TMYX at a comparative concentration.



F3 (mg/ml)	TMYX (mg/ml)	F3 REDUCTION (%)	TMYX REDUCTION (%)
0.03	0.44	-0.47	-4
0.3	4.4	-6.95	-40
0.9	13.2	-55.90	-85

Figure 25. Effects of F3 (0.03, 0.3 and 0.9 mg/ml) perfusion on spontaneous rate of SAN myocytes. Representative time-courses (LEFT) and sample AP traces (RIGHT) recorded in control condition and in presence of F3 (0.03, 0.3 and 0.9 mg/ml). The table indicates F3 relative concentration in the total drug and compares the percentage rate reduction between the preparations.

A complete analysis of the AP parameters was then performed (**figure 26**) and the results confirmed an non-specific action of F3 since all the factors investigated were altered both at the 0.3 and 0.9 mg/ml concentrations, suggesting that the activity of other channels involved in the AP

phases could be altered, too. However, no further investigations were performed regarding this issue.

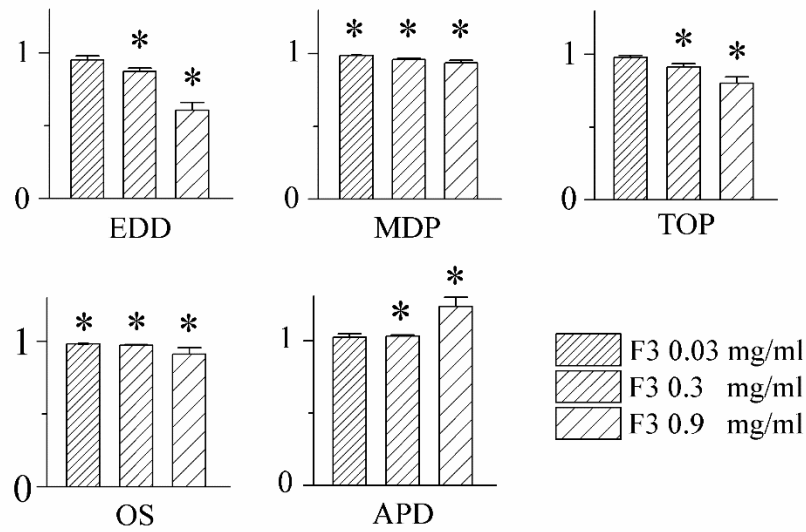


Figure 26. Effects of F3 (0.03, 0.3 and 0.9 mg/ml) on the main AP parameters. The bar graphs display the effects of three doses of F3 (0.03, 0.3 and 0.9 mg/ml; n=15, n=16 and n=14, respectively) on the main AP parameters (EDD, MDP, TOP, OS and APD) normalized on the respective control values; p<0.05 vs control, Student's Pair t-Test.

The last fraction of this set, F4, was also tested, and, when perfused on spontaneous beating SAN myocytes, it clearly induced a great rate reduction but its effect was maintained even after a 10 min wash-out period (figure 27), probably due to its highly lipophilic nature. No further investigations were thus performed.

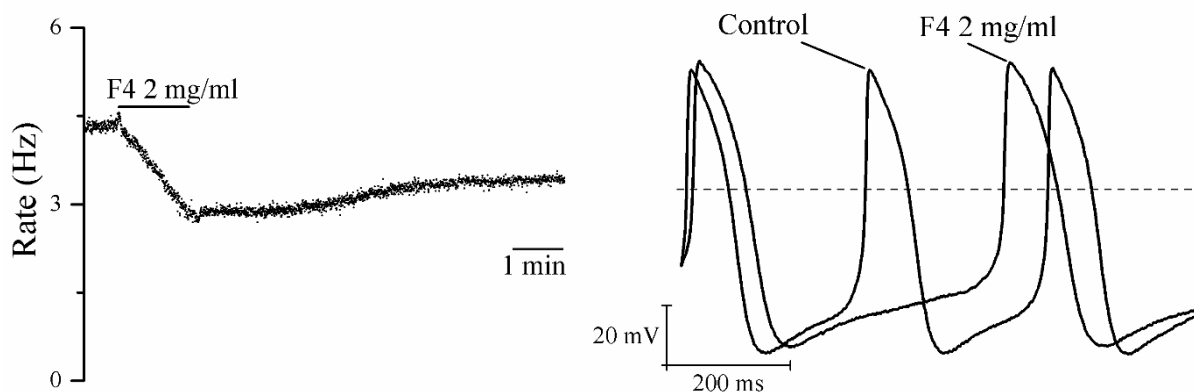


Figure 27. Effects of F4 (2 mg/ml) perfusion on the spontaneous rate of SAN myocytes. Representative time-course (LEFT) and sample AP traces (RIGHT) recorded before and during F4 (2 mg/ml) perfusion. Even after several minutes of wash-out, cell rate is not able to return to the pre-drug condition, moreover the AP shape appears to be altered, too.

The results obtained so far suggest that the molecule of TMYX responsible for the observed bradycardia is located in the F1 fraction, since this is the only preparation able to reduce the spontaneous beating of SAN cells in a dose-dependent and reversible way acting specifically on the EDD slope; furthermore, it mimics the double effect of TMYX on the pacemaker I_f current.

F1 sub-fractions (F1.1-1.4) analysis

To further narrow down the number of molecules to examine, F1 was subsequently divided into 4 sub-fractions (F1.1-1.4).

As for the previous compounds, the first analysis consisted in the evaluation of the effects induced by these preparations on the spontaneous beating of SAN myocytes (**figure 28**).

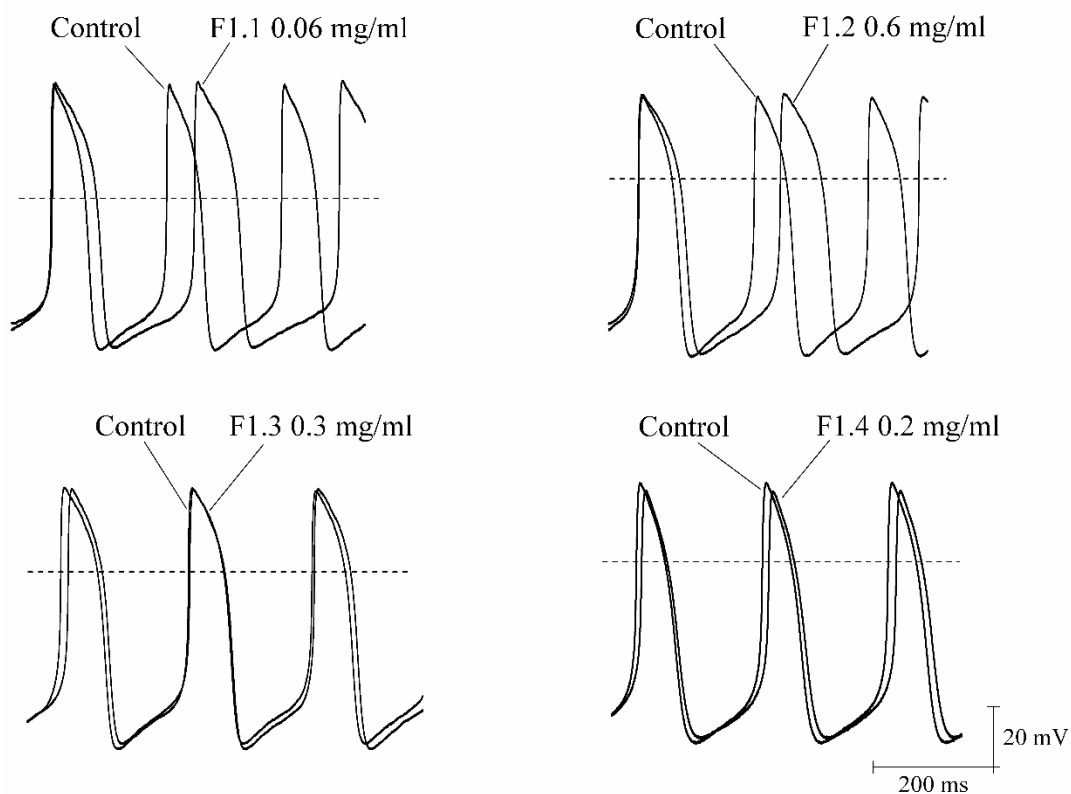


Figure 28. *Effects of F1 sub-fractions (F1.1-1.4) perfusion on spontaneous beating SAN myocytes.* Sample AP traces recorded in control condition and in presence of F1 subfractions (F1.1 0.06 mg/ml, F1.2 0.6 mg/ml, F1.3 0.3 mg/ml and F1.4 0.2 mg/ml – the concentrations of the drugs were calculated in order to reflect their relative presence in F1).

These data clearly demonstrate that only F1.1 and F1.2 are able to induce a significant reduction of the AP rate (%: -20.48 ± 2.23 and -10.58 ± 3.37 ; F1.1 and F1.2), while F1.3 and F1.4 do not

cause any relevant alteration. A further confirmation of these results came from the analysis of the AP parameters (**figure 29**).

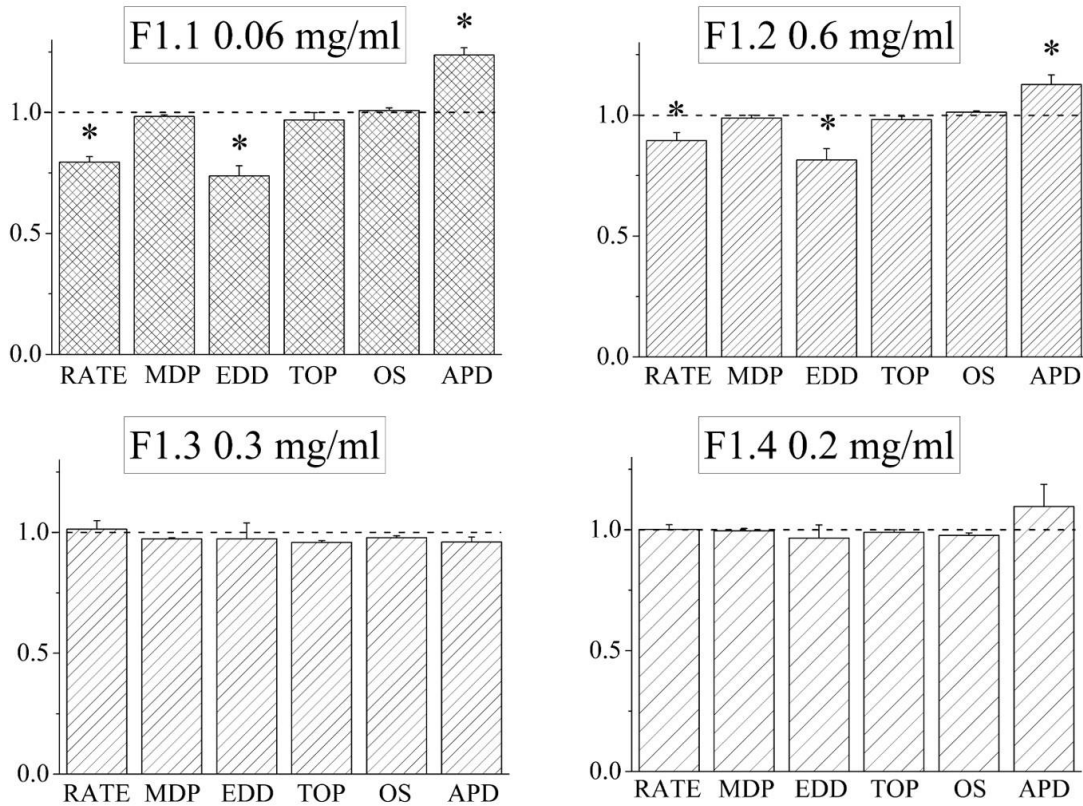


Figure 29. Effects of F1 sub-fractions (F1.1-1.4) on spontaneous rate and the main AP parameters. The bar graphs display the effects of F1 sub-fractions (F1.1, 0.06 mg/ml; F1.2, 0.6 mg/ml; F1.3, 0.3 mg/ml; F1.4, 0.2 mg/ml; n=7) on the spontaneous beating rate and the main AP parameters (EDD, MDP, TOP, OS and APD) normalized on the respective control values; p<0.05 vs control, Student's pair t-test.

For both F1.1 and F1.2, rate slowing was associated with a reduced EDD slope (%: -26.21 ± 4.20 and -18.54 ± 4.67 ; F1.1 and F1.2, respectively) and an increased APD (%: 23.80 ± 3.00 and 12.70 ± 4.02 ; F1.1 and F1.2, respectively). Although the increased APD appears to be quite remarkable, it has to be considered that this is in part due to the reduced AP frequency as a physiological adaptation. As expected, F1.3 and F1.4 did not induced any type of alteration in the AP shape.

Finally, possible effects on the I_f current were observed during the perfusion of all the 4 sub-fractions (**figure 30**). According to the previous results, F1.1 and F1.2 generated the typical double effect of TMYX on the current while F1.3 and F1.4 did not cause any modification.

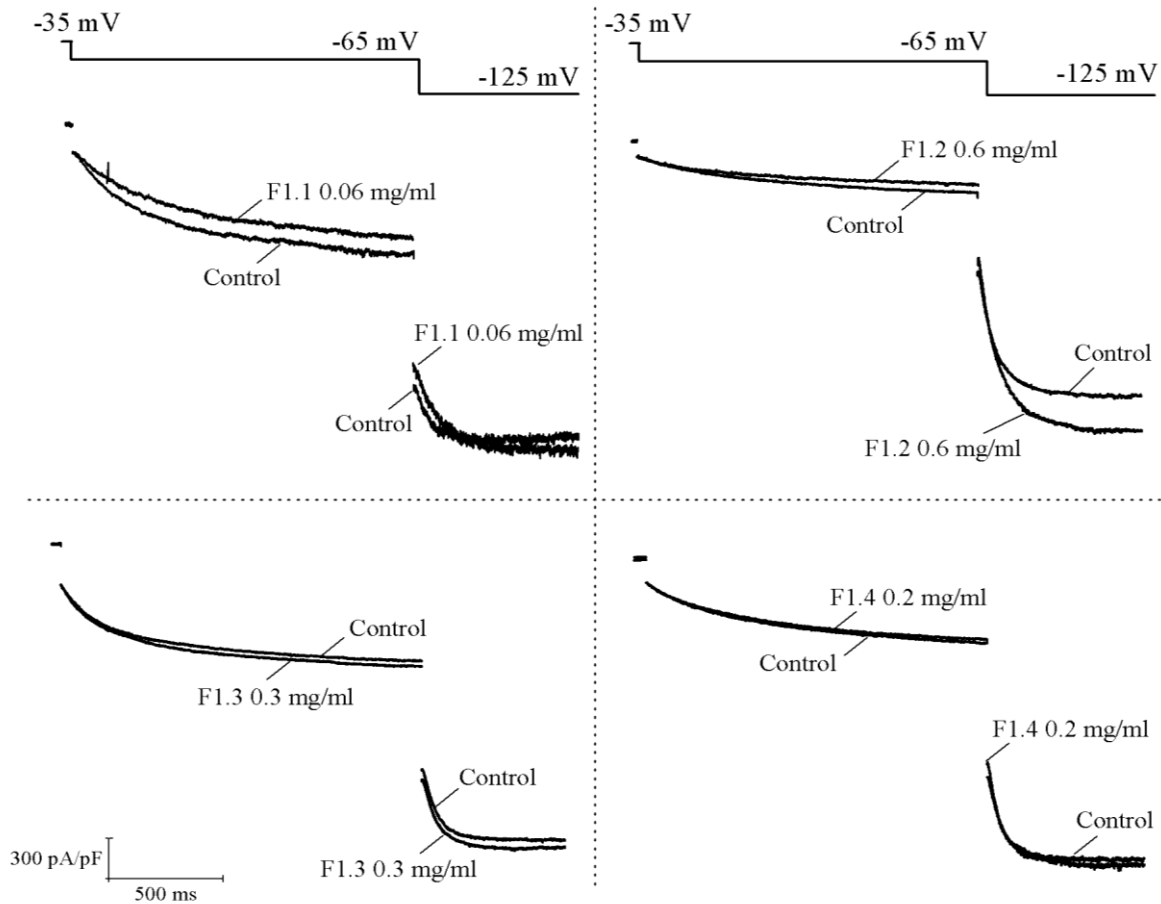


Figure 30. Effects of F1 sub-fractions (F1.1-1.4) perfusion on the I_f current at different voltages.

I_f current sample traces recorded before and during perfusion of F1.1 (0.06 mg/ml), F1.2 (0.6 mg/ml), F1.3 (0.3 mg/ml) and F1.4 (0.2 mg/ml). While F1.1 and F1.2 are able to reduce the pacemaker I_f current at -65mV and increase it at -125mV, mimicking TMYX, F1.3 (0.3 mg/ml) and F1.4 (0.2 mg/ml) do not cause any relevant alteration. The two-step protocol used to record this current is displayed in the top part of the figure.

These data suggest that the molecule responsible for the bradycardic effect of TMYX is contained in both F1.1 and F1.2.

Preliminary investigations on uridine

Preliminary biochemical studies regarding the composition of these two sub-fractions, performed by our Chinese partners, highlighted the presence of a putative shared molecule between F1.1 and F1.2 preparations. Indeed, HPLC analysis revealed a remarkable presence of uridine, or one of its derivatives, in both the compounds. Based on this evidence, we performed some preliminary patch-clamp experiments to evaluate whether this molecule was able to induce elec-

trical alterations in rabbit SAN myocytes. Notably, 1 μM uridine (**figure 31D**) appears to generate a minor increase (+3.45%) in the spontaneous AP rate (**figure 31A-B**). However, when tested on the I_f current (**figure 31C**), a decrease at -65mV was observed.

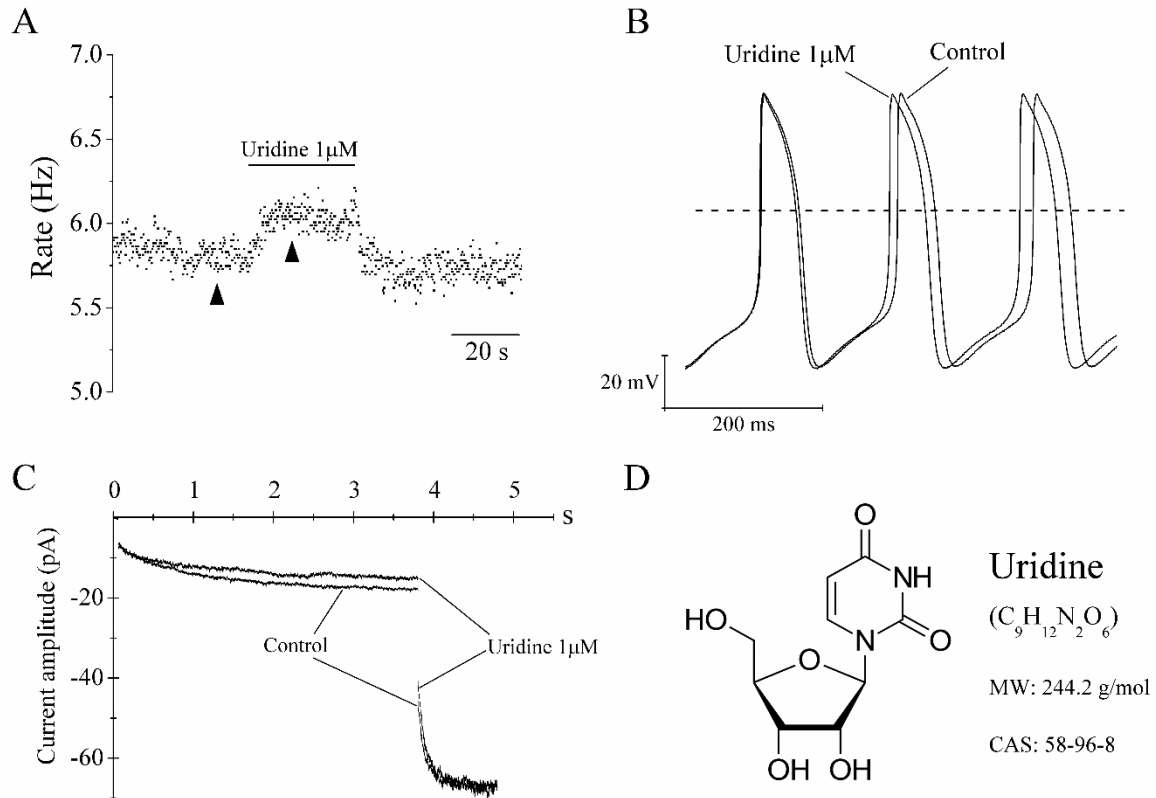


Figure 31. Effects of uridine (1 μM) perfusion on spontaneous AP rate and on the I_f current.

Time course (A), representative AP traces (B) and sample I_f current traces (C) recorded in control conditions and during uridine (1 μM) perfusion. Although the administration of the drug on SAN cells induced an increase in the spontaneous rate, I_f current appears to be reduced at physiological voltages (-65mV). (D) Molecular structure of Uridine, its molecular formula, molecular weight and CAS number.

These results are clearly contrasting and preliminary, therefore further studies are required in order to confirm or exclude any electrical regulatory action of this molecule.

DISCUSSION

In recent years, several robust studies have demonstrated the safe use and beneficial effects of TCM drugs on different pathologies including cancer and cardiovascular diseases^{78,87-89}. Interestingly, and in line with western pharmacology, cardiovascular TCM drugs often target ion channels; for example, the antiarrhythmic agent Wenxin Keli (see *introduction, Traditional Chinese Medicine* section) modulates several cardiac ion channels according to a mechanism of potential relevance in the treatment of atrial fibrillation^{71,77}.

The data presented here highlight the promising impact that Tongmai Yangxin (TMYX), a herbal mixture used in TCM, could have in future years, especially for what concerns the treatment of patients affected by arrhythmias and other cardiovascular diseases which will benefit from a reduced heart rate (angina, coronary artery disease).

With the aim of identify the bio-active molecule responsible for the bradycardic effect of TMYX, the drug was separated the in 4 fractions (F1-4) according to the solubility of the molecules contained. Alterations in the electrical activity of rabbit SAN myocytes were then evaluated by patch-clamp experiment following the perfusion of the 4 preparations. As can be inferred from the results, only F1 was able to reproduce the effects of TMYX both on the spontaneous firing rate (**figure 22**), by means of a specific action on the slope of the EDD phase (**figure 23**) and on the pacemaker I_f current (**figure 24**). Since the molecules contained in this preparation has the highest hydrophilic profile of all the fractions, it is a highly possible for the target compound to display at least a partial water-solubility. Still, at this level of investigation, it is quite difficult to speculate on the characteristics of this molecule.

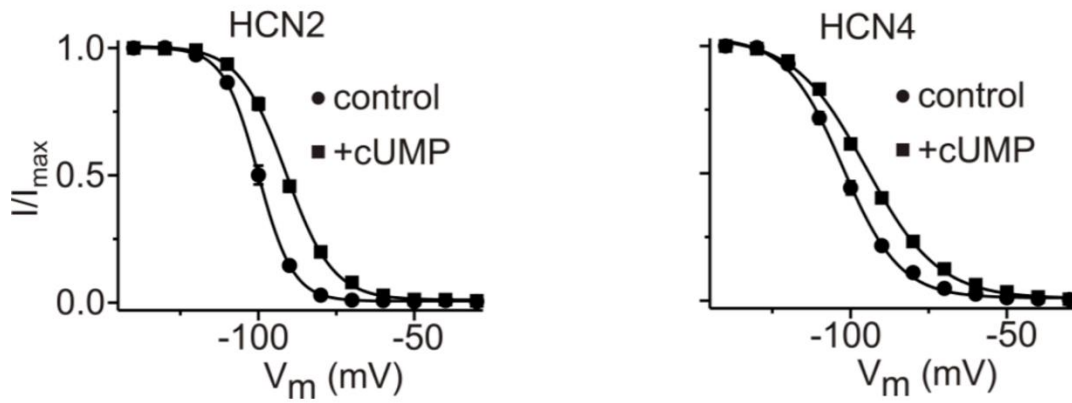
To shed more light on the nature of this bio-active compound, F1 was further separated in 4 sub-fractions (F1.1-1.4) and the same set of electrophysiological analysis was employed to evaluate their effects on rabbit SAN myocytes. As depicted in **figure 28** and **29** both F1.1 and F1.2 show a moderate reduction ability on the spontaneous AP firing with a specific action on EDD phase, the same mechanism observed in TMYX and F1. Furthermore, their effects on the I_f current (**figure 30**) clearly resemble the peculiar dual and opposite effects of the total drug (decreased current density at -65 mV and increased at -125 mV). The presence of the target molecule in two consecutive fractions (F1.1 and F1.2) is likely related to its small dimensions. Still, the nature of this compound is unknown; a mass spectrometry analysis on F1.1 and F1.2 shared compounds will probably solve this enigma.

Nevertheless, preliminary evaluation of HPLC data indicate the nucleoside uridine (or one of its derivatives) as an accountable target. Uridine is a glycosylated pyrimidine-analog containing uracil attached to a ribose ring (or more specifically a ribofuranose) via a β -N1-glycosidic bond. This molecule is involved in several physiological functions; specifically, it is an essential component of RNA synthesis, it plays a critical role in the production of glycogen and contributes in the generation of bio-membranes⁹⁰.

As shown in **figure 31**, perfusion of uridine 1 μ M on spontaneous beating SAN cells induced a small and reversible rise of the AP firing rate, but decreased the I_f current density at physiological voltages. These results are obviously contradictory, however, the augmented spontaneous activity could be the result of a concurrent effect on other channels/proteins that, at the given concentration (1 μ M), is able to override the bradycardic action induced by the decreased I_f current. It is clear that additional analysis are requested to fully understand this phenomenon.

In addition, it should be taken into account that also a cyclic nucleotide form of uridine (cyclic-uridine monophosphate, or cUMP) has also been observed. Given that TMYX mechanism of action is based on the competitive antagonism with cAMP for the binding to the CNBD of f-channels, the properties of this molecule should also be investigated. Furthermore, cUMP appears to be a partial low-potency activator of HCN channel isoforms 2 and 4, but not of isoforms 1 and 3⁹ (**figure 32**). However, the model employed for this experiments was HEK-293 which allows to observe the interaction between cUMP and the channel but loses the cardiac intracellular regulation typical of SAN myocytes.

Albeit the connection between uridine and TMYX is yet to be confirmed, this molecule, and its cyclic monophosphate form (cUMP), displays interesting features that should be explored in detail in order to fully characterize their possible electrical modulatory activity.



	HCN2		HCN4	
	-cUMP	+cUMP	-cUMP	+cUMP
$V_{1/2}$ (mV)	-100	-89.6	-102	-95
τ_{act} (ms)	5.49	7.13	9.08	11.5

Figure 32. Effects of cUMP perfusion on HCN1-2 channels properties.

Voltage-dependent activation curves recorded in control conditions and during cUMP 1mM perfusion (n=11-16). Full lines indicate the Boltzmann fitting of data-points. In the table are reported the mean $V_{1/2}$ and τ_{act} values before and during cUMP perfusion (from Zong et al., 2012).

PACEMAKER MODULATION IN AGING

INTRODUCTION

Cardiovascular diseases (CVDs) are the main cause of mortality in industrialized countries and their incidence increases with age. According to the World Health Organization, 17.9 million people died from CVDs in 2016, representing 31% of all global deaths. It has been estimated that by the beginning of the next decade, approximately 20% of the population will be aged 65 or older and CVDs will result in 40% of all deaths^{10,11}. Furthermore, the social and economic cost associated with these disorders will obviously get worse with time; in particular the financial expenses will triple by the beginning of the next decade^{91,92}. To deal with this burden, a major aim of the scientific community is to unravel the mechanisms underlying the relation between aging and the etiology of cardiac pathologies so that newer and less-invasive therapeutic strategies could be explored.

It is well documented both in humans and mice that during aging, basal heart rate (BHR, i.e. resting heart rate) remains stable^{93,94} while the intrinsic heart rate (IHR, i.e. heart rate deprived of ANS modulation) declines significantly⁹⁵⁻⁹⁷ (**figure 33**).

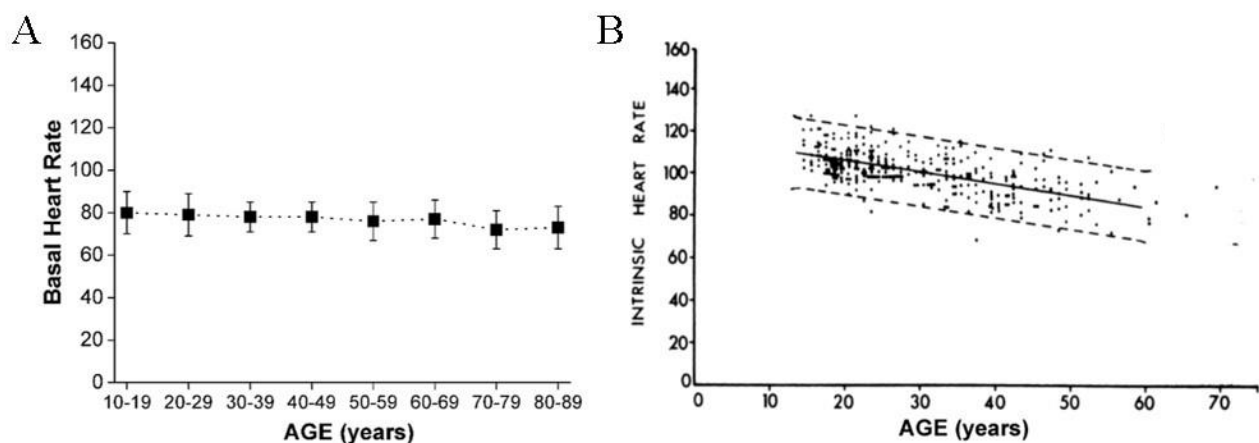


Figure 33. BHR is preserved in advanced age while IHR declines.

(A) Mean BHRs \pm SD acquired from patients (n=260) of different ages and sex (redrawn from Umetani et al., 1998). (B) IHRs in healthy male patients recorded after administration of Propranolol (0.2 mg/kg) and Atropine Sulphate (0.04 mg/kg). The same trend was observed in females (modified from Jose and Collison, 1970).

Since the IHR is unrelated to autonomic control, the causes of its decrease with aging should rely on structural and molecular changes likely occurring within the SAN. From an histological point of view, the aged SAN is characterized by tissue fibrosis, fatty infiltration and cellular senescence^{98,99}. This condition predisposes elderly people to higher vulnerability to both bradyarrhythmias (e.g., sinus arrest) and tachyarrhythmias (e.g., atrial fibrillation, ventricular tachycardia), causing substantial morbidity and mortality¹⁰⁰⁻¹⁰³. Notably, Larson et al.⁹⁷ found remarkable differences in the AP shape of different age mice underlying a modification in ionic channel activity with aging, specifically regarding the pacemaker and the T-type Ca^{2+} currents. Susceptibility to arrhythmogenesis is further enhanced by age-dependent modifications of both the electrical profile of cardiac cells (i.e. ion currents balance), and of cardiac ANS function¹⁰¹⁻¹⁰³. For example, basal plasma norepinephrine levels increase with age^{104,105}, suggesting that sympathetic nervous activity may be elevated in elderly people and this may therefore affect the electrical stability of both atria and ventricles^{103,106,107}. Moreover, an age-related impairment in cardiac vagal modulation has been documented in studies reporting a decline in the vagal component of HRV and diminished HR responses to blockade of muscarinic acetylcholine receptors with advancing age¹⁰⁸⁻¹¹².

Animal models, specifically mice, could be useful to shed light on the relation between aging of the cardiac ANS, decline in vagally-mediated HRV and proarrhythmic electrical remodeling of the heart.

AIMS

By the beginning of the next decade the number of elderly people will substantially increase and the high mortality related to cardiovascular diseases will represent a serious social issue. Thus, the scientific interest concerning the pathophysiological mechanisms underlying cardiac aging is rising year after year.

Data already reported in the scientific literature highlight the occurrence of an age-related decline in intrinsic heart rate (IHR) but a preservation of basal heart rate (BHR), a phenomenon that is still not fully understood. The most solid hypothesis indicates an unbalance of the autonomic nervous system (ANS) influence towards an increased role of the sympathetic activity.

The aim of this study is to assess age-related changes in cardiac autonomic modulation and heart rate variability (HRV) and their association with spontaneous and pharmacologically-induced vulnerability to cardiac arrhythmias, to verify the translational relevance of mouse models for further in depth evaluation of the link between autonomic changes and increased arrhythmic risk with advancing age.

MATERIALS AND METHODS

Animals

C57BL/6J mice (JAX™ from Charles River Europe) of two different ages (4- and 19-month-old) were individually housed, kept in rooms with controlled temperature ($22\pm 2^\circ\text{C}$) and humidity ($60\pm 10\%$), and maintained in a 12/12 hr light/dark cycle (light on from 7:00 to 19:00 h), with food and water ad libitum.

All procedures performed were in accordance with the European directive 2010/63/UE and approved by the Italian legislation on animal experimentation (D.L. 04/04/2014, n. 26). All efforts were made to reduce sample size and minimize animal suffering.

Transmitter implantation

Mice were anesthetized using inhaled isoflurane (Isoflurane-VET, Merial). Anesthesia was induced by spontaneous breathing of 5% isoflurane in 100% oxygen at a flow rate of 1 L/min and then maintained at 1.5-3% isoflurane in 100% oxygen at a flow rate of 1 L/min; all animals received analgesic (Rymadil, Pfizer, 5 mg/kg) and antibiotic (Baytril, Bayer, 5.8 mg/kg) treatment immediately prior to transmitter implantation. Mice were then implanted with radiotelemetric transmitters (TA10ETA-F20, Data Sciences Int.) for recordings of ECG (sampling frequency: 2000 Hz), and locomotor activity (LOC, expressed as counts/minute) signals. The transmitter was placed in the abdominal cavity: one electrode was fixed to the dorsal surface of the xiphoid process and another one was placed in the anterior mediastinum close to the right atrium, according to a previously described procedure¹¹³. This electrode location guarantees high-quality ECG recordings, even during vigorous somatomotor activity. Animals were given food and water post-surgery and were housed individually. Rymadil and Baytril were given to the animals for 5 consecutive days after surgery. Before the beginning of the experimental recordings, mice were allowed two weeks to recover and re-establish normal daily rhythms of heart rate and LOC.

Pharmacological ANS modulation

At the end of the daily recordings, mice were injected intraperitoneally on different days, following a rotational design, with: (i) 1 ml/kg saline solution (0.9% NaCl; control condition); (ii) 0.1

mg/kg methylscopolamine (muscarinic receptor antagonist); (iii) 1 mg/kg atenolol (β -adrenergic receptor antagonist); (iv) methylscopolamine+atenolol (at the same above-indicated doses; for both vagal and sympathetic blockade). Each injection was separated by at least a 2-day wash-out period and the injection volume was always the same (100 μ l). Drug doses were selected on the base of previous studies^{114,115}.

After pharmacological autonomic blockades, mice were injected intraperitoneally with isoprenaline (non-selective β adrenergic agonist, at a dose of 0.2 mg/kg for mimicking potent sympathetic stimulation¹¹⁶).

ECG recordings were performed 1 hr prior (baseline control condition) and 2 hrs after the injection procedure.

Data recording and analysis

After recovery from surgery, ECG and LOC signals were recorded for 120 s every 30 min for six consecutive days, with the animals left undisturbed in their home cages. ECG and LOC signals were picked up by platform receivers (RPC-1, Data Sciences Int.) and acquired via Dataquest A.R.T.TM Gold 4.3 acquisition system (Data Sciences Int.).

Initially, each raw ECG signal was visually inspected to ensure that all R-waves were correctly detected. Those parts of ECG recordings which exhibited artifacts were discarded without substitution and excluded from further analysis. Heart rates (bpm) and time- and frequency-domain parameters of HRV were quantified using ChartPro 5.0 software (ADInstruments), following the guidelines suggested by Thireau and colleagues¹¹⁷ for the assessment of HRV parameters in mice. Time-domain measures included the standard deviation of the time between normal-to-normal beats (SDNN) and the root mean squared of successive beat-to-beat interval differences (RMSSD)²⁵. For spectral (frequency-domain) analysis of HRV, a power spectrum was obtained with a fast Fourier transform-based method (Welch's periodogram: 256 points, 50% overlap, and Hamming window). The following parameters were taken into account: the total power of the spectrum (TP, ms²), the power (ms²) of the low frequency band (LF, 0.15–1.5 Hz), the power (ms²) of the high frequency band (HF; 1.5–5.0 Hz), and the low frequency/high frequency ratio (LF/HF).

Separate estimates of heart rates, HRV and LOC were initially generated for each 2-min recording period and subsequently averaged as mean values of the 12 h-light and 12 h-dark phase of each recording day. These parameters were then further averaged to obtain light phase and dark phase means of the 6 recording days. Subsequently, to test for differences between the two groups

of mice, a series of two-way ANOVAs for repeated measures were applied on heart rates and HRV data, with “group” as the between-subject factor (two levels: 4- and 19-month-old mice) and “phase” as the within-subject factor (two levels: light and dark phases). Follow-up post hoc analyses were conducted using Fisher's LSD.

Each recording period was split in 2-min epochs (0–2 min, 2–4, etc.). For each epoch, separate estimates of heart rates and HRV were generated. Initially, to test the effects of pharmacological autonomic manipulations on heart rate values within each group, Δ heart rate values were calculated as the differences between each 2-min post-injection period and the respective mean baseline value, and then averaged for the 60-min period corresponding to the second hour that followed each injection (min 60-120; i.e., when animals had completely re-established baseline heart rates and HRV following stress associated with handling and injection, as shown in the saline condition). For each group, delta heart rate values were analyzed by means of one-way ANOVAs for repeated measures, with ‘autonomic manipulation’ as the within subject factor (4 levels: control condition, vagal blockade, sympathetic blockade, double blockade). Follow-up post hoc analyses were conducted using Fisher's LSD. Subsequently, to test for differences between the two groups of mice in heart rate and HRV parameters during each pharmacological autonomic manipulation, a series of two-way ANOVAs for repeated measures were applied, with “group” as the between subject factor (two levels: 4- and 19-month-old mice) and “condition” as the within-subject factor (two levels: baseline and post-injection (min 60-120)).

Follow-up analyses were conducted using Student's t-tests with a Fisher's correction for multiple comparisons.

Incidence of cardiac arrhythmias

Lastly, the occurrence of spontaneous and pharmacologically (isoprenaline)-induced cardiac arrhythmias was determined and quantified as described in previous works^{118,119}. Occurrence of sinus pauses, atrioventricular blocks, and supraventricular (SV) and ventricular (V) ectopic beats and the total number of arrhythmic events (reported as number of events per length (hrs) of analyzed ECG recording) were identified and analyzed during daily undisturbed conditions and following pharmacological sympathetic stimulation with isoprenaline. Age-related changes in arrhythmia vulnerability were assessed by means of unpaired Student's t-tests.

Data in figures and tables are presented as means \pm SEM. Statistical analyses were performed using OriginPro2016 and SPSS 24 software package. Statistical significance was set at $p < 0.05$.

RESULTS

Circadian HR and HRV rhythms

The presence of a circadian oscillation of the heart rate was assessed by collecting 2 minutes-long ECG traces every 30 minutes for 6 consecutive days. Mean heart rate values measured during light and dark phases of the daily cycle are shown for each mouse in **figure 34A, left**, while collective mean data are shown on the **right**.

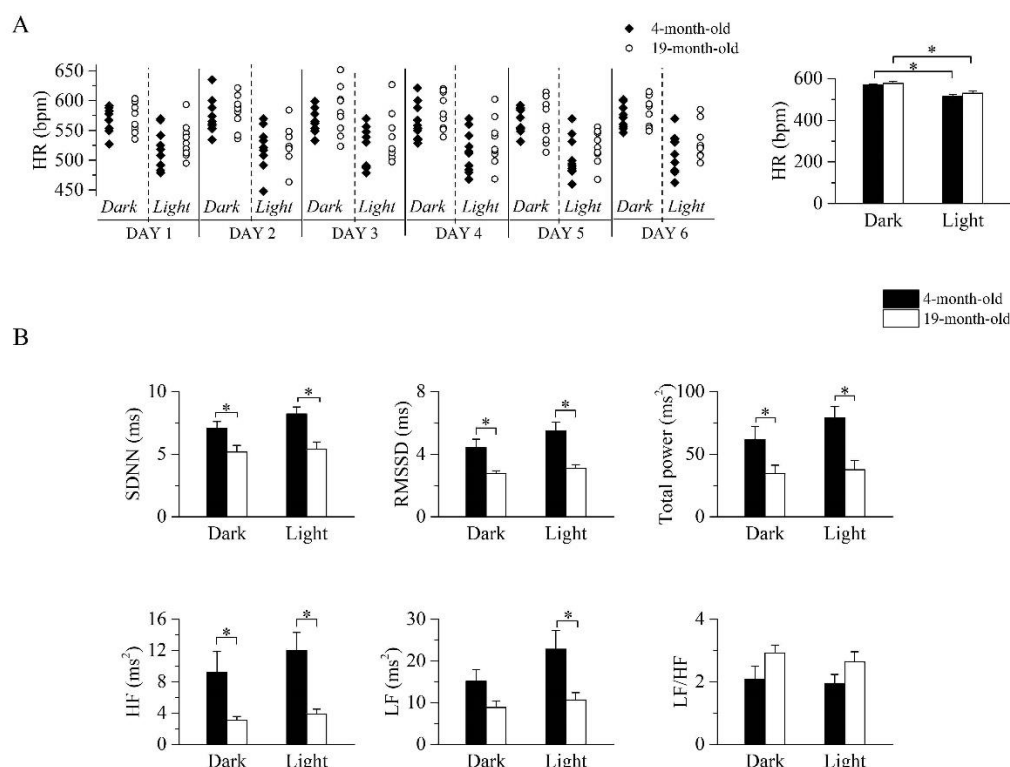


Figure 34. Long-term evaluation of heart rate (HR) and HRV in 4- and 19-month-old freely-moving mice. (A) Time course (left) and mean values (right) of the heart rates (HR) recorded during the 12-hr light and 12-hr dark phases of 6 consecutive days in adult ($n=10$, filled squares) and aged ($n=9$, empty circles) freely-moving mice. (B) Mean HRV parameters evaluated from ECG traces recorded from adult and aged (same meaning of color) mice during the daily cycle (dark and light phases). SDNN=standard deviation of beat-to-beat intervals; RMSSD=root mean square of successive beat-to-beat interval differences; LF=low frequency; HF=high frequency. $p<0.05$, two-way ANOVA with repeated measures followed by Fisher's LSD post-hoc test (from Piantoni et al, 2020 - submitted).

As expected, the heart rates during the dark/active phase of the daily cycle were significantly higher than those during the light/inactive phase for each age group^{120,121} (dark: 567.8 ± 6.54 bpm, 576.12 ± 9.85 bpm, 4- and 19-month-old, respectively; light: 514.7 ± 9.54 bpm, 529.34 ± 10.56 bpm, 4- and 19-month-old, respectively); comparison between age-groups in the light and dark

conditions did not reveal significant differences. Also, no difference in the locomotor activity was detected between the groups (data not shown). HRV indexes, extracted from the same ECG recordings, are plotted in **figure 34B**. The 19-month-old group showed significantly lower values of SDNN, RMSSD, total power, and HF power during both phases of daily cycle, while LF power was reduced only during the light phase. No significant differences were instead observed in the LF/HF ratio.

Age-related differences in ANS modulation of the heart rate

In order to investigate the influences of the ANS on heart rate and dissect the relative contribution of the sympatho-vagal balance in the two age conditions, we evaluated the heart rate responses to selective pharmacological blockades of the parasympathetic and sympathetic systems (**figure 35**) by i.p. injection of methylscopolamine and/or atenolol. Since heart rate and HRV indexes are greatly influenced by the experimental handling of the mouse, animals were first injected with a saline solution. The complete recovery (i.e. basal level, defined as the mean value measured during the hour preceding the treatments) was attained 1 hr after the injection so all the analyses were then carried on the second hour after the injection. The time-courses of heart rate changes (Δ HR) following each autonomic manipulation are shown overlapped separately for the two age groups (**figure 35, left**). Mean Δ HR, calculated in the second hour after the injection, are presented in the right panels of **figure 35** and in the table below.

Within-group statistics yielded a significant effect of autonomic manipulation both in 4-month-old and 19-month-old mice. Specifically, post-hoc analysis revealed that in 4-month-old mice vagal blockade with methylscopolamine provoked a significant increase in heart rate (vs saline), whereas sympathetic blockade with atenolol provoked a significant decrease in heart rate (vs saline). No significant changes in heart rate were observed in 4-month-old mice after double autonomic blockade (methylscopolamine+atenolol) compared with the control condition. In the 19-month-old group a significant decrease in heart rate was observed during sympathetic blockade, while an increase, albeit not significant, was observed during parasympathetic deprivation. Quite interestingly, in the older group the double autonomic blockade caused a significant decrease of heart rate, thus revealing a substantial difference between the intrinsic and basal rate.

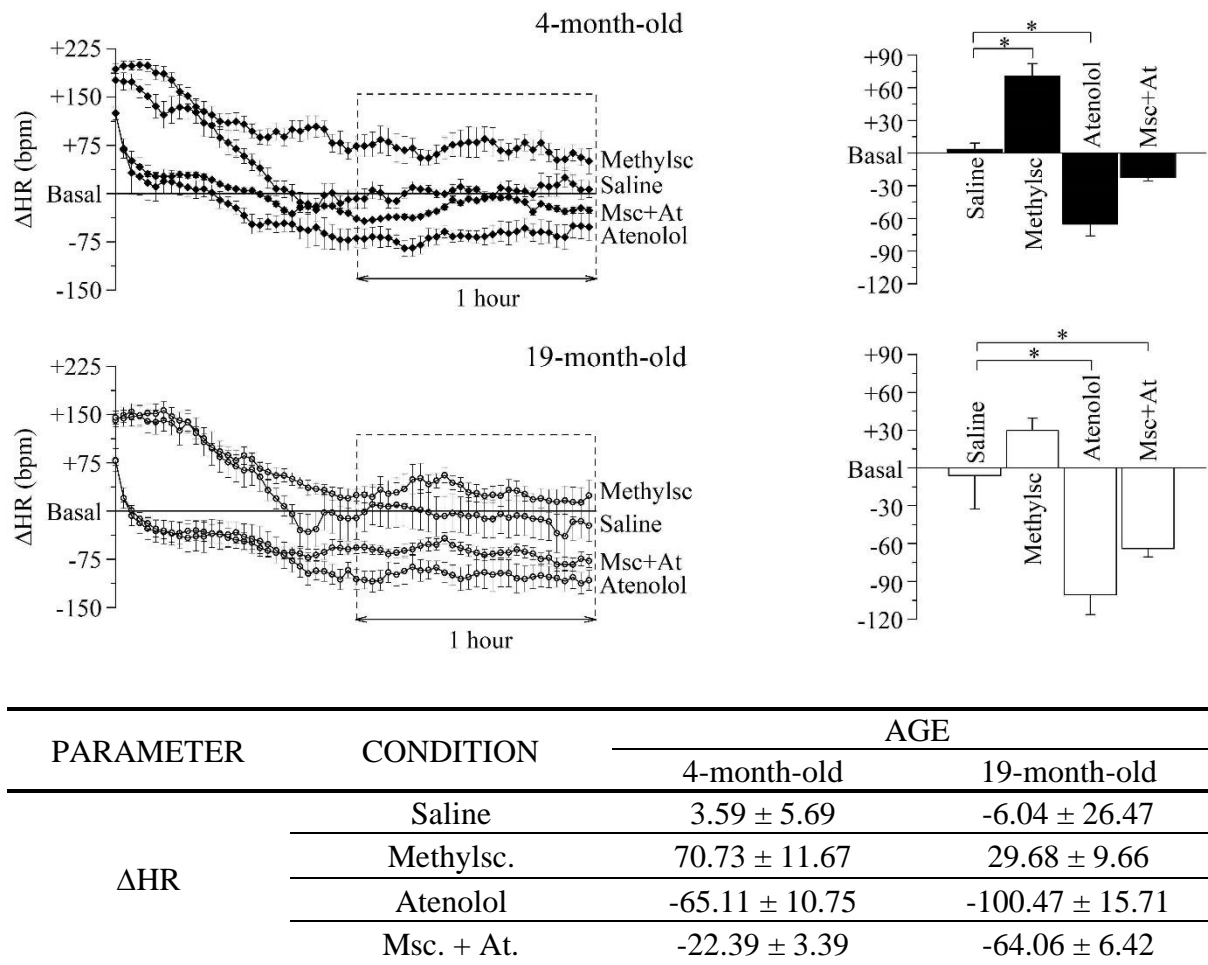


Figure 35. Age-related differences in mice autonomic modulation of heart rate.

Heart rate changes (Δ HR) after i.p. injection of vehicle (Saline) and autonomic modulator drugs (Methylscopolamine, Atenolol and Methylscopolamine+Atenolol) in adult (4 -months-old, n=10) and aged (19-months-old, n=9) freely-moving mice. The left panels represent the time courses of the Δ HR recorded from the moment of the injection; each point represent the mean heart rate of a 2-min period. Saline was employed to identify the time span which is needed by the animals to recover from the handling-induced stress (60-120 min; i.e. when their heart rate returned similar to the mean state recorded 60 mins before drugs administration, Basal). The right panels report the mean Δ HR values recorded during the second hour post-injection (values in the table). Data are reported as mean \pm SEM; $p < 0.05$, one-way ANOVA for repeated measures followed by Fisher's LSD post-hoc test (from Piantoni et al., 2020 - submitted).

We also further proceeded to verify whether the effect of autonomic blockade could reveal aging associated differences. To this aim we compared the Δ HRs during each specific pharmacological manipulation and confirmed that both vagal and double autonomic blockade were different between the two age groups (Student's t-test, $p < 0.05$), while no difference was identified during sympathetic deprivation.

HRV responses to pharmacological autonomic blockades

BHR results from the complex balance of at least three main elements: IHR, sympathetic and parasympathetic drive. Results obtained in previous figures clearly illustrate that 4- and 19-month-old mice share similar BHR values, but the underlying relative contribution of the above-mentioned elements is different. To shed light on this point and better characterize the differences, HRV analysis was carried on the ECG traces collected during selective autonomic blockade (**figures 36** and **37**). In this case, we calculated differences in the HRV indexes obtained in Basal (prior to treatments) and during the second hour following each autonomic manipulation or saline injection.

In 4-month-old mice (**figure 36**), vagal blockade (methylscopolamine) and double autonomic block (methylscopolamine+atenolol) significantly reduced SDNN, RMSSD, total power, HF, LF values compared with the control (saline) condition. Interestingly, sympathetic blockade alone did not result in significant changes in any index.

In 19-month-old mice (**figure 37**), unexpectedly, when compared to the saline (control) condition, vagal or sympathetic blockade alone did not result in significant changes in SDNN, RMSSD, total power, HF and LF. However, significant reductions of all HRV parameters were observed under double autonomic blockade. In addition, differences in LF/HF values were identified during double and sympathetic blockades.

Taken together these results point to a lower level of rate variability in aged mice, and this appear to be mostly associated with a decreased vagal component.

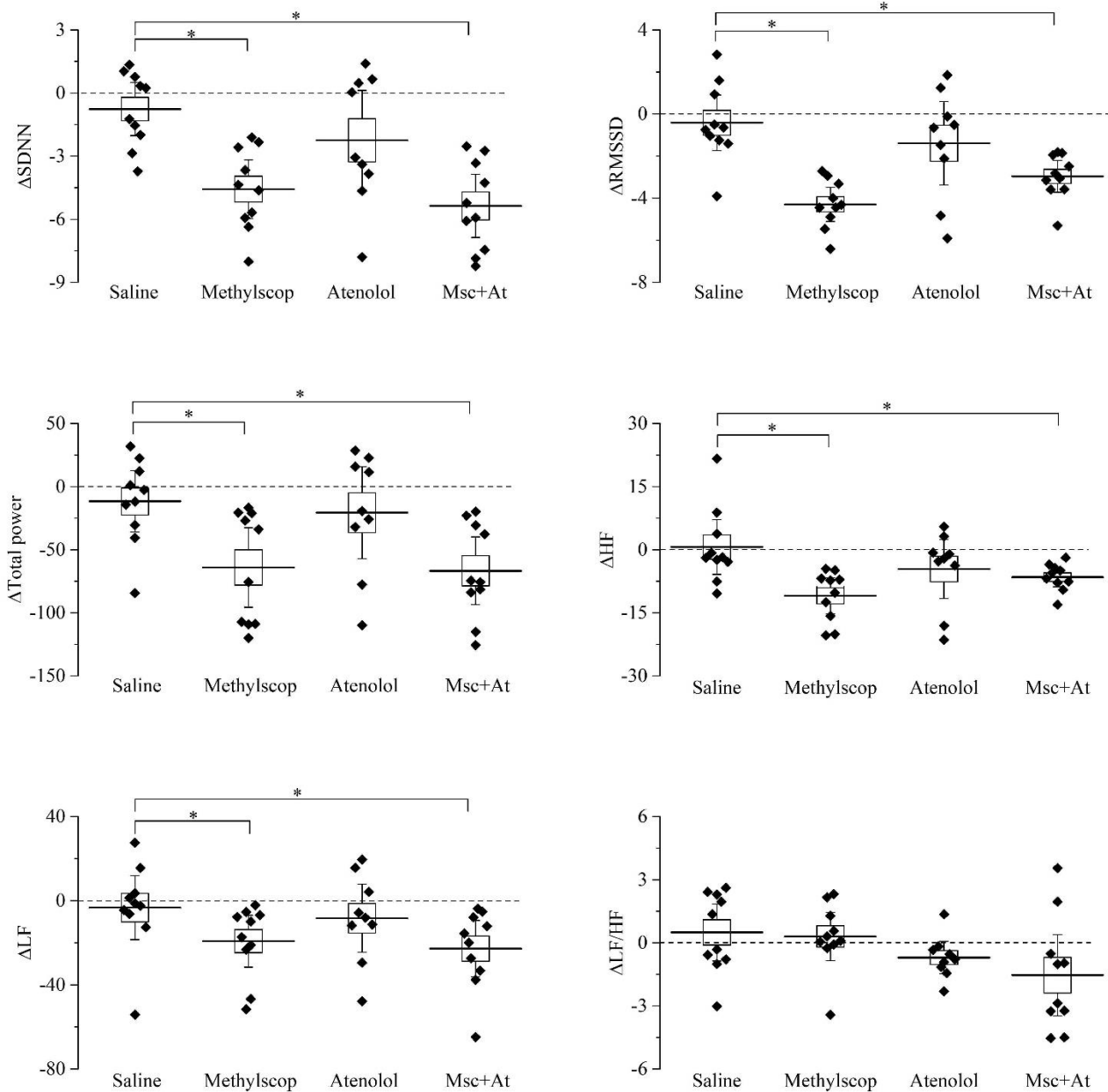


Figure 36. HRV parameters response to pharmacological autonomic blockade in 4-month-old mice.

Changes in HRV parameters calculated from ECG traces recorded from 60 to 120 min after i.p. injection of vehicle (saline) and autonomic modulator drugs (Methyscopolamine, Atenolol, Methyscopolamine+Atenolol) in 4-month-old (n=10) freely-moving mice. The dotted line indicates the mean BHR value recorded 60 min before drug administration. In the box chart, middle line indicates the mean value, delimiting lines of the box are confidence intervals at 95% and whiskers represent SEM; $p < 0.05$, one-way ANOVA with repeated measures followed by Fisher's LSD post-hoc test (from Piantoni et al., 2020 – submitted).

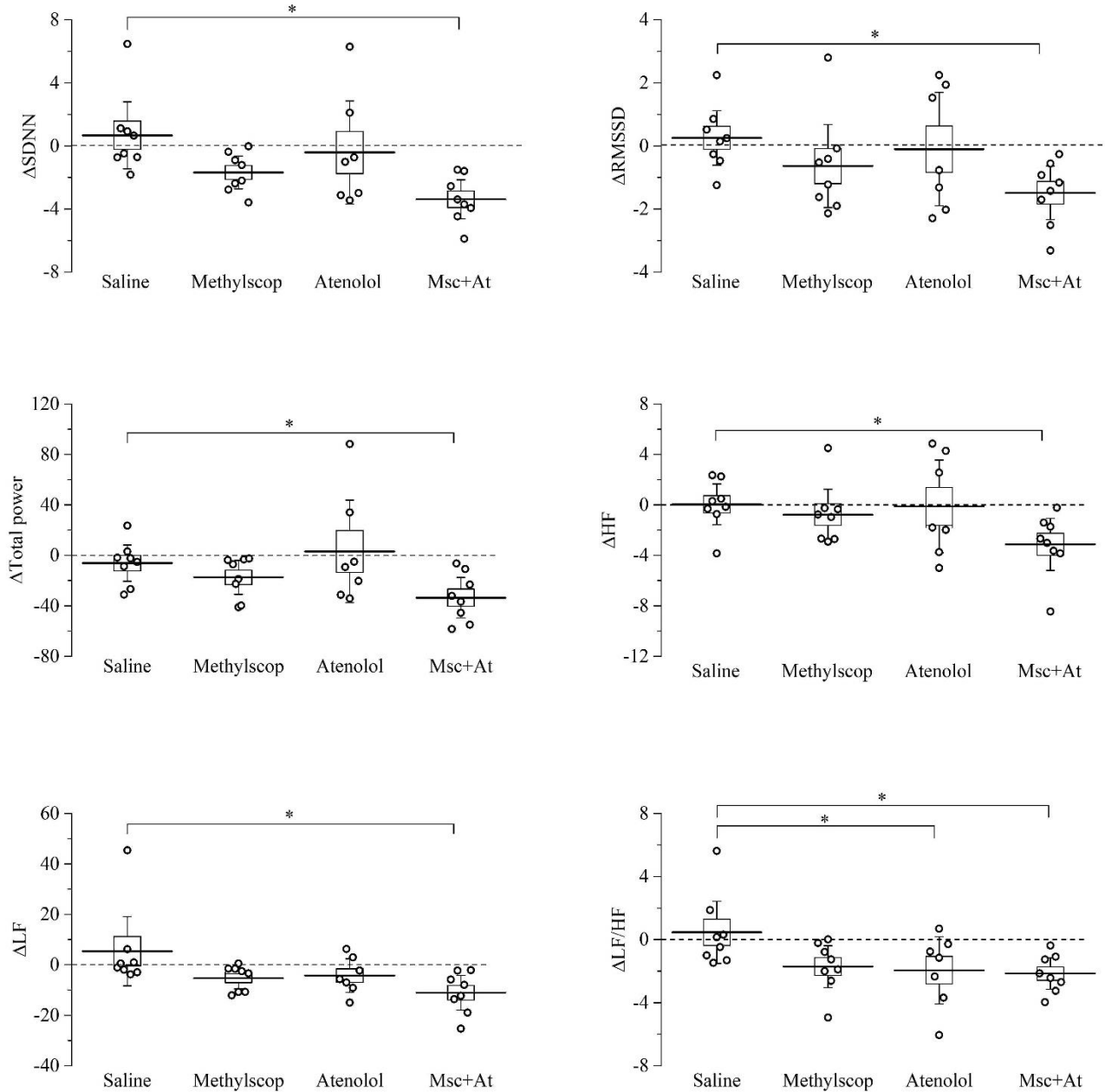


Figure 37. HRV parameters response to pharmacological autonomic blockade in 19-month-old mice.

Changes in HRV parameters calculated from ECG traces recorded from 60 to 120 min after i.p. injection of vehicle (saline) and autonomic modulator drugs (Methyloscopamine, Atenolol, Methyloscopamine+Atenolol) in 19-month-old (n=9) freely-moving mice. The dotted line indicates the mean BHR value recorded 60 min before drug administration. In the box chart middle line indicates the mean value, delimiting lines of the box are confidence intervals at 95% and whiskers represent SEM; p<0.05, one-way ANOVA with repeated measures followed by Fisher's LSD post-hoc test (from Piantoni et al., 2020 - submitted).

Vulnerability to cardiac arrhythmias

A more rigid chronotropism (i.e. a reduced HRV) is a pro-arrhythmic marker in humans; therefore, based on previous results, and with the overall aim to test whether the mouse is a reasonable experimental model for cardiac aging investigations, we further proceeded to verify the propensity to arrhythmias in the two age groups.

In **figure 38**, representative recordings (panel **A**) and mean cumulative data (panel **B**) of the arrhythmic events observed in the mice are shown. During undisturbed daily recordings (**figure 38B, top**), the overall incidence of cardiac arrhythmias was significantly larger in 19-month-old mice compared to 4-month-old mice, without specific age-related differences in the incidence of the various arrhythmic subtypes.

Since an increased adrenergic background drive is also a well-known pro-arrhythmic condition, we repeated the analysis in the presence of adrenergic stimuli with isoprenaline (ISO), and a similar larger overall incidence of cardiac arrhythmias was found in 19-month-old mice (**figure 38B, bottom**). Although this increase seems to be mainly due to ventricular arrhythmias, statistical analysis did not reach significance.

Of note, heart rate response to maximal ISO stimulation, measured as ΔHR , was significantly smaller in 19-month-old (171.4 ± 16.0 bpm, n=7) compared with 4-month-old mice (226.8 ± 14.3 bpm, n=8).

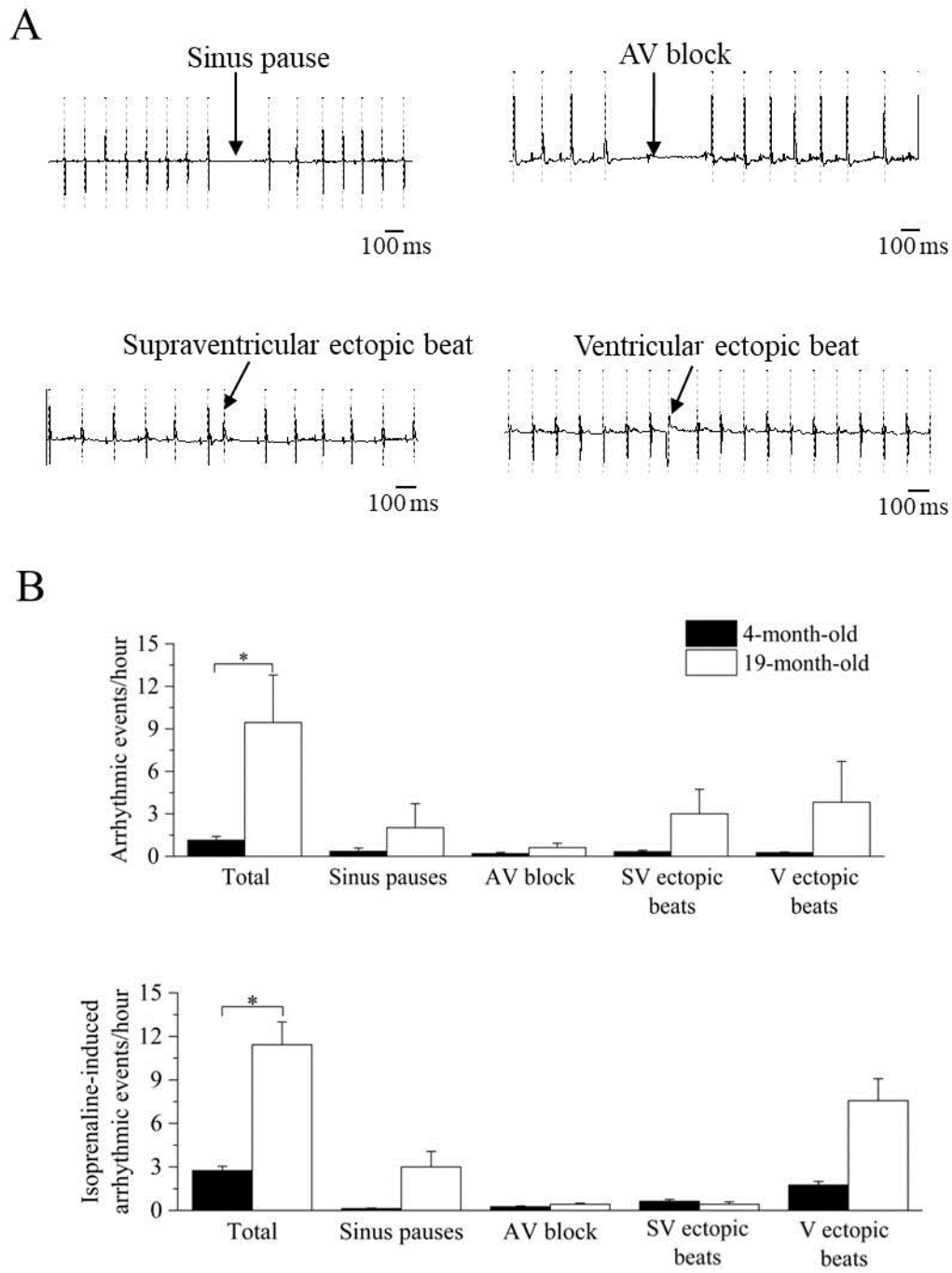


Figure 38. Analysis and classification of spontaneous and induced arrhythmic events occurred in 4- and 19-month-old mice.

(A) Sample ECG traces of four different types of arrhythmic events: sinus pause, atrioventricular block, supraventricular and ventricular ectopic beat. (B) Mean \pm SEM values of the spontaneous (TOP) and isoprenaline-induced (BOTTOM) total and type-specific (sinus pauses, atrioventricular block, supraventricular and ventricular ectopic beats) arrhythmic events. Comparisons were evaluated by Student's t-test, $p < 0.05$ (from Piantoni et al., 2020 - submitted).

DISCUSSION

Age-related changes in cardiac ANS modulation in mice

Specific patterns of cardiac ANS modulation may vary across species, with possible species-typical sympathovagal balance¹²²⁻¹²⁴. For example, BHR is characterized by a relatively larger vagal prevalence in humans¹²⁵ while it is generally believed that mice have a sympathetically-dominated BHR¹²⁶⁻¹²⁸, thus questioning the translational relevance of the murine model for the study of cardiac ANS-related conditions.

In a recent study it is suggested that the murine organism operate under high sympathetic drive in order to maintain a normal core temperature in standard laboratory conditions (20°C), and that when mice are acclimated to their thermoneutral zone (30°C) for 3 days, sympathetic input to the heart is greatly reduced¹²⁸. However, one may argue that patterns of ANS modulation at 30°C might represent a transient physiological response to environmental alterations in mice that were born and raised at ~20°C. Moreover, it must be noted that previous attempts to characterize age-related ANS changes in mice were performed under general anesthesia (which may affect ANS function) or during short-term recordings (which do not take into account potential circadian effects on ANS function)¹²⁸⁻¹³⁰. Therefore, in the present study these limitations were overcome by assessing age-related changes in cardiac autonomic modulation using two different and complementary approaches: via HRV analysis of ECG signals obtained during daily recordings at standard laboratory temperature conditions (~22°C) in conscious mice of different age (4- and 19-months-old), and by evaluating heart rate responses to selective pharmacological autonomic blockades.

An age-related reduction in time- (SDNN, RMSSD) and frequency-domain (total power and HF bands) indexes of HRV were detected during both phases of the daily cycle (**figure 34B**), which recapitulates human findings¹³¹. The LF index was instead reduced only during daytime analysis. Importantly, evidence that age-related changes in HRV are not ascribable to changes in somatomotor activity levels were further provided. Relatedly, it was observed a significant increment in mean heart rate values under vagal blockade with methylscopolamine in 4-month-old, but not in 19-month-old, mice compared with the control (saline) condition (**figure 35**). Taken together, these data (see below the discussion on HRV indexes) are indicative of a decline in resting cardiac vagal modulation with advancing age that typically characterizes humans¹⁰⁸. On the other hand, adrenergic receptor blockade with atenolol led to a decrease in the average heart rate in both groups with a larger, albeit not significant effect observed in the 19 month-old group.

Notably, these age-related ANS changes were not reflected by concomitant changes in resting measures of heart rate. A potential explanation lies in the fact that the IHR was significantly lower in 19-month-old mice compared to the younger group. It has been suggested that changes in the mechanisms intrinsic to heart pacemaker cells may compensate for the aging-associated shift in the sympathovagal balance towards a sympathetic prevalence to preserve a stable BHR¹⁰⁸.

In interpreting these findings from a translational point of view, similarities and differences with the human condition have to be taken into consideration. First, the fact that muscarinic receptor blockade with methylscopolamine was associated with a significant increase of the average heart rate in the younger group suggests that in young adult mice vagal modulation plays a significant role in the regulation of BHR. It must be acknowledged, however, that the IHR in the young group was similar to the average BHR, confirming that, contrary to young adult humans¹²⁵, BHR in young adult mice is not predominantly modulated by vagal influences. Most importantly, these results indicate that mice exhibit age-related changes in cardiac ANS regulation (i.e., decline in vagal functioning) and automaticity of cardiac pacemaker cells (i.e., reduced IHR) that closely recapitulate those observed in human populations^{95,108-112}. Moreover, as in humans¹³², β -adrenergic receptor stimulation with isoprenaline provoked a smaller heart rate response in the older group. This result is in agreement with a previous study documenting a reduced sensitivity of the average heart beating intervals to β -adrenergic receptor stimulation in the isolated SAN tissue of older mice¹²⁹. Therefore, these results confirm and strengthen the reliability of the murine model for the study of age-related cardiac ANS conditions.

Utility of HRV indexes in detecting age-related changes in murine cardiac ANS modulation

HRV can be separated into various components, reflecting ANS influence on cardiac control, and its analysis has become a popular approach in several investigational domains, both in human and animal research¹³³⁻¹³⁵. Specifically, in humans the SDNN is thought to reflect all the cyclic components responsible for variability, and the SDNN squared is equivalent to the variance (total power) when observed in the frequency domain¹³⁶. The RMSSD and the HF component of HRV detect quick beat-to-beat fluctuations in a heart period time series, primarily reflecting vagal modulation¹³⁵. In this study, the reliability of RMSSD and HF band to assess vagally-mediated HRV is corroborated since in 4 month-old mice it is observed a substantial reduction

of these indexes following muscarinic receptor blockade with methylscopolamine (**figure 36**). Relatedly, vagal blockade, but not sympathetic blockade, modulates SDNN and total power values, suggesting that a prevalent vagal influence mediates HRV in mice. This finding well correlates with the evidence that vagal block in young adult mice significantly modifies heart rate in this age group. Notably, the effect of vagal blockade on HRV indexes was significant in 4-month-old but not in 19-month-old mice (**figure 36 and 37**) in agreement with the above discussed decline in resting cardiac vagal functioning in the older group. Furthermore, although the LF component of HRV has been theorized to represent both sympathetic and vagal influences^{137,138}, findings of reduced LF values following vagal, but not sympathetic, blockade in the young group suggest that the LF band (0.15–1.5 Hz in this study¹¹⁷) captures predominantly vagal influences in mice. This result questions the traditional interpretation of the LF to HF ratio as an index of sympathovagal balance in mice, as already pointed out in humans^{135,139}. In fact, no differences were found in daily values of LF/HF between the two groups, despite clear pharmacological evidence of an age-dependent shift of the sympathovagal balance towards an increased sympathetic drive. In the light of these considerations, the use of vagally-mediated HRV indexes is to be considered a fundamental tool for capturing the decline in cardiac vagal modulation in mouse models of aging. However, it must be noted that while HRV alterations are often ascribed solely to changes in ANS signaling, age-related changes in HRV in mice have also been associated with deterioration of autonomic neuronal receptor signaling and mechanisms intrinsic to heart pacemaker cells¹²⁹.

Age-related changes in the vulnerability to cardiac arrhythmias

Reduced vagally-mediated HRV has been proposed as a prognostic marker of increased mortality and susceptibility to lethal ventricular arrhythmias in cardiac patients¹⁴⁰⁻¹⁴², and associated with increased CVD morbidity and mortality in the elderly¹⁴³.

In this study 19-month-old mice exhibited, alongside reduced vagally-mediated HRV, a larger vulnerability to both spontaneous and pharmacologically-(isoprenaline-)induced cardiac arrhythmias compared to 4-month-old mice (**figure 38**). Arrhythmias were both of supraventricular (e.g., sinus pauses, supraventricular ectopic beats) and ventricular (ventricular ectopic beats) origin, with no clear chamber prevalence. It must be acknowledged that the incidence of arrhythmias was relatively modest even in the older group. In fact, one of the major limitations of this study is that only two age groups were employed, with the older group likely representing an

early phase of the aging process in this mouse strain. Therefore, we cannot exclude that arrhythmogenesis would be more evident in older mice. Notably, in humans premature atrial and ventricular complexes are frequently present in the healthy elderly population, even in the absence of apparent structural abnormalities¹⁰¹⁻¹⁰³. For example, in the Cardiovascular Health Study¹⁴⁴, 24-h ambulatory monitoring in 60- to 85-year-old healthy individuals showed that 86% of patients had premature atrial complexes, with 26% having >36 premature atrial complexes/h. Premature ventricular complexes were found in 82% of elderly subjects, including runs of non-sustained ventricular tachycardia. Importantly, a high burden of premature ventricular complexes was associated with increased left ventricular systolic dysfunction, incident heart failure, and mortality among the participants of this study¹⁴⁵. However, despite promising and preliminary results on the utility of vagally-mediated HRV indexes for predicting arrhythmic risk in rodents^{116,130}, it is premature to assume that decreased vagally-mediated HRV in aged mice can be regarded as a negative prognostic indicator of CVD risk. Nevertheless, the preliminary association found in this study between decline in cardiac vagal functioning and increased vulnerability to arrhythmias with advancing age encourages future mouse research aimed at investigating the causal role of age-related perturbations in ANS in the proarrhythmic electrical remodeling of the heart.

In conclusion, keeping inherent limitations in mind¹²⁸, the results of this study support the utility of mouse models for investigating specific research questions related to aging of the cardiac ANS. Indeed, while one of the major advantages of using mice as an aged model is their short lifespan, available research, including the present investigation, is mostly cross-sectional^{129,146}. Consequently, these results warrant future longitudinal studies adopting HRV measures to investigate the trajectory of vagal decline with advancing age in conscious mice. Moreover, these data prompt future research aimed at unveiling the mechanisms underlying the relation between aging of the ANS, decline in vagally-mediated HRV, and proarrhythmic remodeling of the mouse heart.

SODIUM CHANNEL MUTATIONS

INTRODUCTION

In 2015, a two years-old baby was recovered at the Azienda Ospedaliera Papa Giovanni XXIII (Bergamo, Italy) presenting a severe but asymptomatic bradycardia and recurrent arial flutter episodes; furthermore, Verapamil administration induced a QT interval prolongation. The final diagnosis was sinus node disease and the patient was implanted with a pacemaker¹³.

The genetic analysis displayed the presence of a compound heterozygous mutation for both the paternal and maternal allele of the α -subunit of the cardiac sodium channel (SCN5A). The paternal one is a missense mutation located in the D4:S2 transmembrane segment (Lys1578Asn or K1578N); the maternal one is a frame-shift mutation located at the C-terminus of the protein (Gly1866fs or G1866fs), resulting in a shortened protein (Δ 150 amino acids) (**figure 39**). Family history was unremarkable and both parents were asymptomatic and with normal ECGs.

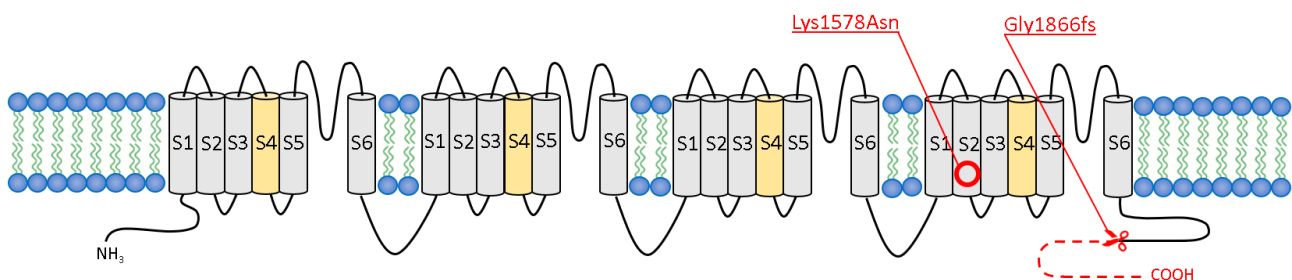


Figure 39. Localization of the two mutations analyzed in this study.

The paternal mutation (Lys1578Asn) is located in the transmembrane S2 segment of the fourth monomer while the maternal mutation (Gly1866fs) is a frame-shift alteration that causes a shortened C-terminus.

Sinus Node Dysfunctions (SNDs) are cardiac conduction disorders characterized by symptomatic dysfunction of the SAN, often associated with senescence of the node and surrounding atrial myocardium¹⁴⁷. Although the term "*sick sinus syndrome*" was first used to describe the sluggish return of SAN activity following electrical cardioversion, it is now commonly used to describe the inability of the SAN to generate an heart rate commensurate with the physiological needs of an individual¹⁴⁸. Since the SAN is the natural pacemaker of the heart, typical symptoms of SND include syncope, dizziness, palpitations, exertional dyspnea, easy fatigability from chronotropic incompetence, heart failure, and angina¹⁴⁷. However, early SND may be latent and

some individuals may remain asymptomatic¹⁴⁹. These diseases can be both familial, i.e. genetically encoded, or sporadic, i.e. not correlated with gene inheritance. The latter are clearly the most prevalent kind and their causes can be divided in extrinsic, intrinsic or both. A retrospective study¹⁵⁰ displayed that in patients hospitalized for compromising bradycardia, 51% of cases were attributable to an extrinsic cause, such as an adverse drug reaction, electrolyte imbalance or acute myocardial infraction. In the other 49% the etiology was not clear. Historically, SND has often be associated with fibrosis and cellular senescence^{98,99}.

In cardiac SAN myocytes, the presence of Na_v1.5 channels has long been debated. There is now evidence that in most of the animal model investigated, Na_v1.5 channels are absent or scarce in the center of the SAN, while they are widely expressed in the periphery where they functionally contribute to impulse conduction¹⁵¹⁻¹⁵³. Despite their absence in the center of the SAN, there are lots of evidences that many SCN5A mutations are associated with inherited SND, such as bradycardia and sinus exit block¹⁵⁴.

As previously described, the SCN5A gene can be expressed in a series of alternative splicing variants. Among these, the inclusion of two alternative exons 6 (A-B) characterizes the adult and the neonatal isoform¹⁴ (**figure 40**). Although very little is known about the human isoform switch, it has been observed a very fast afterbirth switch from the neonatal to the adult isoform in rats^{155,156}.

Adult Na_v1.5 channels presents the B-exon while the neonatal form is characterized by the presence of the A-exon, resulting in a difference of 7 amino acids. Notably, the replacement of a negatively charged aspartate with a positively charged lysine leads to a charge-reversal in neonatal channel specifically in the region immediately adjacent to the voltage sensor of domain I. This could explain the positive shift of the activation curve of this isoform compared to the adult one¹⁴.

Given the high number of splice variants, several protein isoforms of the neonatal/adult Na_v1.5 channel can be generated. The presence (or absence) of a glutamine in position 1077 (exon 18) represents another common splicing modification^{15,157} (**figure 40**).

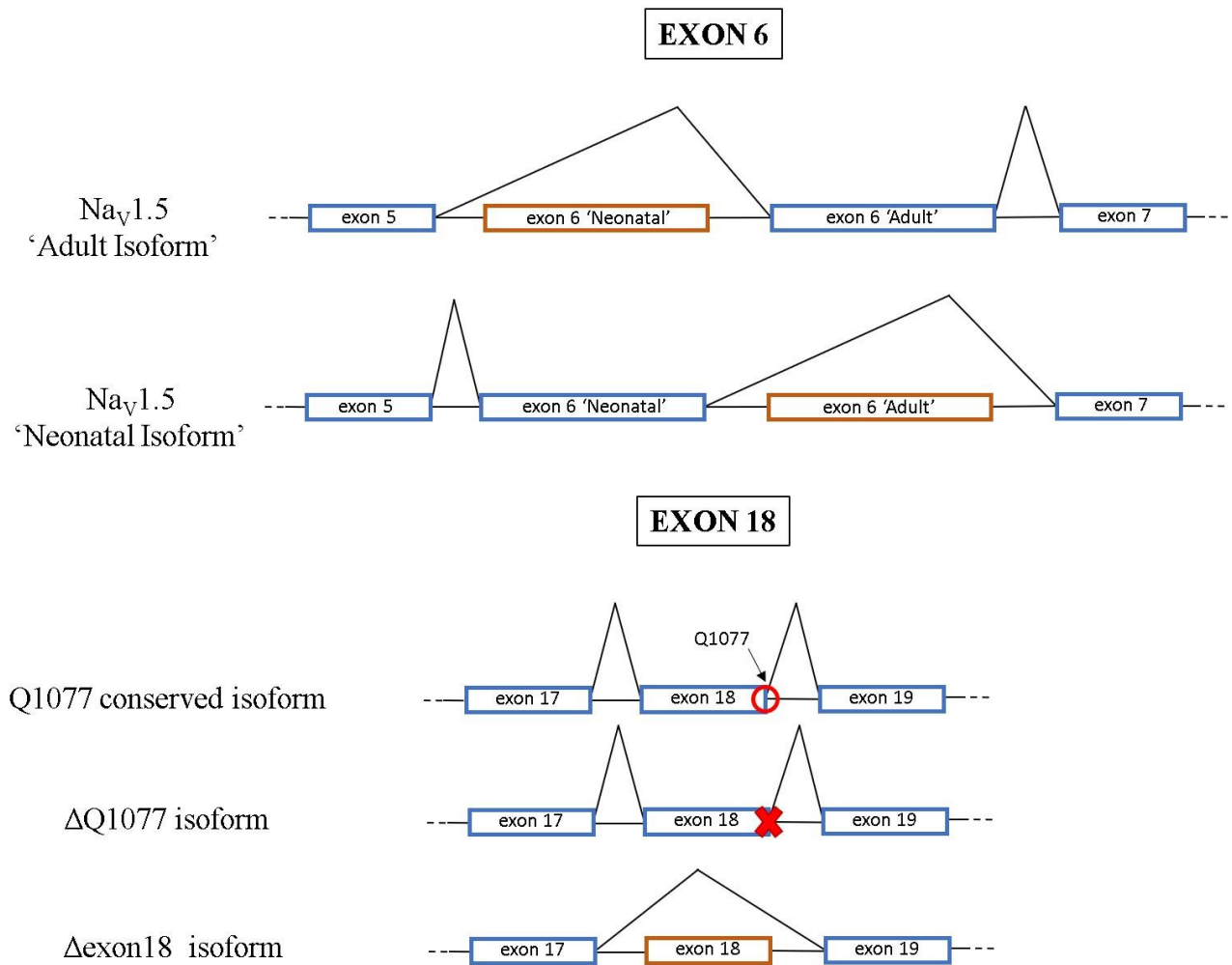


Figure 40. Illustrative scheme of the main SCN5A gene splice variants.

Na_v1.5 channel is expressed in several different physiological isoforms since the SCN5A gene can undergo a series of alternative splicing events. Among these, the two main splicing regions are exon 6 (adult/neonatal isoform) and exon 18.

AIMS

Channelopathies are a heterogeneous group of diseases resulting from defects in ion channels by both genetic or acquired factors¹⁵⁸. Among these, alterations in the function of the cardiac voltage-gated sodium channel gene (SCN5A) often generate severe problems in the heart function¹². The aim of this project, in collaboration with Azienda Ospedaliera Papa Giovanni XXIII (Bergamo, Italy), is to characterize the electrical features of two mutations of this gene (K1578N - G1866fs). The patient, a two years-old baby, carried both the alterations and is affected by a severe but asymptomatic bradycardia, recurrent arial flutters and drug-inducible QT prolongation; on the other hand, the parents, who express a heterozygous mutation each, do not present any relevant symptom.

In addition, since the sodium channel Na_v1.5 undergoes a switch from a neonatal to an adult isoform, we investigated whether this phenomenon could affect the clinical outcome of the patient during his life.

MATERIALS AND METHODS

Cell culture

HEK-293 (human embryonic kidney-293) cells were used as an heterologous model for the evaluation of the biophysical properties of WT/mutated Na_v1.5 channels. This cell line is characterized by a physiological reduced expression of ion channels so it is widely used for electrophysiology analysis¹⁵⁹.

Cells were maintained at a 37°C in an incubator with 5% CO₂, cultured in DMEM (Dulbecco's Modified Eagle's Medium, Life Technologies) supplemented with 10% FBS (Fetal Bovine Serum, Life Technologies), 1% sodium pyruvate (Sigma-Aldrich), 1% L-Glutamine (Sigma-Aldrich), 0.5% Penicillin and 0.5% Streptomycin (0.1 mg/mL and 100 U/mL, Sigma-Aldrich, respectively).

Plasmids generation and transfection

The adult wild type human SCN5A vector was kindly provided by Dr. F. Charpentier (Université de Nantes, France).

The neonatal (Neo) wild type human SCN5A isoform, as previous mentioned, differs from the adult one only by 7 amino acids: T206V, T207S, F209N, V210I, D211K, V215L, and S234P (**figure 41**). These differences, as well as mutations K1578N and G1866fs, were introduced in the genetic sequence of the adult isoform through a site-directed mutagenesis kit (QuikChange II XL Site-Directed Mutagenesis Kit, Agilent Technologies), using the following primers:

F: 5'-cacagggcagtgattgtcaacctggctgcctgc-3'

K1578N

R: 5'-gcagggcagccaggtgacaatacactcgctgtg-3'

F: 5'-tcctgggggagtcagctctggggagatggac-3'

G1866fs

R: 5'-gtccatctccccagactgactccccagga-3'

Both the adult and the neonatal isoform used in these experiments do not present the glutamine (Q) located in position 1077 (exon 18) since this variant is the most expressed in the population. Automated DNA sequence analysis (BioFab Research, Italy) was performed to verify the presence of the mutations in the channel sequence.

Finally, SCN1 β -1B (the most expressed isoform of the SCN1 β gene) sequence was fused with the GFP (Green Fluorescent Protein) reporter sequence.

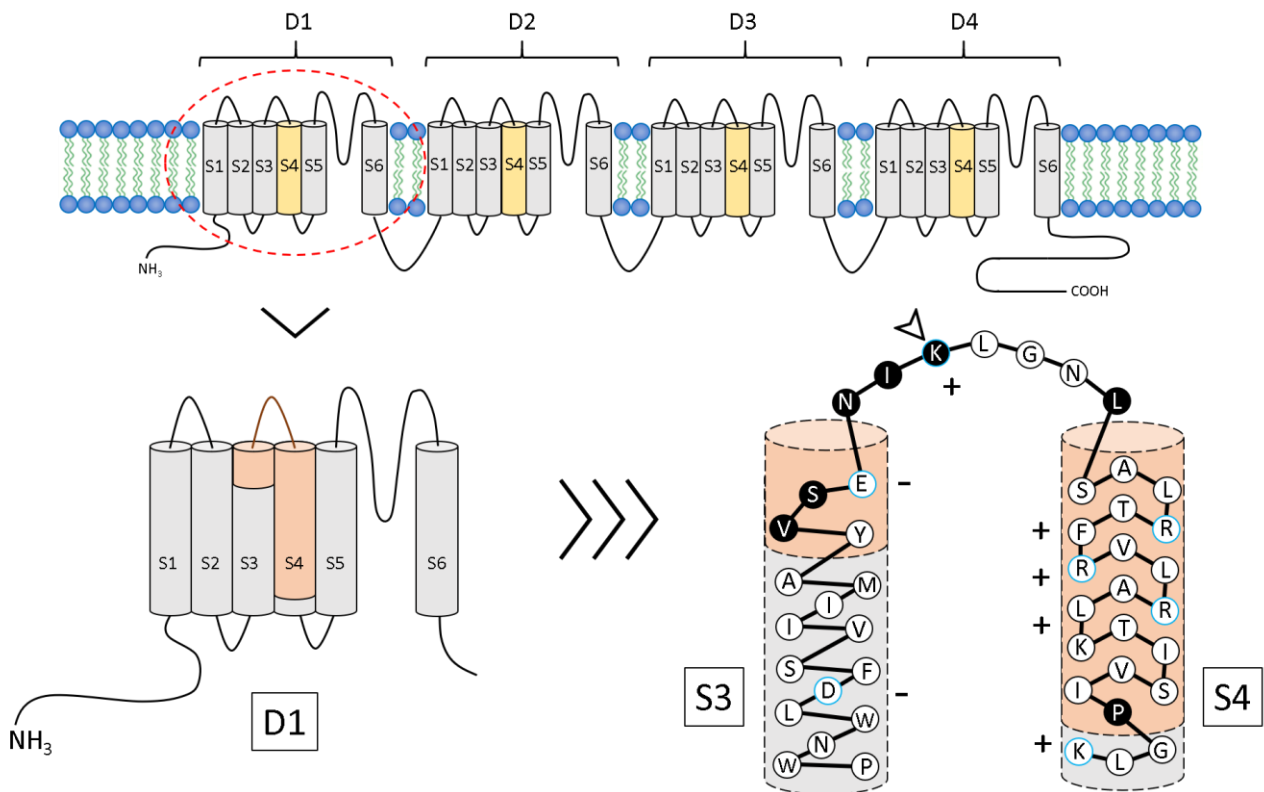


Figure 41. Differences in the amino acids sequence between Adult and Neonatal Na v 1.5 channel isoforms.

The different amino acids (black circles/white lettering) between Adult and Neonatal Na v 1.5 channel isoforms are located mainly in the C-terminal end of D1:S3 and the S3/S4 linker region of the channel, close to the four positively charged residues of the voltage-sensing S4. The arrow indicates a “charge-reversing” amino acid change (i.e. negative aspartate (D) in Adult to positive lysine (K) in Neonatal exon 6 – this could explain the positive shift of the activation curve in the Neonatal isoform). All charged amino acids are circled in blue.

36 hours before the patch-camp experiment, HEK293 cells were plated on 35-mm Petri dishes and transfected with 1 μ g of expression vector (pCI) containing the accessory β -subunit protein SCN1 β -1B and:

- 1 μ g of WT (WT adult isoform);
- 1 μ g of Neo (WT neonatal isoform);
- 0.5 μ g of WT + 0.5 μ g of WT-K1578N (paternal mutation - heterozygous);
- 0.5 μ g of WT + 0.5 μ g of WT-G1866fs (maternal mutation - heterozygous);
- 0.5 μ g of WT-K1578N + 0.5 μ g of WT-G1866fs (adult isoform, compound mutation);

- 0.5 μg of Neo-K1578N + 0.5 μg Neo-G1866fs (neonatal isoform, compound mutation);
using ViaFect™ transfection reagent (Promega).

The day after the transfection procedure, cells were dispersed using trypsin-EDTA and plated at low density on 35-mm plastic Petri dishes. The following day, only GFP-expressing single cells were selected for the patch. All the experiments were performed in whole-cell configuration at room temperature ($\sim 25^\circ\text{C}$).

Patch clamp solutions

During the experiments, cells were maintained in standard Tyrode (**table 2**) while the extracellular solution used to acquire the Na^+ current included (mM): NMDG-Cl 100, NaCl 30, CsCl 5, Hepes 10, MgCl₂ 1.2, CaCl₂ 2 and Glucose 5, pH 7.4. It displays a reduced Na^+ concentration compared to standard Tyrode and KCl was replaced with CsCl in order to inactivate possible K^+ currents. Patch-clamp pipettes with a resistance of 1-3 M Ω were filled with an internal solution containing (mM): CsCl 130, NaCl 10, MgCl₂ 1, Hepes 10, EGTA 10, Na 2ATP 2, pH 7.2.

Protocols and data analysis

Na^+ currents were elicited applying depolarizing voltages steps from -80 to +20 mV from a holding potential of -120 mV (where the opening probability is maximal).

Inactivation curves were obtained by maintaining cells at holding potential of -100 mV and applying depolarizing steps of 1s from -140 mV to 0 mV.

The recovery from inactivation was analyzed through a double pulse protocol. Cells were depolarized to 0 mV for 50 ms from a holding potential of -120 mV, then maintained to the holding potential for a variable interval of time (from 0.4 to 32.2 ms) and a second step of 50 ms to 0 mV was then delivered.

All the traces were filtered at 10 kHz.

Current-voltage relationships were calculated using the following equation: $I = g_{max} * (E - E_{rev})$, where “ I ” is the peak current amplitude; “ g_{max} ” is the maximal conductance; “ E ” is the voltage applied; “ E_{rev} ” is the Na^+ reversal potential, calculated for each cells (experimental theoretical E_{rev} : 28.23 mV, calculated with the Nernst equation).

The conductance (g) was determined as the slope of the linear fitting of the mean current density values at 10 and 20mV, where the open probability of the channels is maximal so the influence of the activation curve is absent.

Activation/inactivation curve data were fitted according to Boltzmann equation: $y=1/(1+\exp((V - V_{1/2})/s))$ for inactivation and $y=1/(1+\exp(-(V - V_{1/2})/s))$ for the activation; “V” is the voltage applied, “ $V_{1/2}$ ” is the half-activation value and “s” is the slope.

Recovery curve data were instead fitted with the following mono-exponential function: $y=A*\exp(-x/t)+y_0$, where: “A” is the current amplitude, “x” is the time, “t” is the time constant and “ y_0 ” represents the percentage of channels that have already recovered from the inactivation.

RESULTS

After the generation of the neonatal and mutated SCN5A vectors, HEK-293 cells were transiently transfected with both the β - and different α -subunits sequences to perform patch-clamp studies on the electrical properties of the WT and altered forms of the Na v 1.5 channel.

First of all, adult and neonatal WT isoforms were compared in order to functionally assess the electrophysiological differences between the two channels (**figure 42**).

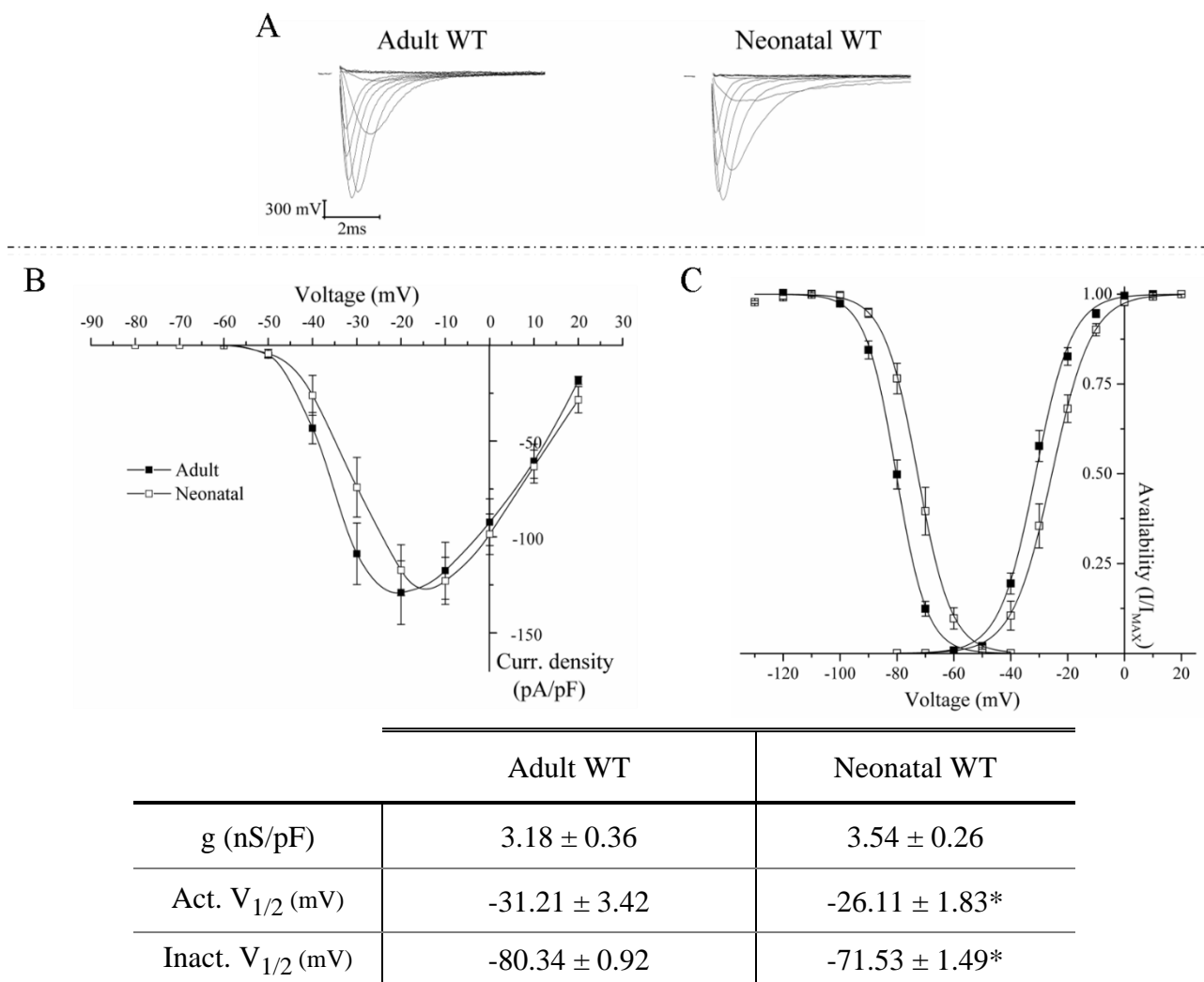


Figure 42. Differences in Na⁺ current features between WT Adult and WT Neonatal Na v 1.5 channel isoforms.

(A) Representative current traces recorded in whole-cell configuration in HEK-293 cells transfected with WT adult and WT neonatal Na v 1.5 channel isoforms (as indicated). (B) Current/voltage relationships in the WT adult (filled squares, n=10) and WT neonatal (empty squares, n=11) isoforms; each point indicate the mean \pm SEM value at that voltage. (C) Activation/inactivation curves recorded in WT adult (n=10/25) and WT neonatal (n=11/9) isoforms (same meaning of color); each point indicate the mean \pm SEM value at that voltage while the full lines indicate the Boltzmann fitting of data-points. Mean V_{1/2} and g values are indicated in the table; *p<0.05 vs adult WT, two-sample Student's t-test.

From our studies, the current densities of the two isoforms appear very similar, though they reach their peak at different voltages (**figure 42B**). We therefore proceeded to evaluate the conductance (g), obtained as the slope of the linear fit after the peak (where the current availability is maximal, **figure 42C**) and, since these two isoforms do not display significant differences in this parameter (two-sample Student's t-test, $p > 0.05$), we confirmed that they carry a comparable Na^+ current.

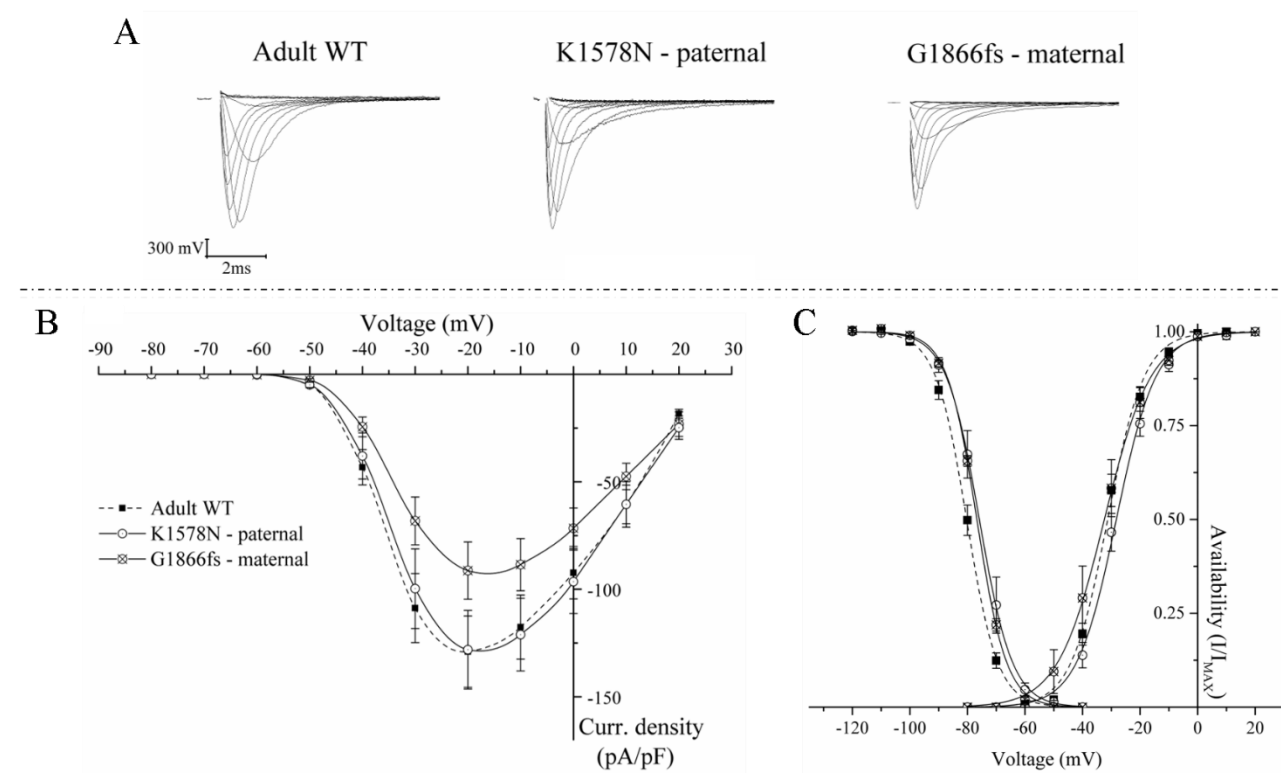
An investigation on the activation/inactivation properties (**figure 42C**) showed a positive shift in the WT neonatal isoform of both the curves compared to the WT adult (Act. curve shift: +5.10 mV; Inact. curve shift: +8.81 mV).

In order to recapitulate the effects of the mutations in the parents situation, HEK-293 cells were transfected with the adult SCN5A gene sequence carrying each mutations in heterozygosis (paternal: adultSCN5A-K1578N; maternal: adultSCN5A-G1866fs; **figure 43**).

For what concerns the paternal one (K1578N), as displayed in **figure 43B** and **C**, both the current density and the activation curve were not affected by the mutation (vs adult WT, two-sample Student's t-test, $p > 0.05$), however a positive shift of the inactivation curve was observed (shift: +4.83 mV) when compared to the WT adult isoform.

On the other hand, the maternal mutation (G1866fs) showed a clear reduction in the current density (peak difference vs WT adult: -29.24%); the analysis of the conductance confirmed this result. In addition, the activation curve was not altered (vs adult WT, two-sample Student's t-test, $p > 0.05$) but a positive shift influenced the position of the inactivation curve (shift: +10.73 mV).

No statistical differences were observed between the activation/inactivation properties between the two mutant isoforms ($p > 0.05$, two-sample Student's t-test).

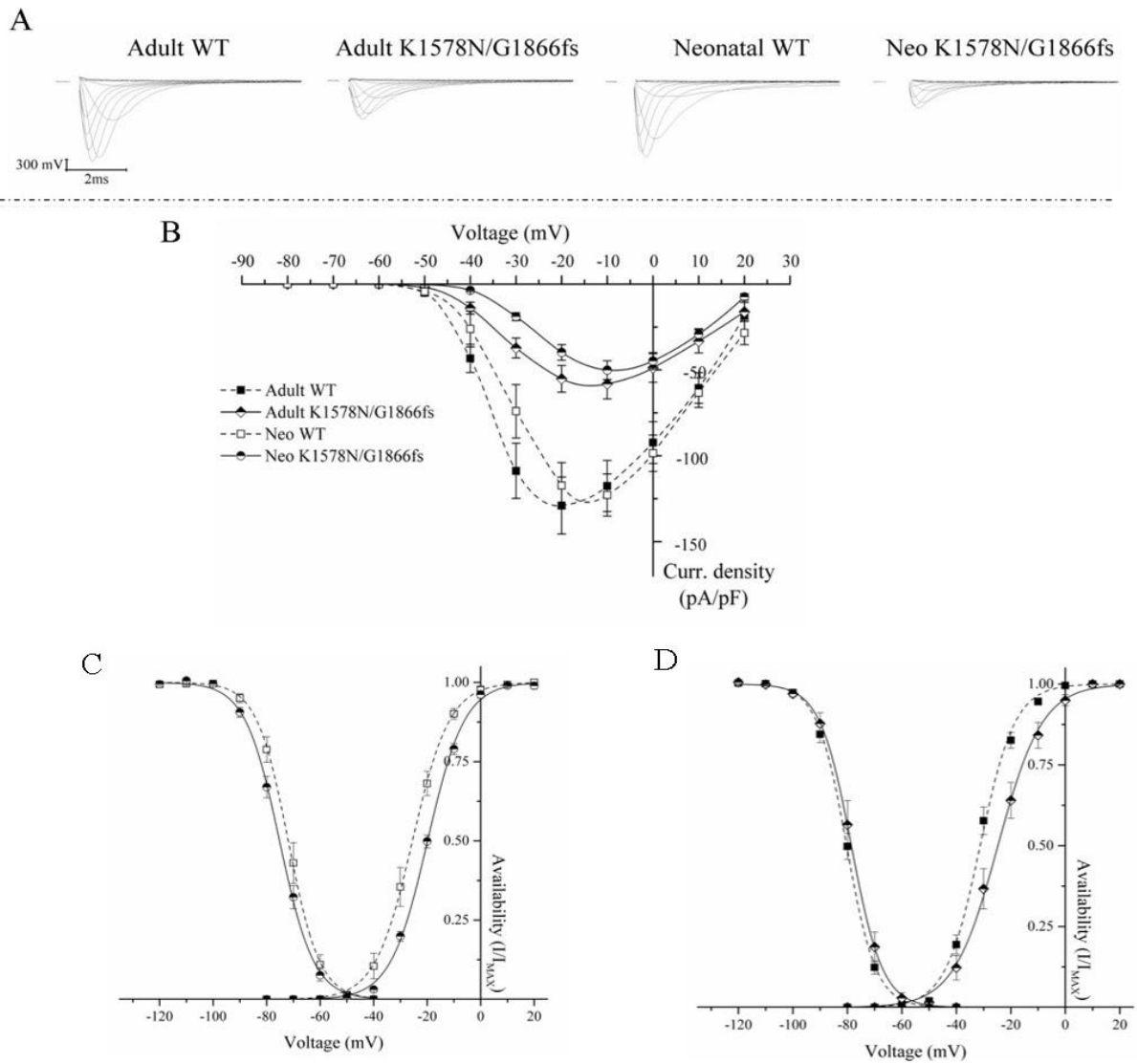


	Adult WT	Adult-K1578N	Adult-G1866fs
g (nS/pF)	3.18 ± 0.36	3.60 ± 1.32	2.35 ± 1.10*
Act. V _{1/2} (mV)	-31.21 ± 3.42	-28.40 ± 1.43	-32.45 ± 2.54
Inact. V _{1/2} (mV)	-80.34 ± 0.92	-75.51 ± 1.82*	-69.61 ± 6.94*

Figure 43. Differences in Na⁺ current features between the adult Na_v1.5 carrying the parental heterozygous mutations (K1578N – G1866fs) and the WT adult isoform.

(A) Representative current traces recorded in whole-cell configuration in HEK-293 cells transfected with the adult Na_v1.5 channel isoform carrying the paternal (K1578N) and the maternal (G1866fs) mutations in heterozygosis and the WT adult isoform (as indicated). (B) Current/voltage relationships recorded in adult-K1578N (white circles, n=9) and adult-G1866fs (crossed circles, n=12) compared to the WT adult isoform (filled squares); each point indicate the mean ± SEM value at that voltage. (C) Activation/inactivation curves recorded in adult-K1578N (n=9/5) and adult-G1866fs (n=12/10) compared to the WT adult isoform (same meaning of color); each point indicate the mean ± SEM value at that voltage while the full/dashed lines indicate the Boltzmann fitting of data-points. Mean V_{1/2} and g values are indicated in the table; *p<0.05 vs adult WT, two-sample Student's t-test.

To reproduce the condition of the patient, the compound mutation K1578N/G1866fs was introduced in the neonatal SCN5A isoform and HEK-293 cells were transfected with this genetic sequence. In this case we observed a great reduction in the current density (peak difference vs WT neonatal: -59.23%, **figure 44A, B**). Furthermore, a positive shift of the activation curve was identified (shift: +6.46 mV), while no statistical differences (p>0.05 vs neonatal WT, two-sample Student's t-test) were observed for what concerned the inactivation properties (**figure 44C**).



	Adult WT	Adult-K1578N/G1866fs	Neonatal WT	Neonatal-K1578N/G1866fs
g (nS/pF)	3.18 ± 0.36	1.84 ± 0.26* [#]	3.54 ± 0.26	1.72 ± 0.21* [#]
Act. V _{1/2} (mV)	-31.21 ± 3.42	-27.17 ± 2.39	-26.11 ± 1.83*	-19.65 ± 0.66* ^{#§}
Inact. V _{1/2} (mV)	-80.34 ± 0.92	-78.37 ± 1.66 [#]	-71.53 ± 1.49*	-75.03 ± 1.06*

Figure 44. Differences in Na⁺ current features between the adult and neonatal Na_v1.5 isoform carrying the compound mutations (K1578N/G1866fs) and the WT adult and neonatal isoforms.

(A) Representative current traces recorded in whole-cell configuration in HEK-293 cells transfected with the adult and neonatal Na_v1.5 channel isoforms carrying both the paternal (K1578N) and the maternal (G1866fs) mutations and the WT adult and neonatal isoforms (as indicated). (B) Current/voltage relationships recorded in adult-K1578N/G1866fs (half-filled squares, n=5) and neonatal-K1578N/G1866fs (half-filled circles, n=29) compared to the WT adult (filled squares) and WT neonatal (empty squares) isoforms; each point indicate the mean±SEM value at that voltage. (C) Activation/inactivation curves recorded in neonatal-K1578N/G1866fs (n=29/24) vs neonatal WT and (D) adult-K1578N/G1866fs (n=5/7) vs adult WT (same meaning of color); each point indicate the mean±SEM value at that voltage while the full/dashed lines indicate the Boltzmann fitting of data-points. Mean V_{1/2} and g values are indicated in the table; *p<0.05 vs adult WT, [#]p<0.05 vs neonatal WT, [§]p<0.05 vs adult K1578N/G1866fs, two-sample Student's t-test.

Additionally, the compound mutation was expressed in the adult SCN5A isoform to verify whether the age dependent switch to the adult isoform could generate a recovery in the current features. The comparison of the current conductance did not revealed significant differences (vs adult WT, two-sample Student's t-test, $p > 0.05$, **figure 44B**), but a negative shift of the activation curve (-7.52 mV) was observed (**figure 44D**). However, this shift is comparable to that observed in their respective WT isoforms indicating that the mutated condition affects the activation kinetics equally in both the isoforms. No differences were instead observed in the inactivation gate kinetics which were very close to that of the adult WT ($p > 0.05$, two-sample Student's t-test).

Finally, we assessed the recovery from inactivation properties by means of a two-pulse protocol that involves a first depolarization step to 0 mV (50 ms) followed by an identical step delivered after a variable time interval (from 0.4 to 35.2 ms). No significant differences were detected in the activation constant (τ) values ($p > 0.05$ vs adult WT, one-way ANOVA) (**figure 45**).

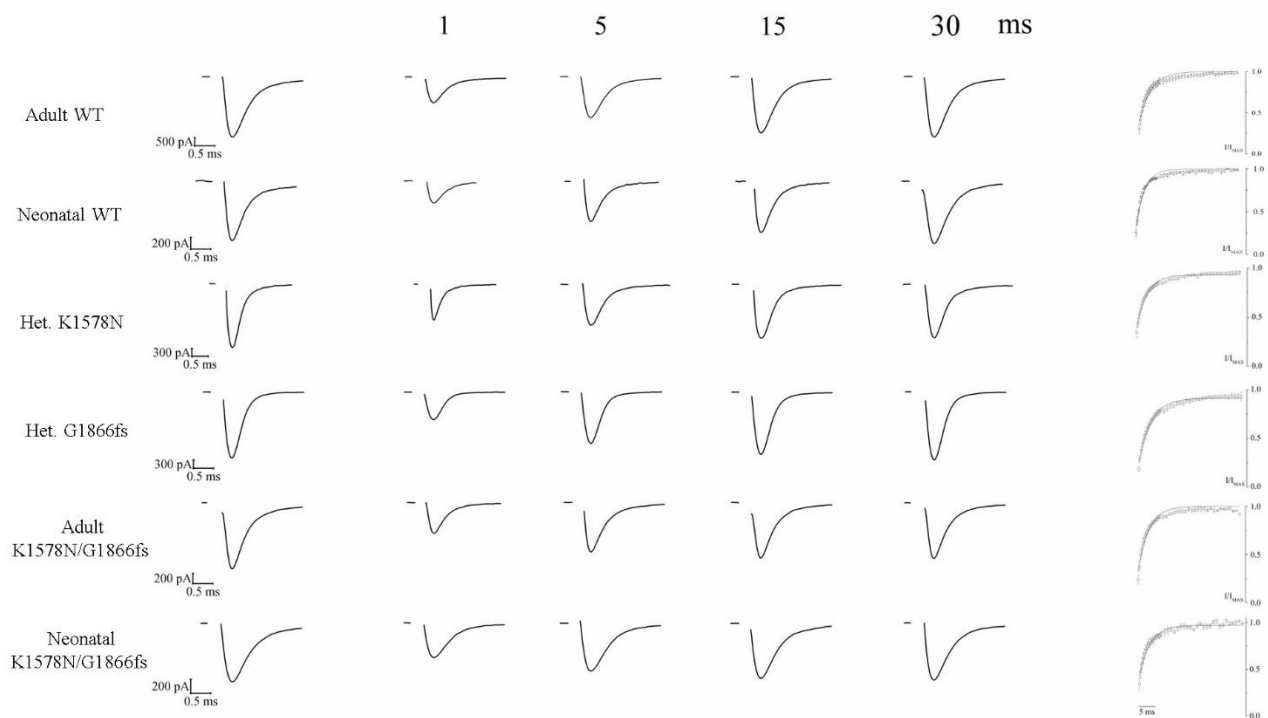


Figure 45. *The recovery from inactivation is not influence by the different isoforms or by the mutations.*

Sample current traces recorded at different times (1-5-15-30ms) after a depolarization to 0 mV (left column) in all the conditions investigated (n=4-8). The time courses are represented in the right column; no difference were detected in the time constant (τ) values ($p > 0.05$, one-way ANOVA).

DISCUSSION

The switch from the neonatal to adult Nav1.5 isoform is a well-documented event in both humans and animals model. However, there is no clear indication on the exact developmental stage at which this switch takes place^{155,156,15}. In addition, literature data relative to the kinetics and amplitude profiles of these isoforms are quite conflicting. The electrophysiological characterization of the WT adult and neonatal isoforms carried out in this study (summarized in **figure 42**) clearly indicate that they carry a similar amount of current but have a different position in the current density peak which is consequent to a positive shift (+5.10 mV) of the activation curve of the neonatal isoform which also displayed a right shift in the inactivation curve (+8.81 mV). These results are in accordance with previous studies^{14,160}.

As mentioned in the *'Introduction'* section, the patient was a baby who carried both the mutations (K1578N/G1866fs) in the SCN5A gene sequence while the parents, who carry one mutation each in heterozygosis, are not affected by any cardiac disease and their ECG traces do not display alterations. To comprehend the different impact of these alterations on the Na_v1.5 channel activity, HEK-293 cells were transfected with the mutated sequences and patch-clamp experiments performed on the WT isoforms were performed (**figure 43**).

When compared to the adult WT isoform, the paternal mutation (K1578N) does not display significant changes in current density and kinetics features, except for a rightward shift of the inactivation curve (+4.83 mV). Taken together, these results support the clinical analysis and confirm a non-pathological scenario.

On the other hand, the maternal mutation (G1866fs) displays a moderate reduction of the current density (-29.24% vs adult WT). This alteration generates a protein with a truncated C-terminus which plays an important role in regulating both channel gating and membrane expression in the WT isoform. The first part of the C-terminus consists of six helices (H1-H6) that are involved in the stabilization of the inactivation state^{161,162}, while the second part is not structured and contains several critical regions involved in protein-protein interaction¹⁶³.

Once the single mutations were characterized in the adult protein structure, we proceeded to reproduce the patient's condition by transfecting HEK-293 cells with both the mutations (K1578N/G1866fs, **figure 44**) in the neonatal isoform. When compared to the WT neonatal isoform this mutant channel was characterized by a great current density reduction (-59.23%) .

Furthermore, in this isoform, Na_v1.5 channels show a positive shift of the activation curve (shift: +7.52 mV, vs neonatal WT) but no alterations in the inactivation properties.

In order to verify whether the neonatal-to-adult isoform switch could be beneficial for the patient, the mutations effects were evaluated in the adult SCN5A isoform (**figure 45**). These data show that a current density reduction is present when compared to the WT adult isoform while no differences were identified vs the compound mutated neonatal isoform (g comparison). Furthermore, since both the mutated isoforms display a comparable activation curve positive shift (**figure 45**), it is possible to assume that the mutations have the same effects on this parameter both in the adult and neonatal isoform. No differences were observed in the inactivation curve (vs WT isoform).

Eventually, the analysis of the recovery from inactivation process did not reveal changes between the investigated condition (**figure 46**).

In conclusion, these data indicate an important loss-of-function of Na_v1.5 channels in the patient's condition, suggesting that the two parental mutations (K1578N–G1866fs), when expressed together, generate a far worst phenotype than their single heterologous expression. Indeed, the analysis of the parents genetic situation reasonably confirms their healthy state and the absence of abnormalities in their ECGs. In addition, even when incorporated in the adult SCN5A isoform, the effects of the compound mutation did not change, suggesting that the neonatal to adult isoform switch will probably grant no benefits for the patient.

The limitation of this study is that in some cases the number of cells investigated is quite low and that this is still an ongoing project; additional experiments are needed in order to confirm these data and to fine tune the differences between WT and mutated isoforms.

REFERENCES

- 1 Thollon, C. *et al.* Electrophysiological effects of S 16257, a novel sino-atrial node modulator, on rabbit and guinea-pig cardiac preparations: comparison with UL-FS 49. *Br J Pharmacol* 112, 37-42, doi:10.1111/j.1476-5381.1994.tb13025.x (1994).
- 2 Bois, P., Bescond, J., Renaudon, B. & Lenfant, J. Mode of action of bradycardic agent, S 16257, on ionic currents of rabbit sinoatrial node cells. *Br J Pharmacol* 118, 1051-1057, doi:10.1111/j.1476-5381.1996.tb15505.x (1996).
- 3 Tardif, J. C. *et al.* Efficacy of ivabradine, a new selective I(f) inhibitor, compared with atenolol in patients with chronic stable angina. *Eur Heart J* 26, 2529-2536, doi:10.1093/eurheartj/ehi586 (2005).
- 4 Cai, X. *et al.* Clinical metabolomics analysis of therapeutic mechanism of Tongmai Yangxin Pill on stable angina. *J Chromatogr B Analyt Technol Biomed Life Sci* 1100-1101, 106-112, doi:10.1016/j.jchromb.2018.09.038 (2018).
- 5 Fan, Y. *et al.* Analysis of bioactive components and pharmacokinetic study of herb-herb interactions in the traditional Chinese patent medicine Tongmai Yangxin Pill. *J Pharm Biomed Anal* 120, 364-373, doi:10.1016/j.jpba.2015.12.032 (2016).
- 6 Guo, R. *et al.* High content screening identifies licoisoflavone A as a bioactive compound of Tongmai yangxin Pills to restrain cardiomyocyte hypertrophy via activating Sirt3. *Phytomedicine* 68, 153171, doi:10.1016/j.phymed.2020.153171 (2020).
- 7 Ng, L. C. T., Putrenko, I., Baronas, V., Van Petegem, F. & Accili, E. A. Cyclic Purine and Pyrimidine Nucleotides Bind to the HCN2 Ion Channel and Variably Promote C-Terminal Domain Interactions and Opening. *Structure* 24, 1629-1642, doi:10.1016/j.str.2016.06.024 (2016).
- 8 Datunashvili, M. *et al.* Modulation of Hyperpolarization-Activated Inward Current and Thalamic Activity Modes by Different Cyclic Nucleotides. *Front Cell Neurosci* 12, 369, doi:10.3389/fncel.2018.00369 (2018).
- 9 Zong, X. *et al.* Regulation of hyperpolarization-activated cyclic nucleotide-gated (HCN) channel activity by cCMP. *J Biol Chem* 287, 26506-26512, doi:10.1074/jbc.M112.357129 (2012).
- 10 North, B. J. & Sinclair, D. A. The intersection between aging and cardiovascular disease. *Circ Res* 110, 1097-1108, doi:10.1161/CIRCRESAHA.111.246876 (2012).
- 11 Lakatta, E. G. & Sollott, S. J. Perspectives on mammalian cardiovascular aging: humans to molecules. *Comp Biochem Physiol A Mol Integr Physiol* 132, 699-721, doi:10.1016/s1095-6433(02)00124-1 (2002).

- 12 Han, D., Tan, H., Sun, C. & Li, G. Dysfunctional Nav1.5 channels due to SCN5A mutations. *Exp Biol Med (Maywood)* 243, 852-863, doi:10.1177/1535370218777972 (2018).
- 13 De Filippo, P., Ferrari, P., Iascone, M., Racheli, M. & Senni, M. Cavotricuspid isthmus ablation and subcutaneous monitoring device implantation in a 2-year-old baby with 2 SCN5A mutations, sinus node dysfunction, atrial flutter recurrences, and drug induced long-QT syndrome: a tricky case of pediatric overlap syndrome? *J Cardiovasc Electrophysiol* 26, 346-349, doi:10.1111/jce.12570 (2015).
- 14 Onkal, R. *et al.* Alternative splicing of Nav1.5: an electrophysiological comparison of 'neonatal' and 'adult' isoforms and critical involvement of a lysine residue. *J Cell Physiol* 216, 716-726, doi:10.1002/jcp.21451 (2008).
- 15 Veerman, C. C., Wilde, A. A. & Lodder, E. M. The cardiac sodium channel gene SCN5A and its gene product NaV1.5: Role in physiology and pathophysiology. *Gene* 573, 177-187, doi:10.1016/j.gene.2015.08.062 (2015).
- 16 Molina, D. K. & DiMaio, V. J. Normal organ weights in men: part I-the heart. *Am J Forensic Med Pathol* 33, 362-367, doi:10.1097/PAF.0b013e31823d298b (2012).
- 17 Anderson, R. H., Yanni, J., Boyett, M. R., Chandler, N. J. & Dobrzynski, H. The anatomy of the cardiac conduction system. *Clin Anat* 22, 99-113, doi:10.1002/ca.20700 (2009).
- 18 Chen, Y. J., Chen, Y. C., Yeh, H. I., Lin, C. I. & Chen, S. A. Electrophysiology and arrhythmogenic activity of single cardiomyocytes from canine superior vena cava. *Circulation* 105, 2679-2685, doi:10.1161/01.cir.0000016822.96362.26 (2002).
- 19 Cheng, H., Smith, G. L., Hancox, J. C. & Orchard, C. H. Inhibition of spontaneous activity of rabbit atrioventricular node cells by KB-R7943 and inhibitors of sarcoplasmic reticulum Ca(2+) ATPase. *Cell Calcium* 49, 56-65, doi:10.1016/j.ceca.2010.11.008 (2011).
- 20 Wongcharoen, W. *et al.* Effects of a Na⁺/Ca²⁺ exchanger inhibitor on pulmonary vein electrical activity and ouabain-induced arrhythmogenicity. *Cardiovasc Res* 70, 497-508, doi:10.1016/j.cardiores.2006.02.026 (2006).
- 21 Brodde, O. E. & Michel, M. C. Adrenergic and muscarinic receptors in the human heart. *Pharmacol Rev* 51, 651-690 (1999).
- 22 Kent, K. M., Epstein, S. E., Cooper, T. & Jacobowitz, D. M. Cholinergic innervation of the canine and human ventricular conducting system. Anatomic and electrophysiologic correlations. *Circulation* 50, 948-955, doi:10.1161/01.cir.50.5.948 (1974).
- 23 Becker, D. E. Fundamentals of electrocardiography interpretation. *Anesth Prog* 53, 53-63; quiz 64, doi:10.2344/0003-3006(2006)53[53:FOEI]2.0.CO;2 (2006).
- 24 Pumpila, J., Howorka, K., Groves, D., Chester, M. & Nolan, J. Functional assessment of heart rate variability: physiological basis and practical applications. *Int J Cardiol* 84, 1-14, doi:10.1016/s0167-5273(02)00057-8 (2002).

- 25 Heart rate variability: standards of measurement, physiological interpretation and clinical use. Task Force of the European Society of Cardiology and the North American Society of Pacing and Electrophysiology. *Circulation* 93, 1043-1065 (1996).
- 26 Cygankiewicz, I. & Zareba, W. Heart rate variability. *Handb Clin Neurol* 117, 379-393, doi:10.1016/B978-0-444-53491-0.00031-6 (2013).
- 27 Thayer, J. F., Hansen, A. L., Saus-Rose, E. & Johnsen, B. H. Heart rate variability, prefrontal neural function, and cognitive performance: the neurovisceral integration perspective on self-regulation, adaptation, and health. *Ann Behav Med* 37, 141-153, doi:10.1007/s12160-009-9101-z (2009).
- 28 Barnett, M. W. & Larkman, P. M. The action potential. *Pract Neurol* 7, 192-197 (2007).
- 29 Pietruszka, M., Stolarek, J. & Pazurkiewicz-Kocot, K. Time evolution of the action potential in plant cells. *J Biol Phys* 23, 219-232, doi:10.1023/A:1005020826000 (1997).
- 30 Fabiato, A. Calcium-induced release of calcium from the cardiac sarcoplasmic reticulum. *Am J Physiol* 245, C1-14, doi:10.1152/ajpcell.1983.245.1.C1 (1983).
- 31 DiFrancesco, D., Ferroni, A., Mazzanti, M. & Tromba, C. Properties of the hyperpolarizing-activated current (if) in cells isolated from the rabbit sino-atrial node. *J Physiol* 377, 61-88, doi:10.1113/jphysiol.1986.sp016177 (1986).
- 32 Brown, H. F., DiFrancesco, D. & Noble, S. J. How does adrenaline accelerate the heart? *Nature* 280, 235-236, doi:10.1038/280235a0 (1979).
- 33 DiFrancesco, D. A new interpretation of the pace-maker current in calf Purkinje fibres. *J Physiol* 314, 359-376, doi:10.1113/jphysiol.1981.sp013713 (1981).
- 34 DiFrancesco, D. A study of the ionic nature of the pace-maker current in calf Purkinje fibres. *J Physiol* 314, 377-393, doi:10.1113/jphysiol.1981.sp013714 (1981).
- 35 Magee, J. C. Dendritic hyperpolarization-activated currents modify the integrative properties of hippocampal CA1 pyramidal neurons. *J Neurosci* 18, 7613-7624 (1998).
- 36 Wang, M. *et al.* Alpha2A-adrenoceptors strengthen working memory networks by inhibiting cAMP-HCN channel signaling in prefrontal cortex. *Cell* 129, 397-410, doi:10.1016/j.cell.2007.03.015 (2007).
- 37 Nolan, M. F. *et al.* The hyperpolarization-activated HCN1 channel is important for motor learning and neuronal integration by cerebellar Purkinje cells. *Cell* 115, 551-564, doi:10.1016/s0092-8674(03)00884-5 (2003).
- 38 Beaumont, V., Zhong, N., Froemke, R. C., Ball, R. W. & Zucker, R. S. Temporal synaptic tagging by I(h) activation and actin: involvement in long-term facilitation and cAMP-induced synaptic enhancement. *Neuron* 33, 601-613, doi:10.1016/s0896-6273(02)00581-0 (2002).

- 39 Zhou, Z. & Lipsius, S. L. Effect of isoprenaline on I(f) current in latent pacemaker cells isolated from cat right atrium: ruptured vs. perforated patch whole-cell recording methods. *Pflugers Arch* 423, 442-447, doi:10.1007/BF00374939 (1993).
- 40 Pian, P., Bucchi, A., Robinson, R. B. & Siegelbaum, S. A. Regulation of gating and rundown of HCN hyperpolarization-activated channels by exogenous and endogenous PIP2. *J Gen Physiol* 128, 593-604, doi:10.1085/jgp.200609648 (2006).
- 41 Sassone-Corsi, P. The cyclic AMP pathway. *Cold Spring Harb Perspect Biol* 4, doi:10.1101/cshperspect.a011148 (2012).
- 42 DiFrancesco, D. & Tortora, P. Direct activation of cardiac pacemaker channels by intracellular cyclic AMP. *Nature* 351, 145-147, doi:10.1038/351145a0 (1991).
- 43 Rybin, V. O., Xu, X., Lisanti, M. P. & Steinberg, S. F. Differential targeting of beta - adrenergic receptor subtypes and adenylyl cyclase to cardiomyocyte caveolae. A mechanism to functionally regulate the cAMP signaling pathway. *J Biol Chem* 275, 41447-41457, doi:10.1074/jbc.M006951200 (2000).
- 44 Parton, R. G. Caveolae--from ultrastructure to molecular mechanisms. *Nat Rev Mol Cell Biol* 4, 162-167, doi:10.1038/nrm1017 (2003).
- 45 Zagotta, W. N. *et al.* Structural basis for modulation and agonist specificity of HCN pacemaker channels. *Nature* 425, 200-205, doi:10.1038/nature01922 (2003).
- 46 Kim, D. M. & Nimigean, C. M. Voltage-Gated Potassium Channels: A Structural Examination of Selectivity and Gating. *Cold Spring Harb Perspect Biol* 8, doi:10.1101/cshperspect.a029231 (2016).
- 47 Biel, M., Schneider, A. & Wahl, C. Cardiac HCN channels: structure, function, and modulation. *Trends Cardiovasc Med* 12, 206-212, doi:10.1016/s1050-1738(02)00162-7 (2002).
- 48 Baruscotti, M., Barbuti, A. & Bucchi, A. The cardiac pacemaker current. *J Mol Cell Cardiol* 48, 55-64, doi:10.1016/j.yjmcc.2009.06.019 (2010).
- 49 Varnum, M. D., Black, K. D. & Zagotta, W. N. Molecular mechanism for ligand discrimination of cyclic nucleotide-gated channels. *Neuron* 15, 619-625, doi:10.1016/0896-6273(95)90150-7 (1995).
- 50 Viscomi, C. *et al.* C terminus-mediated control of voltage and cAMP gating of hyperpolarization-activated cyclic nucleotide-gated channels. *J Biol Chem* 276, 29930-29934, doi:10.1074/jbc.M103971200 (2001).
- 51 Accili, E. A., Proenza, C., Baruscotti, M. & DiFrancesco, D. From funny current to HCN channels: 20 years of excitement. *News Physiol Sci* 17, 32-37, doi:10.1152/physiologyonline.2002.17.1.32 (2002).
- 52 Ludwig, A. *et al.* Two pacemaker channels from human heart with profoundly different activation kinetics. *EMBO J* 18, 2323-2329, doi:10.1093/emboj/18.9.2323 (1999).

- 53 Baruscotti, M., Bucchi, A. & DiFrancesco, D. Physiology and pharmacology of the cardiac pacemaker ("funny") current. *Pharmacol Ther* 107, 59-79, doi:10.1016/j.pharmthera.2005.01.005 (2005).
- 54 Stieber, J., Stockl, G., Herrmann, S., Hassfurth, B. & Hofmann, F. Functional expression of the human HCN3 channel. *J Biol Chem* 280, 34635-34643, doi:10.1074/jbc.M502508200 (2005).
- 55 Lau, Y. T. *et al.* Effects of hyperpolarization-activated cyclic nucleotide-gated (HCN) channel blockers on the proliferation and cell cycle progression of embryonic stem cells. *Pflugers Arch* 461, 191-202, doi:10.1007/s00424-010-0899-9 (2011).
- 56 Yusuf, S. & Camm, A. J. Sinus tachyarrhythmias and the specific bradycardic agents: a marriage made in heaven? *J Cardiovasc Pharmacol Ther* 8, 89-105, doi:10.1177/107424840300800202 (2003).
- 57 DiFrancesco, D. & Camm, J. A. Heart rate lowering by specific and selective I(f) current inhibition with ivabradine: a new therapeutic perspective in cardiovascular disease. *Drugs* 64, 1757-1765, doi:10.2165/00003495-200464160-00003 (2004).
- 58 Snyders, D. J. & Van Bogaert, P. P. Alinidine modifies the pacemaker current in sheep Purkinje fibers. *Pflugers Arch* 410, 83-91, doi:10.1007/BF00581900 (1987).
- 59 Lillie, C. & Kobinger, W. Investigations differentiating the mechanism of specific bradycardic agents from that of calcium channel blockers. *Naunyn Schmiedebergs Arch Pharmacol* 335, 331-333, doi:10.1007/BF00172806 (1987).
- 60 Raes, A., Van de Vijver, G., Goethals, M. & van Bogaert, P. P. Use-dependent block of I_h in mouse dorsal root ganglion neurons by sinus node inhibitors. *Br J Pharmacol* 125, 741-750, doi:10.1038/sj.bjp.0702153 (1998).
- 61 BoSmith, R. E., Briggs, I. & Sturgess, N. C. Inhibitory actions of ZENECA ZD7288 on whole-cell hyperpolarization activated inward current (I_f) in guinea-pig dissociated sinoatrial node cells. *Br J Pharmacol* 110, 343-349, doi:10.1111/j.1476-5381.1993.tb13815.x (1993).
- 62 Gasparini, S. & DiFrancesco, D. Action of the hyperpolarization-activated current (I_h) blocker ZD 7288 in hippocampal CA1 neurons. *Pflugers Arch* 435, 99-106, doi:10.1007/s004240050488 (1997).
- 63 Borer, J. S., Fox, K., Jaillon, P., Lerebours, G. & Ivabradine Investigators, G. Antianginal and antiischemic effects of ivabradine, an I(f) inhibitor, in stable angina: a randomized, double-blind, multicentered, placebo-controlled trial. *Circulation* 107, 817-823, doi:10.1161/01.cir.0000048143.25023.87 (2003).
- 64 Swedberg, K. *et al.* Ivabradine and outcomes in chronic heart failure (SHIFT): a randomised placebo-controlled study. *Lancet* 376, 875-885, doi:10.1016/S0140-6736(10)61198-1 (2010).

- 65 Catterall, W. A. Voltage-gated sodium channels at 60: structure, function and pathophysiology. *J Physiol* 590, 2577-2589, doi:10.1113/jphysiol.2011.224204 (2012).
- 66 Makielski, J. C. *et al.* A ubiquitous splice variant and a common polymorphism affect heterologous expression of recombinant human SCN5A heart sodium channels. *Circ Res* 93, 821-828, doi:10.1161/01.RES.0000096652.14509.96 (2003).
- 67 Lao L., X. L., and Xu S. . Traditional Chinese Medicine *Pediatric Oncology*, 125-135, doi: 10.1007/978-3-642-04201-0_9 (2012).
- 68 Ye, S. *et al.* Effect of a Traditional Chinese Herbal Medicine Formulation on Cell Survival and Apoptosis of MPP(+)-Treated MES 23.5 Dopaminergic Cells. *Parkinsons Dis* 2017, 4764212, doi:10.1155/2017/4764212 (2017).
- 69 Chen, J. X. & Hu, L. S. Traditional chinese medicine for the treatment of chronic prostatitis in China: a systematic review and meta-analysis. *J Altern Complement Med* 12, 763-769, doi:10.1089/acm.2006.12.763 (2006).
- 70 Fung, F. Y. & Linn, Y. C. Developing traditional chinese medicine in the era of evidence-based medicine: current evidences and challenges. *Evid Based Complement Alternat Med* 2015, 425037, doi:10.1155/2015/425037 (2015).
- 71 Burashnikov, A., Petroski, A., Hu, D., Barajas-Martinez, H. & Antzelevitch, C. Atrial-selective inhibition of sodium-channel current by Wenxin Keli is effective in suppressing atrial fibrillation. *Heart Rhythm* 9, 125-131, doi:10.1016/j.hrthm.2011.08.027 (2012).
- 72 Normile, D. DRUG DISCOVERY. Nobel for antimalarial drug highlights East-West divide. *Science* 350, 265, doi:10.1126/science.350.6258.265 (2015).
- 73 Chiou, W. F., Yen, M. H. & Chen, C. F. Mechanism of vasodilatory effect of berberine in rat mesenteric artery. *Eur J Pharmacol* 204, 35-40, doi:10.1016/0014-2999(91)90832-b (1991).
- 74 Bova S., P. R., Goldman W.F., Berman D.M., Cargnelli G. On the mechanism of vasodilating action of berberine: Possible role of inositol lipid signaling system. *Journal of Pharmacology and Experimental Therapeutics* 261 (1), 318-323 (1992).
- 75 Chi, J. F., Chu, S. H., Lee, C. S., Chou, N. K. & Su, M. J. Mechanical and electrophysiological effects of 8-oxoberberine (JKL1073A) on atrial tissue. *Br J Pharmacol* 118, 503-512, doi:10.1111/j.1476-5381.1996.tb15431.x (1996).
- 76 Wang, J., Wong, Y. K. & Liao, F. What has traditional Chinese medicine delivered for modern medicine? *Expert Rev Mol Med* 20, e4, doi:10.1017/erm.2018.3 (2018).
- 77 Tian, G. *et al.* Therapeutic Effects of Wenxin Keli in Cardiovascular Diseases: An Experimental and Mechanism Overview. *Front Pharmacol* 9, 1005, doi:10.3389/fphar.2018.01005 (2018).
- 78 Tu, Y. The discovery of artemisinin (qinghaosu) and gifts from Chinese medicine. *Nat Med* 17, 1217-1220, doi:10.1038/nm.2471 (2011).

- 79 Looareesuwan, S. *et al.* Randomised trial of artesunate and mefloquine alone and in sequence for acute uncomplicated falciparum malaria. *Lancet* 339, 821-824, doi:10.1016/0140-6736(92)90276-9 (1992).
- 80 Bich, N. N. *et al.* Efficacy and tolerance of artemisinin in short combination regimens for the treatment of uncomplicated falciparum malaria. *Am J Trop Med Hyg* 55, 438-443, doi:10.4269/ajtmh.1996.55.438 (1996).
- 81 Tao S., H. Y., Chen Z., Chen Y., Wang Y., Wang Y. Rapid identification of anti - inflammatory compounds from Tongmai Yangxin Pills by liquid chromatography with high - resolution mass spectrometry and chemometric analysis. *Journal of Separation Science* 38, 1881-1893, doi:<https://doi.org/10.1002/jssc.201401481> (2015).
- 82 Akimoto, M., VanSchouwen, B. & Melacini, G. The structure of the apo cAMP-binding domain of HCN4 - a stepping stone toward understanding the cAMP-dependent modulation of the hyperpolarization-activated cyclic-nucleotide-gated ion channels. *FEBS J* 285, 2182-2192, doi:10.1111/febs.14408 (2018).
- 83 DiFrancesco, D. & Noble, D. A model of cardiac electrical activity incorporating ionic pumps and concentration changes. *Philos Trans R Soc Lond B Biol Sci* 307, 353-398, doi:10.1098/rstb.1985.0001 (1985).
- 84 Bucchi, A., Baruscotti, M. & DiFrancesco, D. Current-dependent block of rabbit sino-atrial node I(f) channels by ivabradine. *J Gen Physiol* 120, 1-13, doi:10.1085/jgp.20028593 (2002).
- 85 Bucchi, A., Baruscotti, M., Robinson, R. B. & DiFrancesco, D. Modulation of rate by autonomic agonists in SAN cells involves changes in diastolic depolarization and the pacemaker current. *J Mol Cell Cardiol* 43, 39-48, doi:10.1016/j.yjmcc.2007.04.017 (2007).
- 86 Bucchi, A., Baruscotti, M., Robinson, R. B. & DiFrancesco, D. I(f)-dependent modulation of pacemaker rate mediated by cAMP in the presence of ryanodine in rabbit sino-atrial node cells. *J Mol Cell Cardiol* 35, 905-913, doi:10.1016/s0022-2828(03)00150-0 (2003).
- 87 Efferth, T., Li, P. C., Konkimalla, V. S. & Kaina, B. From traditional Chinese medicine to rational cancer therapy. *Trends Mol Med* 13, 353-361, doi:10.1016/j.molmed.2007.07.001 (2007).
- 88 Pommier, Y. Topoisomerase I inhibitors: camptothecins and beyond. *Nat Rev Cancer* 6, 789-802, doi:10.1038/nrc1977 (2006).
- 89 Chen, R. *et al.* Tongmai Yangxin pill reduces myocardial No-reflow via endothelium-dependent NO-cGMP signaling by activation of the cAMP/PKA pathway. *J Ethnopharmacol*, 113462, doi:10.1016/j.jep.2020.113462 (2020).
- 90 Yamamoto, T. *et al.* Biochemistry of uridine in plasma. *Clin Chim Acta* 412, 1712-1724, doi:10.1016/j.cca.2011.06.006 (2011).

- 91 Fleg, J. L., Aronow, W. S. & Frishman, W. H. Cardiovascular drug therapy in the elderly: benefits and challenges. *Nat Rev Cardiol* 8, 13-28, doi:10.1038/nrcardio.2010.162 (2011).
- 92 Heidenreich, P. A. *et al.* Forecasting the future of cardiovascular disease in the United States: a policy statement from the American Heart Association. *Circulation* 123, 933-944, doi:10.1161/CIR.0b013e31820a55f5 (2011).
- 93 Fleg, J. L. *et al.* Effects of acute beta-adrenergic receptor blockade on age-associated changes in cardiovascular performance during dynamic exercise. *Circulation* 90, 2333-2341, doi:10.1161/01.cir.90.5.2333 (1994).
- 94 Liu, J. *et al.* Age-associated abnormalities of intrinsic automaticity of sinoatrial nodal cells are linked to deficient cAMP-PKA-Ca(2+) signaling. *Am J Physiol Heart Circ Physiol* 306, H1385-1397, doi:10.1152/ajpheart.00088.2014 (2014).
- 95 Jose, A. D. & Collison, D. The normal range and determinants of the intrinsic heart rate in man. *Cardiovasc Res* 4, 160-167, doi:10.1093/cvr/4.2.160 (1970).
- 96 Christou, D. D. & Seals, D. R. Decreased maximal heart rate with aging is related to reduced {beta}-adrenergic responsiveness but is largely explained by a reduction in intrinsic heart rate. *J Appl Physiol (1985)* 105, 24-29, doi:10.1152/jappphysiol.90401.2008 (2008).
- 97 Larson, E. D., St Clair, J. R., Sumner, W. A., Bannister, R. A. & Proenza, C. Depressed pacemaker activity of sinoatrial node myocytes contributes to the age-dependent decline in maximum heart rate. *Proc Natl Acad Sci U S A* 110, 18011-18016, doi:10.1073/pnas.1308477110 (2013).
- 98 They, C., Gosselin, B., Lekieffre, J. & Warembourg, H. Pathology of sinoatrial node. Correlations with electrocardiographic findings in 111 patients. *Am Heart J* 93, 735-740, doi:10.1016/s0002-8703(77)80070-7 (1977).
- 99 Evans, R. & Shaw, D. B. Pathological studies in sinoatrial disorder (sick sinus syndrome). *Br Heart J* 39, 778-786, doi:10.1136/hrt.39.7.778 (1977).
- 100 Yazdanyar, A. & Newman, A. B. The burden of cardiovascular disease in the elderly: morbidity, mortality, and costs. *Clin Geriatr Med* 25, 563-577, vii, doi:10.1016/j.cger.2009.07.007 (2009).
- 101 Chow, G. V., Marine, J. E. & Fleg, J. L. Epidemiology of arrhythmias and conduction disorders in older adults. *Clin Geriatr Med* 28, 539-553, doi:10.1016/j.cger.2012.07.003 (2012).
- 102 Chadda, K. R. *et al.* Ageing, the autonomic nervous system and arrhythmia: From brain to heart. *Ageing Res Rev* 48, 40-50, doi:10.1016/j.arr.2018.09.005 (2018).
- 103 Curtis, A. B., Karki, R., Hattoum, A. & Sharma, U. C. Arrhythmias in Patients \geq 80 Years of Age: Pathophysiology, Management, and Outcomes. *J Am Coll Cardiol* 71, 2041-2057, doi:10.1016/j.jacc.2018.03.019 (2018).

- 104 Pfeifer, M. A. *et al.* Differential changes of autonomic nervous system function with age in man. *Am J Med* 75, 249-258, doi:10.1016/0002-9343(83)91201-9 (1983).
- 105 Ziegler, M. G., Lake, C. R. & Kopin, I. J. Plasma noradrenaline increases with age. *Nature* 261, 333-335, doi:10.1038/261333a0 (1976).
- 106 Shen, M. J. & Zipes, D. P. Role of the autonomic nervous system in modulating cardiac arrhythmias. *Circ Res* 114, 1004-1021, doi:10.1161/CIRCRESAHA.113.302549 (2014).
- 107 Kalla, M., Herring, N. & Paterson, D. J. Cardiac sympatho-vagal balance and ventricular arrhythmia. *Auton Neurosci* 199, 29-37, doi:10.1016/j.autneu.2016.08.016 (2016).
- 108 De Meersman, R. E. & Stein, P. K. Vagal modulation and aging. *Biol Psychol* 74, 165-173, doi:10.1016/j.biopsycho.2006.04.008 (2007).
- 109 Umetani, K., Singer, D. H., McCraty, R. & Atkinson, M. Twenty-four hour time domain heart rate variability and heart rate: relations to age and gender over nine decades. *J Am Coll Cardiol* 31, 593-601, doi:10.1016/s0735-1097(97)00554-8 (1998).
- 110 Antelmi, I. *et al.* Influence of age, gender, body mass index, and functional capacity on heart rate variability in a cohort of subjects without heart disease. *Am J Cardiol* 93, 381-385, doi:10.1016/j.amjcard.2003.09.065 (2004).
- 111 Korkushko, O. V., Shatilo, V. B. & Kaukenas, J. K. Changes in heart rhythm power spectrum during human aging. *Aging (Milano)* 3, 177-179, doi:10.1007/BF03324001 (1991).
- 112 Poller, U., Nedelka, G., Radke, J., Ponicke, K. & Brodde, O. E. Age-dependent changes in cardiac muscarinic receptor function in healthy volunteers. *J Am Coll Cardiol* 29, 187-193, doi:10.1016/s0735-1097(96)00437-8 (1997).
- 113 Sgoifo, A. *et al.* Electrode positioning for reliable telemetry ECG recordings during social stress in unrestrained rats. *Physiol Behav* 60, 1397-1401, doi:10.1016/s0031-9384(96)00228-4 (1996).
- 114 Machado, M. P. *et al.* Autonomic nervous system modulation affects the inflammatory immune response in mice with acute Chagas disease. *Exp Physiol* 97, 1186-1202, doi:10.1113/expphysiol.2012.066431 (2012).
- 115 Statello, R. *et al.* Reduced NPY Y1 receptor hippocampal expression and signs of decreased vagal modulation of heart rate in mice. *Physiol Behav* 172, 31-39, doi:10.1016/j.physbeh.2016.07.017 (2017).
- 116 Carnevali, L., Statello, R. & Sgoifo, A. Resting Heart Rate Variability Predicts Vulnerability to Pharmacologically-Induced Ventricular Arrhythmias in Male Rats. *J Clin Med* 8, doi:10.3390/jcm8050655 (2019).
- 117 Thireau, J., Zhang, B. L., Poisson, D. & Babuty, D. Heart rate variability in mice: a theoretical and practical guide. *Exp Physiol* 93, 83-94, doi:10.1113/expphysiol.2007.040733 (2008).

- 118 Carnevali, L. *et al.* Antidepressant-like activity and cardioprotective effects of fatty acid amide hydrolase inhibitor URB694 in socially stressed Wistar Kyoto rats. *Eur Neuropsychopharmacol* 25, 2157-2169, doi:10.1016/j.euroneuro.2015.07.015 (2015).
- 119 Curtis, M. J. *et al.* The Lambeth Conventions (II): guidelines for the study of animal and human ventricular and supraventricular arrhythmias. *Pharmacol Ther* 139, 213-248, doi:10.1016/j.pharmthera.2013.04.008 (2013).
- 120 Vandewalle, G. *et al.* Robust circadian rhythm in heart rate and its variability: influence of exogenous melatonin and photoperiod. *J Sleep Res* 16, 148-155, doi:10.1111/j.1365-2869.2007.00581.x (2007).
- 121 Li, P., Sur, S. H., Mistlberger, R. E. & Morris, M. Circadian blood pressure and heart rate rhythms in mice. *Am J Physiol* 276, R500-504, doi:10.1152/ajpregu.1999.276.2.R500 (1999).
- 122 Evans, J. M., Randall, D. C., Funk, J. N. & Knapp, C. F. Influence of cardiac innervation on intrinsic heart rate in dogs. *Am J Physiol* 258, H1132-1137, doi:10.1152/ajpheart.1990.258.4.H1132 (1990).
- 123 Japundzic, N., Grichois, M. L., Zitoun, P., Laude, D. & Elghozi, J. L. Spectral analysis of blood pressure and heart rate in conscious rats: effects of autonomic blockers. *J Auton Nerv Syst* 30, 91-100, doi:10.1016/0165-1838(90)90132-3 (1990).
- 124 Carnevali, L. & Sgoifo, A. Vagal modulation of resting heart rate in rats: the role of stress, psychosocial factors, and physical exercise. *Front Physiol* 5, 118, doi:10.3389/fphys.2014.00118 (2014).
- 125 Tan, C. O., Cohen, M. A., Eckberg, D. L. & Taylor, J. A. Fractal properties of human heart period variability: physiological and methodological implications. *J Physiol* 587, 3929-3941, doi:10.1113/jphysiol.2009.169219 (2009).
- 126 Ishii, K., Kuwahara, M., Tsubone, H. & Sugano, S. Autonomic nervous function in mice and voles (*Microtus arvalis*): investigation by power spectral analysis of heart rate variability. *Lab Anim* 30, 359-364, doi:10.1258/002367796780739880 (1996).
- 127 Gehrmann, J. *et al.* Phenotypic screening for heart rate variability in the mouse. *Am J Physiol Heart Circ Physiol* 279, H733-740, doi:10.1152/ajpheart.2000.279.2.H733 (2000).
- 128 Axsom, J. E. *et al.* Acclimation to a thermoneutral environment abolishes age-associated alterations in heart rate and heart rate variability in conscious, unrestrained mice. *Geroscience* 42, 217-232, doi:10.1007/s11357-019-00126-7 (2020).
- 129 Yaniv, Y. *et al.* Deterioration of autonomic neuronal receptor signaling and mechanisms intrinsic to heart pacemaker cells contribute to age-associated alterations in heart rate variability in vivo. *Aging Cell* 15, 716-724, doi:10.1111/acel.12483 (2016).

- 130 He, M. *et al.* Association between heart rate variability indices and features of spontaneous ventricular tachyarrhythmias in mice. *Clin Exp Pharmacol Physiol* 47, 1193-1202, doi:10.1111/1440-1681.13275 (2020).
- 131 Jandackova, V. K., Scholes, S., Britton, A. & Steptoe, A. Are Changes in Heart Rate Variability in Middle-Aged and Older People Normative or Caused by Pathological Conditions? Findings From a Large Population-Based Longitudinal Cohort Study. *J Am Heart Assoc* 5, doi:10.1161/JAHA.115.002365 (2016).
- 132 White, M. *et al.* Age-related changes in beta-adrenergic neuroeffector systems in the human heart. *Circulation* 90, 1225-1238, doi:10.1161/01.cir.90.3.1225 (1994).
- 133 Berntson, G. G. *et al.* Heart rate variability: origins, methods, and interpretive caveats. *Psychophysiology* 34, 623-648, doi:10.1111/j.1469-8986.1997.tb02140.x (1997).
- 134 Rowan, W. H., 3rd, Campen, M. J., Wichers, L. B. & Watkinson, W. P. Heart rate variability in rodents: uses and caveats in toxicological studies. *Cardiovasc Toxicol* 7, 28-51, doi:10.1007/s12012-007-0004-6 (2007).
- 135 Laborde, S., Mosley, E. & Thayer, J. F. Heart Rate Variability and Cardiac Vagal Tone in Psychophysiological Research - Recommendations for Experiment Planning, Data Analysis, and Data Reporting. *Front Psychol* 8, 213, doi:10.3389/fpsyg.2017.00213 (2017).
- 136 Shaffer, F. & Ginsberg, J. P. An Overview of Heart Rate Variability Metrics and Norms. *Front Public Health* 5, 258, doi:10.3389/fpubh.2017.00258 (2017).
- 137 Goldstein, D. S., Bentho, O., Park, M. Y. & Sharabi, Y. Low-frequency power of heart rate variability is not a measure of cardiac sympathetic tone but may be a measure of modulation of cardiac autonomic outflows by baroreflexes. *Exp Physiol* 96, 1255-1261, doi:10.1113/expphysiol.2010.056259 (2011).
- 138 Reyes del Paso, G. A., Langewitz, W., Mulder, L. J., van Roon, A. & Duschek, S. The utility of low frequency heart rate variability as an index of sympathetic cardiac tone: a review with emphasis on a reanalysis of previous studies. *Psychophysiology* 50, 477-487, doi:10.1111/psyp.12027 (2013).
- 139 Billman, G. E. The LF/HF ratio does not accurately measure cardiac sympatho-vagal balance. *Front Physiol* 4, 26, doi:10.3389/fphys.2013.00026 (2013).
- 140 La Rovere, M. T. *et al.* Short-term heart rate variability strongly predicts sudden cardiac death in chronic heart failure patients. *Circulation* 107, 565-570, doi:10.1161/01.cir.0000047275.25795.17 (2003).
- 141 Frenneaux, M. P. Autonomic changes in patients with heart failure and in post-myocardial infarction patients. *Heart* 90, 1248-1255, doi:10.1136/hrt.2003.026146 (2004).
- 142 Huikuri, H. V. & Stein, P. K. Clinical application of heart rate variability after acute myocardial infarction. *Front Physiol* 3, 41, doi:10.3389/fphys.2012.00041 (2012).

- 143 Tsuji, H. *et al.* Reduced heart rate variability and mortality risk in an elderly cohort. The Framingham Heart Study. *Circulation* 90, 878-883, doi:10.1161/01.cir.90.2.878 (1994).
- 144 Manolio, T. A. *et al.* Cardiac arrhythmias on 24-h ambulatory electrocardiography in older women and men: the Cardiovascular Health Study. *J Am Coll Cardiol* 23, 916-925, doi:10.1016/0735-1097(94)90638-6 (1994).
- 145 Dukes, J. W. *et al.* Ventricular Ectopy as a Predictor of Heart Failure and Death. *J Am Coll Cardiol* 66, 101-109, doi:10.1016/j.jacc.2015.04.062 (2015).
- 146 Bennett, B. A., Spannhake, E. W., Rule, A. M., Breyse, P. N. & Tankersley, C. G. The Acute Effects of Age and Particulate Matter Exposure on Heart Rate and Heart Rate Variability in Mice. *Cardiovasc Toxicol* 18, 507-519, doi:10.1007/s12012-018-9461-3 (2018).
- 147 Jensen, P. N. *et al.* Incidence of and risk factors for sick sinus syndrome in the general population. *J Am Coll Cardiol* 64, 531-538, doi:10.1016/j.jacc.2014.03.056 (2014).
- 148 Benditt D.G., S. S., Lurie K.G., Lu F. Sinus Node Dysfunction. Willerson J.T., Wellens H.J.J., Cohn J.N., Holmes D.R. (eds) *Cardiovascular Medicine*. Springer, London, 1925-1941, doi:https://doi.org/10.1007/978-1-84628-715-2_93 (2007).
- 149 Choudhury, M., Boyett, M. R. & Morris, G. M. Biology of the Sinus Node and its Disease. *Arrhythm Electrophysiol Rev* 4, 28-34, doi:10.15420/aer.2015.4.1.28 (2015).
- 150 Sodeck, G. H. *et al.* Compromising bradycardia: management in the emergency department. *Resuscitation* 73, 96-102, doi:10.1016/j.resuscitation.2006.08.006 (2007).
- 151 Honjo, H., Boyett, M. R., Kodama, I. & Toyama, J. Correlation between electrical activity and the size of rabbit sino-atrial node cells. *J Physiol* 496 (Pt 3), 795-808, doi:10.1113/jphysiol.1996.sp021728 (1996).
- 152 Baruscotti, M., DiFrancesco, D. & Robinson, R. B. A TTX-sensitive inward sodium current contributes to spontaneous activity in newborn rabbit sino-atrial node cells. *J Physiol* 492 (Pt 1), 21-30, doi:10.1113/jphysiol.1996.sp021285 (1996).
- 153 Remme C. A., V. A. O., Hoogaars W. M., Aanhaanen W. T., Scicluna B. P., Annink C., van den Hoff M. J., Wilde A.A., van Veen T. A., Veldkamp M. W., de Bakker J. M., Christoffels V. M. & Bezzina C. R. The cardiac sodium channel displays differential distribution in the conduction system and transmural heterogeneity in the murine ventricular myocardium. *Basic Research in Cardiology* 104(5), 511–522 (2009).
- 154 Milanesi, R., Bucchi, A. & Baruscotti, M. The genetic basis for inherited forms of sinoatrial dysfunction and atrioventricular node dysfunction. *J Interv Card Electrophysiol* 43, 121-134, doi:10.1007/s10840-015-9998-z (2015).
- 155 Sarao, R., Gupta, S. K., Auld, V. J. & Dunn, R. J. Developmentally regulated alternative RNA splicing of rat brain sodium channel mRNAs. *Nucleic Acids Res* 19, 5673-5679, doi:10.1093/nar/19.20.5673 (1991).

- 156 Gustafson, T. A., Clevinger, E. C., O'Neill, T. J., Yarowsky, P. J. & Krueger, B. K. Mutually exclusive exon splicing of type III brain sodium channel alpha subunit RNA generates developmentally regulated isoforms in rat brain. *J Biol Chem* 268, 18648-18653 (1993).
- 157 Schroeter, A. *et al.* Structure and function of splice variants of the cardiac voltage-gated sodium channel Na(v)1.5. *J Mol Cell Cardiol* 49, 16-24, doi:10.1016/j.yjmcc.2010.04.004 (2010).
- 158 Kim, J. B. Channelopathies. *Korean J Pediatr* 57, 1-18, doi:10.3345/kjp.2014.57.1.1 (2014).
- 159 Thomas, P. & Smart, T. G. HEK293 cell line: a vehicle for the expression of recombinant proteins. *J Pharmacol Toxicol Methods* 51, 187-200, doi:10.1016/j.vascn.2004.08.014 (2005).
- 160 Baptista-Hon, D. T. *et al.* Potent inhibition by ropivacaine of metastatic colon cancer SW620 cell invasion and Nav1.5 channel function. *Br J Anaesth* 113 Suppl 1, i39-i48, doi:10.1093/bja/aeu104 (2014).
- 161 Motoike, H. K. *et al.* The Na⁺ channel inactivation gate is a molecular complex: a novel role of the COOH-terminal domain. *J Gen Physiol* 123, 155-165, doi:10.1085/jgp.200308929 (2004).
- 162 Cormier, J. W., Rivolta, I., Tateyama, M., Yang, A. S. & Kass, R. S. Secondary structure of the human cardiac Na⁺ channel C terminus: evidence for a role of helical structures in modulation of channel inactivation. *J Biol Chem* 277, 9233-9241, doi:10.1074/jbc.M110204200 (2002).
- 163 Dolz-Gaiton, P. *et al.* Functional characterization of a novel frameshift mutation in the C-terminus of the Nav1.5 channel underlying a Brugada syndrome with variable expression in a Spanish family. *PLoS One* 8, e81493, doi:10.1371/journal.pone.0081493 (2013).